Investigation into the effects of flow distribution on the photovoltaic performance of a building integrated photovoltaic/thermal solar collector

A thesis

Submitted in partial fulfilment

Of the requirements for the degree

of

Doctor of Philosophy

at

The University of Waikato

by

FAISAL ABID GHANI

The University of Waikato

2013

ABSTRACT

The conversion of solar energy into usable forms of energy such as electricity and heat is attractive given the abundance of solar energy and the numerous issues recently raised in the consumption of fossil fuels. Solar conversion technologies may generally be categorised as either photovoltaic or solar thermal types capable of converting incidental sunlight into electricity and heat respectively. The photovoltaic cell is able to transform incidental sunlight into electricity via the Becquerel effect, however, the single junction crystalline silicon solar cell, the predominant cell type in today's photovoltaic market is only able to utilise a small portion (less than 20%) of incidental sunlight for this purpose. A majority of the remaining portion is absorbed much like a traditional solar thermal collector and sunk as heat by the cell, elevating its operating temperature. Given the negative effect of temperature on photovoltaic cell operation, where a linearly proportional drop in conversion efficiency with elevated temperature can be expected, photovoltaic conversion can be reduced significantly particularly in areas of high irradiance and ambient temperatures. Based on the intrinsic absorption characteristics of the photovoltaic cell, a third type of solar panel referred to as the hybrid photovoltaic thermal collector (PVT) collector has been developed where fluid channels running along the underside of the photovoltaic panel transfer heat away from the cells to minimise this detrimental effect. Furthermore, heat captured from the cells may then be used for space heating or domestic hot water improving the overall collector efficiency.

In this study a unique building integrated PVT (BIPVT) collector is investigated consisting of an aluminium extrusion with structural ribs, fluid channels, and solar conversion materials. In order to evaluate this design, a mathematical model of the collector was developed in order to determine both thermal and electrical yield of the

proposed design. The thermal analyses of the building integrated PVT collector in previous studies have generally adopted the approach applied to traditional solar thermal collectors where the distribution of coolant fluid flowing through the piping array is assumed uniform. For a conventional solar thermal collector this simplification may be reasonable under certain circumstances, however, given the temperature sensitivity of photovoltaic cells and their electrical connection scheme, this assumption may lead to significant modelling error. In order to further investigate this issue, a mathematical model has been developed to determine the photovoltaic yield of a BIPVT collector operating under non-homogeneous operating temperature as a result of flow mal-distribution. The model is composed of three steps individually addressing the issues of 1) fluid flow, 2) heat transfer, and 3) the photovoltaic output of a BIPVT array. Fluid analysis was conducted using the finite element method in order to obtain the individual fluid channel flow rates. Using these values, a heat transfer analysis was then conducted for each module forming the BIPVT array to calculate the photovoltaic operating temperature for the constituent cells forming the array. During this step the finite difference method was utilised to approximate the fin efficiency of the building integrated collector, taking into account its irregular geometry. Finally the photovoltaic yield was calculated using a numerical approach which considered the individual operating temperature of the PV cells. During this step a new method was identified to determine the values of series and shunt resistances and also the diode constant required for the modelling of photovoltaic devices based on the multi-dimensional Newton-Raphson method and current-voltage equations expressed using the Lambert *W*-function. Experimentation was carried out to validate the new modelling methods.

These models were combined to quantify the detrimental impact of flow mal-distribution on photovoltaic yield for a number of scenarios. In the case where flow uniformity was

poorest, only a 2% improvement in photovoltaic yield was obtained in comparison to a traditional photovoltaic panel operating under the same environmental conditions. For the case where flow uniformity was optimal however, photovoltaic output was improved by almost 10%.

This work has shown that the effects of poor flow distribution has the potential to have a substantial negative impact on the photovoltaic output of a building integrated solar collector especially given the variability in its physical geometry. The appropriate design of this technology should therefore consider the effects of this phenomenon. The methodology presented in this study can be used to approximate PV output for a BIPVT array with different array geometries and operating characteristics. Furthermore, the method to calculate solar cell modelling parameters developed in this study is not only useful for the analysis of hybrid PVT systems, but for the general analysis of photovoltaic systems based on crystalline silicon solar cells.

ACKNOWLEDGEMENTS

Firstly I'd like to thank my chief and secondary supervisors Mike Duke and James Carson for all their help and guidance. This undertaking was greatly assisted by their valuable input and feedback. On a personal level, the ups and downs that come with doing any PhD were also much more manageable having such approachable and supportive supervisors.

I'd like to thank Ben McGuiness for all his excellent work building the PV laminator and his assistance with this project in general. Your hands on skills were very much appreciated and an important compliment to the mathematical aspects of this work.

Finally, it's a long road getting to the stage of starting a PhD and finishing one. That journey would of have been impossible without the lifetime of support and encouragement from my family. Thanks mum, dad, and apa for everything you have done for me. I hope you can now say that all that money spent on telescopes, microscopes, electronics, and Lego sets was worth it. I'd like to especially thank my big sister, who has always been there for me.

LIST OF PUBLICATIONS

Journal Papers

F. Ghani and M. Duke, "Numerical determination of parasitic resistances of a solar cell using the Lambert *W*-function", *Solar Energy,* vol. 85, pp. 2386-2394, 2011.

F. Ghani, M. Duke, and J. K. Carson, "Effect of flow distribution on the photovoltaic performance of a building integrated photovoltaic/thermal (BIPVT) collector", *Solar Energy,* vol. 86, pp. 1518-1530, 2012.

F. Ghani, M. Duke, and J. K. Carson, "Numerical calculation of series and shunt resistances and diode quality factor of a photovoltaic cell using the Lambert *W*-function", *Solar Energy*, [Article in Press], 2012

F. Ghani, M. Duke, and J. K. Carson, "Estimation of photovoltaic conversion efficiency of a building integrated photovoltaic/thermal (BIPVT) collector array using an artificial neural network", *Solar Energy*, vol. 86, pp.3378-3387, 2012

F. Ghani, M. Duke, and J. K. Carson, "Numerical calculation of series and shunt resistance of a photovoltaic cell using the Lambert *W*-function: Experimental Evaluation", *Solar Energy,* vol. 87, pp.246-253, 2013.

F. Ghani, M. Duke, and J.K. Carson, "Statistical analysis of factors affecting the flow characteristics and thermal efficiency of a building integrated thermal (BIT) solar collector", *International Journal of heat and fluid flow*, [Under review], 2012.

Conference Papers

F. Ghani and M. Duke, “Numerical determination of series and shunt resistances using the Lambert *W*-function”, IEEE Photovoltaic Specialists Conference, Seattle, Washington, 2011.

F. Ghani and M. Duke, “Calculation of Series and shunt resistance using the Lambert *W*-function: Experimental validation”, EU-PVSEC, Frankfurt, Germany, 2012.

F. Ghani, M. Duke, J. K. Carson, “Extraction of solar cell modelling parameters using the Lambert *W*-function”, Australian Solar Energy Society Conference, Melbourne, Australia, 2012.

Table of Contents

Table of Figures

Chapter 1: Introduction

1.1 Problem statement

In a single hour the quantity of energy received on earth from the sun is equivalent to all the energy consumed by humans in an entire year [1]. This makes solar energy one of the most exploitable renewable energy resources that we know of today. To make use of this abundant supply of energy, research into various technologies which are capable of converting solar energy into usable forms of energy such as electricity and heat is active worldwide. One such device is the hybrid photovoltaic/thermal collector, henceforth referred to as a PVT collector. The PVT collector is a single integrated device which can simultaneously convert incidental solar radiation into both electricity and heat [2]. In the next chapter, research conducted into the operational characteristics of a silicon solar cell and how they are temperature sensitive devices is discussed. In summary, their output is hindered by elevated temperature which is typical in the presence of solar radiation due to their inherent absorption characteristics [3]. Referring to Figure 1, the PVT collector incorporates fluid channels which are used to cool the photovoltaic cells. Therefore, by cooling the photovoltaic cells not only can the photovoltaic yield be improved, but heat recovered from the cells may be used for some purpose such as space heating or domestic hot water applications. By converting radiation into both electricity and heat, the energy yield per square meter of roof used by the building integrated PVT collector is increased significantly over traditional photovoltaic solar thermal technology. Furthermore research has indicated that the overall cost and aesthetics may also be improved [4]. Costs are improved by removing material and labour redundancies as the PVT collector is a single integrated device and aesthetics are improved by integrating solar conversion materials into the building envelope [5].

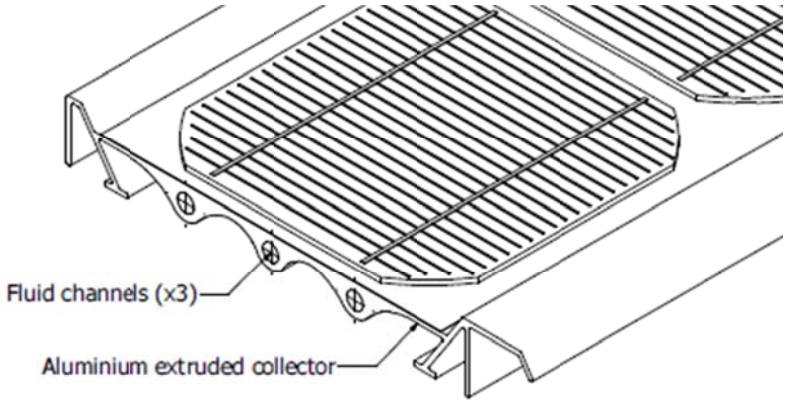

Figure 1 Design of the PVT collector under investigation in this study.

Despite these advantages, the PVT collector is still in its infancy with little penetration into the current solar market. In order to improve the market share of these collectors, their economics must prove favourable over existing technologies. To achieve this goal the development of an accurate model of the PVT collector is required so that its output can be quantified and optimised for specific site conditions, climate, array size, and installation requirements etc.

As PV output will be influenced by temperature, the temperature distribution of the PVT collector must be determined prior to any electrical calculations by conducting a thermal analysis. Currently, the thermal analysis of the PVT collector is typically performed using the one dimensional Hottel-Whillier analysis [6], the same approach carried out for the analysis of standard solar thermal collectors [7]. This method however makes the assumption that flow through each fluid channel of a header/riser fluid network (see Figure 2) is uniform resulting in an even distribution of temperature. However, previous studies have revealed that this is not the case for a traditional solar thermal installation with fluid channel flow rates varying considerably depending on several factors which shall be discussed later. As a result of this flow variation, the operating temperature of each cell being cooled by the fluid will similarly vary leading to electrical losses due to these mismatched conditions. Little research has been carried out which investigates this

phenomenon of flow mal-distribution and its effect on the photovoltaic yield of a PVT collector. This represents a fundamental gap in the understanding of the operational behaviour of the PVT collector.

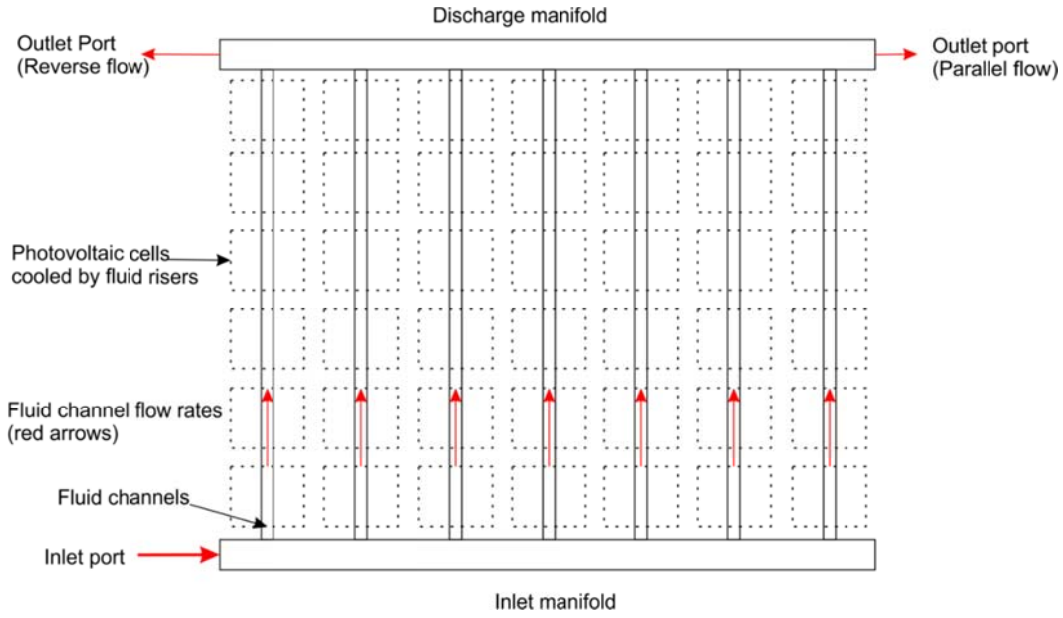

Figure 2 Flow rates through each fluid channel (red arrows) of a header/riser type fluid network will not be equal in the field.

1.2 Aim and scope of research

The aim of this study is to determine what effect flow distribution will have on the output of a building integrated photovoltaic/thermal collector. As previous research has been conducted which examines the effect of flow distribution on the thermal aspects of a traditional solar thermal collector, this study will be primarily focused on the photovoltaic output of the PVT collector. The design of the collector was limited to the aluminium extruded design shown in Figure 1 with a typical header/riser channel network shown in Figure 2 to cool the photovoltaic array. The photovoltaic system consisted of the multi-crystalline silicon (mc-Si) cell type only in this work as it represents the majority of installed photovoltaic devices [8]. The selection of the design shown in Figure 1 is discussed in section 1.2.1.

1.2.1 Collector design selection

Prior to this study, research by Anderson [9] was carried out investigating the thermal aspects of the BIPVT collector. In his work, a standing seam or troughed sheet metal roof made from coloured steel was used to fabricate the collector (refer to Figure 3). In addition to the structural ribs which stiffen the collector and provide the necessary strength, a coolant channel was formed in the profile to provide a pathway for the coolant fluid as shown by Figure 4. The fluid channel was created by attaching a colour coated absorber steel sheet onto the sheet metal roof by the use of adhesives. A number of challenges were encountered with this design however.

i) The coloured steel material used to fabricate the collector was galvanised and dip coated black (to improve absorption). Although varying the material colour was not found to be significantly detrimental to thermal performance [10], welding the absorber sheet to the sheet metal collector was found difficult to achieve unless coatings were first removed [9].

ii) Experience with adhesives as an alternative to welding proved unreliable being prone to leakage and raised serious concern with the longevity of the product.

iii) In order to make the necessary fluid connections to the collector, holes were drilled into the sheet metal collector for the inlet and outlet plumbing fittings (see Figure 3). Nipples were silver soldered onto the underside of the collector for manifold connection. The fluid opening remains at the end so the collector had to be plugged. This process was similarly found unreliable with leaks forming and raised concern over how the process could be reliably implemented in a high speed manufacturing environment.

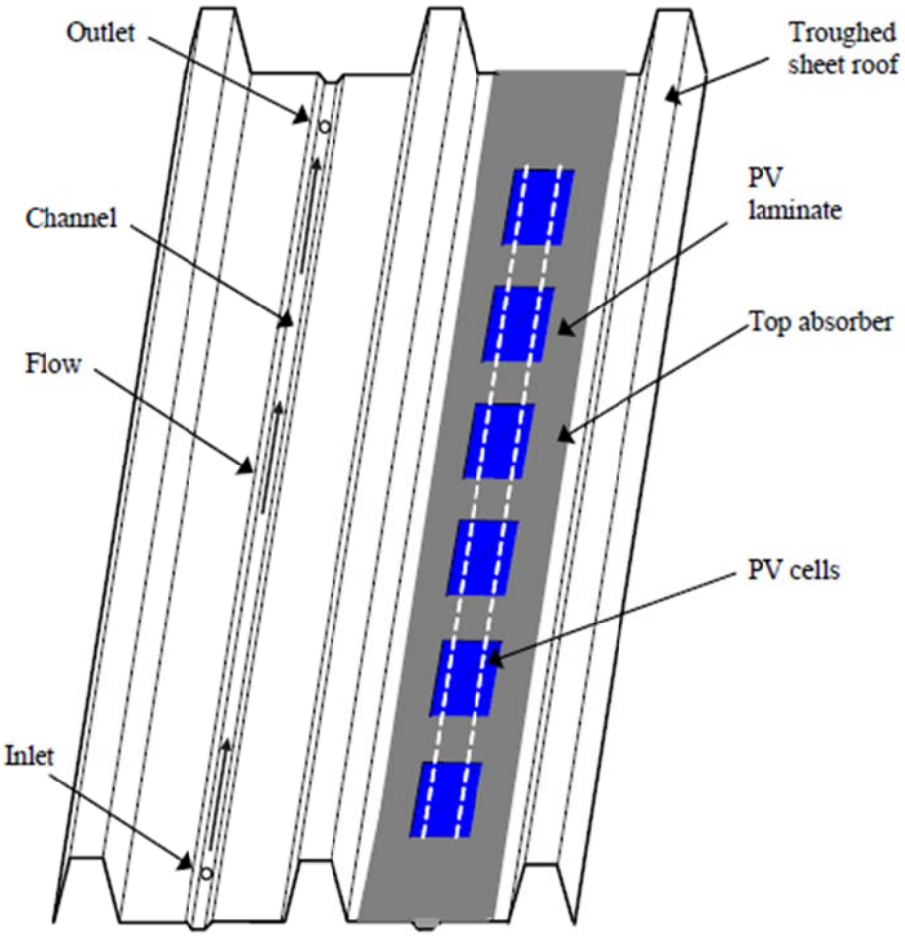

Figure 3 BIPVT Collector design consisting of a standing seam coloured steel roof and an absorber plate adhered in place with pc-Si cells encapsulated using a poly-vinyl resin adhered onto the roofing [9].

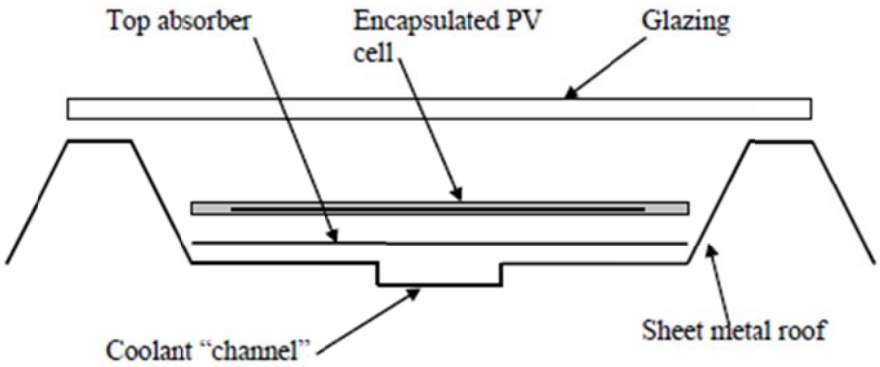

Figure 4 Cross sectional view of the assembly explosion for the collector investigated by Anderson [9].

As a result of these issues, an alternative design was investigated in this study. The use of aluminium extrusions to manufacture the collector which included fluid channels was a promising alternative. By extruding the ribs and fluid channels into a single part, the process of drilling holes into the sheet and silver soldering of nipples as required in the previous design is eliminated removing a significant leakage issue. Fluid channels formed in the extrusion can be tapped and threaded for the connection of plumbing fittings, minimising the risk of leaks. Additionally the high thermal conductivity of aluminium yields an improvement in fin efficiency over a collector fabricated from coloured steel.

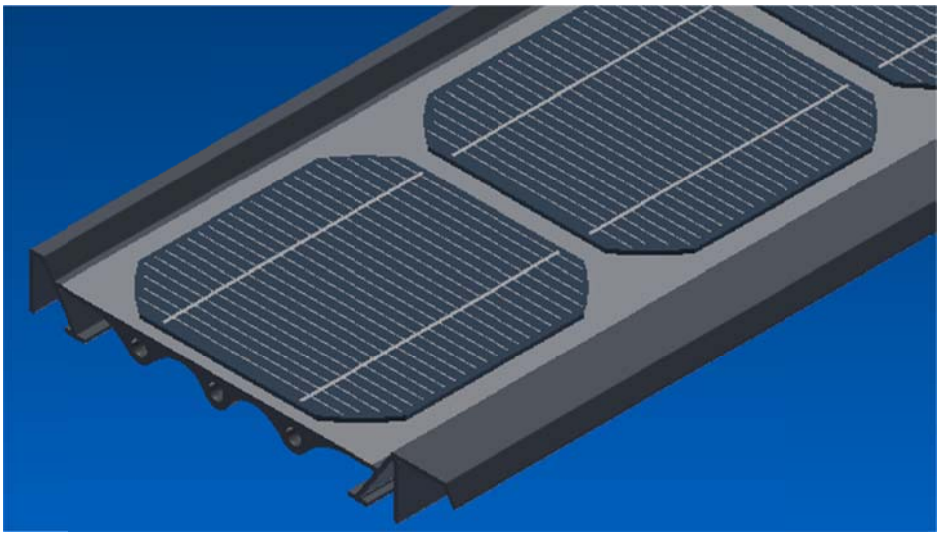

Figure 5 Design of the aluminium extruded BIPVT collector with photovoltaic cells.

The aluminium extrusion design shown in Figure 5 is black anodised to address the issue of corrosion and also to improve the absorption characteristics of the aluminium. The challenge raised by this design however is the method of PV cell encapsulation. The encapsulation process is a critical step to ensure the longevity of the PV system by preventing the ingress of moisture. In this work, vacuum lamination of photovoltaic cells in a sandwich style assembly consisting of a protective top cover (typically glass in current PV modules) and multiple layers of ethylene vinyl-acetate (EVA) was adopted [11]., Figure 6 depicts this assembly type with several layers and their position in the assembly.

Figure 6 Schematic representation of the encapsulation of PV cells using EVA [11].

The assembly shown in Figure 6 is placed in a vacuum laminator (Figure 7) where air is expelled from the assembly and heated to cure the constituent layers of EVA forming the encapsulated assembly.

Figure 7 Flatbed laminator used to cure the EVA and encapsulate the sandwich assembly [11].

As the standard lamination process is typically performed in a flatbed laminator similar to the one shown in Figure 7, the method of laminating onto the extruded aluminium design (Figure 5) with its unique geometry containing structural ribs and fluid channels was an initial concern however research carried out at the University of Waikato in a separate study was able to build a custom laminator capable of laminating the extruded design addressing this issue [12].

With the lamination issue addressed, the aluminium extruded design (Figure 5) was deemed a viable product for manufacture and worthy of further investigation.

1.3 Overview of the thesis

Chapter 2 will review the literature relevant to the PVT collector and the research aim. The major types and design variations of the PVT will be introduced and discussed. Studies regarding the effect of flow distribution in the context of the solar thermal collector will be examined followed by the traditional heat transfer analysis of these systems. Literature regarding the modelling of photovoltaic devices including the influence of temperature and the effects of mismatching will be discussed in detail.

A preliminary investigation into the effect of geometry and other factors specific to the building integrated PVT collector on flow distribution is given in Chapter 3. As the results from Chapter 3 indicated that a large variation in flow distribution is possible for the building integrated PVT collector, a photovoltaic model with the ability to capture heterogeneous array operating temperature was developed. Chapter 4 will describe the research carried out into the development of a unique numerical method for determining the series and shunt resistances of a solar cell, two parameters required for modelling a photovoltaic cell, using the Lambert *W*-function. The experimental method used to validate the numerical method presented in Chapter 4 is presented in Chapter 5. Based on the results presented in Chapter 5, it was found that the numerical method presented in Chapter 4 could be further enhanced. Chapter 6 presents a modified numerical algorithm to calculate the values of series and shunt resistances and also the diode ideality factor. Using the mathematical model of the photovoltaic system developed in chapter's four to six, the effect of flow distribution on the photovoltaic output of the PVT collector is examined in Chapter 7. However, the three step numerical approach presented in Chapter 7 was found to be computationally intensive and time consuming to conduct. To address this issue, an artificial neural network was successfully trained to approximate photovoltaic output considering the phenomenon of flow distribution. Details of this

study are provided in Chapter 8. Conclusions and recommendations are finally provided in Chapter 9.

Chapters 3 to 8 inclusive are presented in their journal article published format. Those already published and submitted for publication are included in the abstract. Prior to each journal paper, a short introduction is provided commenting on the motivation behind the work carried out and its overall contribution to the body of thesis.

Chapter 2: Review of the Literature

2.0 Introduction

Background material relevant to the analysis of the hybrid photovoltaic/thermal (PVT) collector is presented in this chapter. Considerable research into this technology has occurred from its original development in the 70's [13]. Here previous research onto the development of the hybrid PVT collector is reviewed including the advantages and motives behind the technology. Examples will be presented for the PVT/air, PVT/water, and the building integrated (BIPVT) design variants. Despite the technological advantages associated with the PVT collector, a number of obstacles that remain to be addressed, such as the detrimental effect of high temperature on the output of a photovoltaic device, leading to the primary research goal of this study.

2.1 The hybrid photovoltaic/thermal collector

As a result of the OPEC oil embargo in 1973/1974 and the subsequent rise in oil prices, research into the harnessing of solar energy was escalated during this period. One outcome of this research activity was the development of the PVT collector concept originally developed by Martin Wolf in the mid 70's [13]. In this pioneering study, Wolf experimented with a PV array mounted within a non-concentrating thermal collector and a lead acid battery for storage. His work concluded that the concept was both feasible and cost effective leading to significant research into this area.

The PVT collector is a single integrated device which can simultaneously convert solar radiation into both electricity and heat [14]. In essence, solar cells are implemented directly onto a thermal absorber and used for the direct conversion of solar energy into electricity via the photovoltaic effect. The typical silicon solar cell will convert between 4-17% of incidental radiation into electricity [15]. The remaining portion (greater than 50% after the deduction of reflection losses) is absorbed and converted into heat [16]. As

a result of their absorption characteristics [16], the operating temperature of a solar cell can be expected to rise in the presence of radiation. This can lead to two undesirable outcomes:

(i) a drop in conversion efficiency (0.5%/^{o}C rise for silicon cells has been reported [17]) and

(ii) possible permanent damage to the cell due to thermal stress [18].

These undesirable effects, however, can be mitigated by cooling the cells with a fluid (typically either water or air) thus improving their photovoltaic output and lifetime. Total energy yield from the collector can be further improved by capturing and transporting heat collected from the cells for space heating/hot water applications via an active heat recovery system. The photovoltaic array is thus a constituent part of the thermal absorber assembly [19] potentially leading to a substantial increase in the overall efficiency of the collector. Model calculations performed in the 1990's gave the range of the total combined efficiency to be between 60-80% for a hybrid collector [20].

The improved yield of the hybrid collector was experimentally demonstrated in the Netherlands by Zondag et al. [21]. In their study, solar thermal and photovoltaic collectors each of 1 m^2 in area were found to produce 520 kWh and 72 kWh of energy respectively in annual yield. A PVT collector 2m^2 in total area on the other hand was found to yield 720 kWh of thermal energy and 144 kWh of electrical energy, an approximate increase of 44%. These results were further supported in follow-up work by the same group [22]. The advantage of yielding more energy per unit area of roofing in comparison to traditional solar technologies was stated to be particularly relevant to areas of dense population such as India, China, and Japan [23]. For example, a simulation study

demonstrated that the PVT collector can reduce the total roofing area by 60% in comparison to using traditional technology installed side-by-side [24].

A number of design variations currently exist within the PVT family from which two main categories may be identified: (i) concentrated and (ii) flat plate [25]. As the former is beyond the scope of this work this review shall focus only on the flat plate collector. Within this group, collectors can be further classified according to the type of working fluid used to transport heat away from the photovoltaic (PV) cells. Air and water are the most common; however, several studies have investigated the use of refrigerants coupled with heat pumps [26-31]. Furthermore a special variant of the PVT collector, the building integrated PVT or BIPVT collector will be discussed in detail given its particular relevance to this research project. The proceeding sections will review the historical development of each.

2.1.1 The PVT/air collector

Air that is naturally or forcibly circulated can be used simply and economically to cool photovoltaic modules. Forced circulation will offer superior cooling over natural circulation owing to higher rates of convective heat transfer but the additional fan power will reduce net electricity gain [15]. The low thermal conductivity of air, however, results in poor heat transfer between the absorber plate and air [32]. Nevertheless several designs have been proposed to increase the heat transfer coefficient to tackle this issue. These include multiple pass [33, 34], finned absorber [35, 36], and corrugated-type absorber air heaters [37].

The effect of multiple-pass air flow for a solar air heater was theoretically investigated by Garg et al. [33]. The addition of air passes was said to reduce thermal losses from the collector, thereby increasing total energy collected. Optical losses were reported to increase with the addition of covers but the thermal gains were found to improve

performance overall. This is true for a collector whose sole purpose is to heat air, but for a hybrid photovoltaic collector, the optical losses may prove a severe detriment to electricity generation.

A performance comparison between a single and double pass PVT/air collector was analytically carried out by Sopian et al. [38]. The single pass collector consisted of air flowing only under the PV panel whereas the double pass collector included fluid flow over the top and then under the PV panel. For the latter flow arrangement greater heat removal from the top absorber plate was demonstrated consequently reducing absorber plate temperature. By reducing the absorber plate temperature, heat loss to the environment was reduced maximising thermal efficiency. The reduced absorber plate temperature also meant the photovoltaic cells were cooler, improving electric yield.

Hegazy [34] made an extensive numerical investigation of four popular multiple pass PVT/air collector designs looking at thermal, electrical, hydraulic and overall performance. The four designs studied were: Model I - air flowing over absorber, Model II - air flowing under absorber, Model III - air flowing on both sides of the absorber in a single pass, and Mode IV - the same as mode III but in a double pass fashion (see Figure 8).

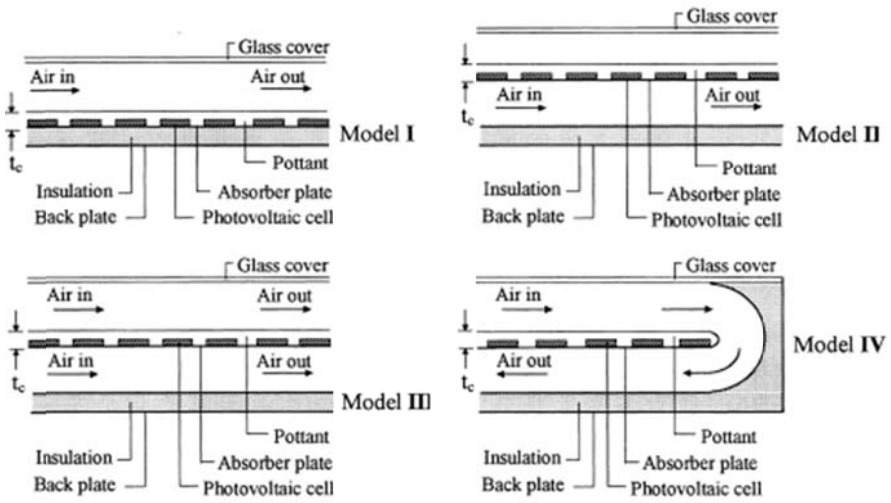

Figure 8: Schematic of PVT/air collector designs evaluated in the study by Hegazy [34].

It was shown from this study that Mode I offered the lowest performance while the other three produced comparable results. Mode III followed by Mode IV and II consumed the least fan power. The suitability of a selective surface absorber plate was also investigated and deemed inappropriate due to reduced PV generation especially at low flow rates.

Joshi et al. [39] evaluated the performance of two single pass hybrid PVT/air collectors. The first PVT/air collector was made with a glass-to-Tedlar® construction and the second was a glass-to-glass type. All experiments were performed outdoors in New Delhi, India. It was found that the glass-to-glass collector operated with the highest thermal efficiency. Thermal efficiency was found to decrease with duct length for both collectors and increase with an increase in duct air velocity.

Another study by Garg et al. [35] showed the effect of introducing rectangular fins and v-groove corrugation into the absorber of a solar air heater by carrying out an theoretical analysis. By increasing the heat transfer area of the absorber using fins, the air outlet temperature was shown to improve.

A black-painted corrugated Aluminium roof was analytically and experimentally investigated by Choudhury et al. [37] as a low cost air heater for low temperature applications such as agricultural use. Electrically driven blowers were used to circulate air in a channel created between the roof and a wooden plate. Collector efficiency measurements were made for various mass flow rates and channel dimensions. In order to obtain high temperatures it was found that that a low mass flow rate with long channel length was necessary. Reducing fin width was found to significantly improve system performance in their study.

A finned double-pass PVT/air collector was investigated by Yusof Othman et al. [6] which adopted both the multiple pass and finned approach. In this collector, air entered through the upper channel formed between the glass cover and a photovoltaic panel which was directly heated by the sun. The air then entered a lower channel formed

between the module back and the mono-crystalline photovoltaic panel. Fins on the back of the PV panel were expected to interrupt air flow, creating turbulence which would in turn improve heat transfer to the air. The collector was tested at steady state under indoor conditions using 500W solar lamps. Thermal efficiency was improved by increasing the air mass flow rate but benchmark collectors were not used to compare the effect of the multiple pass finned strategy in this experiment.

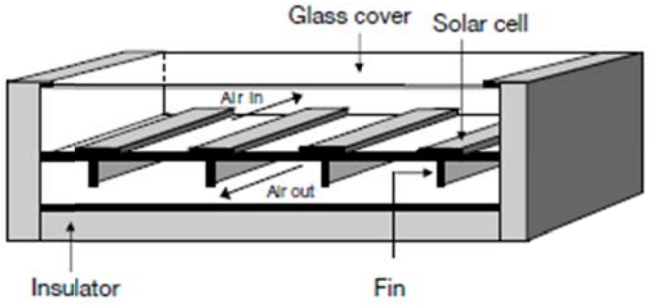

Figure 9 Double pass PVT/air collector with underside fins [6].

Outdoor testing in Greece was carried out on both PVT/air and PVT/water collectors of different configurations by Tripanagnostopoulos et al. [40]. Thermal efficiencies ranged between 38% to 75% and 55% to 80% for the PVT/air and PVT/water collectors respectively. The higher efficiency values were obtained by using low-cost diffuse reflectors between adjacent rows to increase incidental radiation. It was determined that a PVT/air collector would cost 5% more to manufacture over a conventional photovoltaic module and around 8% more for a PVT/water collector with polycrystalline cells.

An innovative photovoltaic collector incorporated into building cladding known as SOLARWALL was reported by Hollick from Conserval Engineering Incorporated [41]. The collector was made from corrugated metal cladding (either galvanized steel or aluminium) and coated for weather protection and also to match building aesthetics. Using crystalline silicon solar cells and heat recovery, the roofing system was found to

make substantial reductions in thermal energy consumption based from indoor testing results. Energy savings of 500 kWh to 1000 kWh per m^2 per year were claimed.

So far this survey has only covered roof-mounted collectors but a novel PVT/air collector in the form of a wallboard has been developed and tested by Nagano et al. [42]. This novel collector was developed in response to the issue of snow build-up on collectors in the cold climate of Hokkaido, Japan. A vertical wall board would not accumulate snow and would function throughout the year. Photovoltaic panels orientated at 80 degrees (relative to the ground) were arranged with a rear air channel where air was circulated using fans. Various configurations were investigated including the fabrication of collectors with amorphous silicon PV and polycrystalline cells and with/without glazing. Thermal efficiencies varied between 20.2 and 22.3% for unglazed collectors and 29.2% and 36.9% for glazed ones. Amorphous silicon cells were found to be unsuitable on account of their low conversion efficiency as the area of the south facing wall of a typical Japanese house would be insufficient to provide the electricity needed.

The disadvantages of the PVT/air collector, however, are the low heat transfer rates due to the low heat capacity and thermal conductivity values of air. Tripanagnostopoulos et al. [40] carried out an extensive comparative study on a combination of PVT collector designs including the use of glazing and air and water as the working fluid. Their study showed that thermal output was improved by up to 30% with the introduction of glazing albeit at the cost of photovoltaic yield. Photovoltaic conversion efficiency was reduced by 16% due to reflection loss introduced by glazing and the elevated working temperature of the photovoltaic cells. Based on these results the authors recommended that glazing be used for applications favouring thermal output. However, by installing low cost booster diffuse reflectors, photovoltaic losses were completely recovered compared with the glazed PVT collector.

Furthermore Kalogirou and Tripanagnostopoulos [43] mentioned that air-type PVT collectors are not suited for applications in medium and high latitude countries due to the low ambient temperatures which limit their implementation. Consequently a significant number of studies have been carried out in the development of the PVT/water collector.

2.1.2 The PVT/water collector

The transport properties of water make it better suited for heat exchange applications based on its higher thermal capacity [44]. Furthermore, water is convenient due to its infrared absorption characteristics which could be exploited when coupled with a PV cell of complimentary spectral response [45]. At present the most popular design resembles the traditional solar thermal collector which utilises the fin and tube approach; however, several other approaches have also been investigated.

In one study, a PVT collector was built by simply laminating photovoltaic cells directly onto the aluminium absorber of a conventional solar thermal collector [46]. The objective of this analysis was to compare the total energy yield of a thermo-electric generator (TEG) and a hybrid PVT collector. The PVT collector of 2.1 m^2 in aperture area was found to operate with a total efficiency of 73.6% at zero reduced temperature. A similar value was reported by Tripanagnostopoulos et al. for a flat plate collector built and tested in Greece [40]. In the study by Tripanagnostopoulos et al., however, the PV panel was mechanically pressed onto the top of the heat exchanger raising the issue of thermal contact resistance with air trapped between the PV panel and absorber. A similar method of coupling the PV panel to the absorber was also reported in another study [47]. A significant improvement in yield was more recently reported by a German group which fabricated a glazed PVT collector by directly laminating single crystalline cells onto an optimised absorber, thus minimising contact resistance [48]. Indoor testing of the collector revealed a combined thermal/photovoltaic conversion efficiency of nearly 88%.

An alternative to the sheet and tube design is to use non-circular fluid channels. Although this may complicate the connection of manifolds, the rectangular cross section channel has potential to increase the fin efficiency value *F* (discussed in Section 2.3). A flat box absorber assembly consisting of aluminium extrusions (Figure 10) was used to construct a PVT collector operating under thermosyphon flow [49]. Such an absorber was quoted by the authors to have a fin efficiency approaching unity.

Figure 10 Flat box channels assembled to create an absorber for a PVT collector [49].

In the Netherlands, a comparative analysis based on a numerical investigation was performed on seven different PVT collector design concepts [22]. The designs investigated were classified into four groups; a) sheet and tube, b) channel flow, c) free flow, and d) two-absorber type collectors (see Figure 11). The sheet and tube design, as already discussed, is the simplest design based on its extensive use in traditional solar thermal collectors. Here a tube was mechanically attached to the absorber with good thermal contact for fluid circulation. The channel design involves water being circulated in a channel between the PV panel and a glass sheet, with care taken to ensure the spectral absorption of the water compliments the spectral response of the solar cell. A similar design was investigated in Turkey which reported the economic benefits of such a design [50]. However it was found by Zondag's group [22] that a small overlap did exist between the absorption characteristics resulting in a 4% drop in electrical efficiency from the PV panel. The free flow design eliminates one of the glass covers used in the channel design so that water is free to flow over the surface of the PV panel. A major issue with

this design is the relatively low evaporation temperature of the water, leading to substantial heat losses.

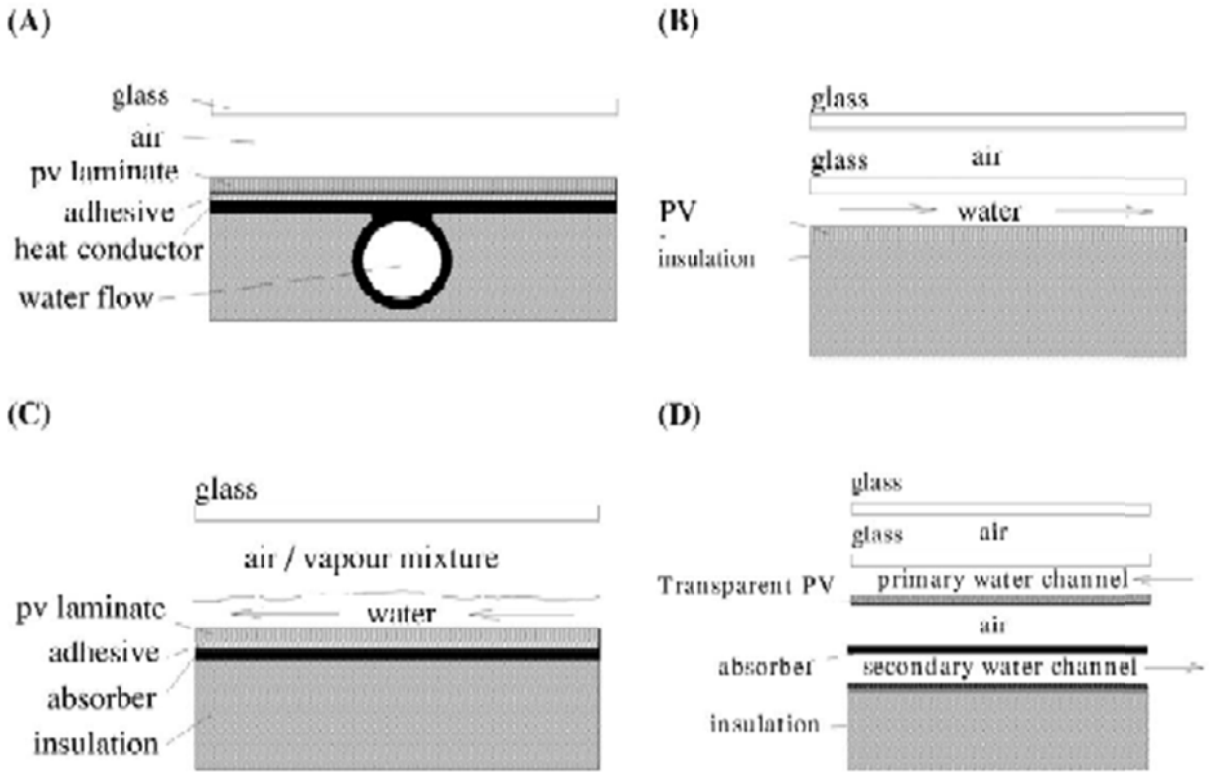

Figure 11 PVT configurations investigated by Zondag et al. [22].

Finally the two-absorber design consists of a fluid being circulated within a channel between a transparent PV panel and a glass sheet. Light transmitted through the PV panel is then absorbed by a secondary black absorber with fluid circulating underneath it. This design, also investigated by MIT in earlier work, was found to offer high thermal performance [51]. The investigation carried out by Zondag et al. [22] supported these results; however, the point was made that the additional materials including two glass sheets increases the weight and fragility of the collector [52]. The sheet and tube with a single cover design was found to operate with only 2% lower efficiency compared to the two-absorber design and is significantly less complex to manufacture. Based on these

results, Zondag et al. made the conclusion that this design is the most promising of the designs investigated.

Further investigation into the sheet and tube design PVT collector was consequently carried out by Zondag et al. [53]. A numerical model was developed in order to identify and quantify the loss mechanisms behind the reduced PV and thermal yield of a PVT collector in comparison to traditional PV and solar thermal collectors respectively. It was found that reductions for both PV and thermal losses could be achieved by the application of anti-reflective coatings and thermal output could be improved by applying a low emissivity coating to the absorber at the expense of electrical efficiency. Their work identified the trade-off that exists between the thermal and photovoltaic efficiencies.

The technology discussed so far is similar to conventional solar thermal and photovoltaic collectors in the sense that they are installed on top of existing building materials (roofs, walls, etc.). A special branch of PVT collectors known as the building integrated PVT or BIPVT collector has recently emerged receiving significant attention. Here traditional building materials are replaced by solar-converting ones.

2.1.3 Building integrated photovoltaic collectors

The energy consumed and the emissions produced by today's modern buildings are gaining more attention as a result of growing demand for the implementation of renewable energy technologies [54]. However one of the challenges facing the implementation of renewable energy today, particularly solar energy systems, is this issue of cost. The economics of solar energy systems needs be addressed to see the transfer of this technology into the market. Studies have been performed which indicate that the PVT collector is favourable over existing technology based on its improved energy yield [22]. The reduced payback time of a PVT collector in comparison to individual technologies

(i.e. PV only or solar thermal only) has consequently been demonstrated by a study conducted in Italy by Frankly et al. [55]. Similarly a study performed in Greece showed that the payback time of the PVT collector was reduced by 10 and 6 years for mono-crystalline (c-Si) and amorphous crystalline (a-Si) modules respectively against the traditional corresponding photovoltaic systems [56].

Further cost reductions, however, are possible by replacing traditional building materials with solar energy conversion materials and removing installation and material redundancies [57]. A number of methods currently exist to incorporate solar technology into the built environment. The first method is to only integrate the photovoltaic panel onto roofs and facades [58]. This rapidly growing area is known as building integrated photovoltaics or BIPV. The second method is to include the characteristics of a traditional solar thermal collector and manufacture what is called a building integrated thermal or BIT collector. Finally the BIPVT collector includes aspects from both BIPV and BIT technologies. Driven by its cost saving potential and architectural uniformity, where even colour can be varied [10, 22, 59], several studies have been carried out exploring this technology.

Photovoltaic technology can be integrated into sloped roofs, flat roofs, facades, and shading devices [54]. By replacing conventional building envelope materials with BIPV technology, the outer surface serves as a climate screen and also a local source of electrical energy. The improved economics of the BIPV collector over a standalone photovoltaic system was demonstrated in one modelling study carried out in India [60]. Supporting the results of Benemann et al. [61], this study provided the details of an economic analysis comparing these two systems showing the improved economics of the building integrated system. In addition to its technological advantages, the BIPV collector offers an aesthetic improvement by providing greater architectural uniformity

One major concern of integrating photovoltaics into rather than onto the building envelope, however, is temperature. The negative effect of temperature on photovoltaic yield will be discussed in detail in a later section; however, it is worth noting that there is a linear drop in conversion efficiency for crystalline silicon solar cells with increased temperature. By incorporating PV technology into structures, higher than usual operating temperatures may result due to the reduced cooling. For example, Davis et al. [62] predicted operating temperatures greater than 20 ^{o}C above the normal operating temperature of a photovoltaic panel. Taking the mean decay of PV conversion efficiency to be 0.5% per degree Celsius rise [63], this will lead to an approximate drop of 10% in PV output compared to normal operation. Similar to the concept behind the PVT collector, by incorporating ventilation or means to actively recover heat from the BIPV panel, the negative effect of temperature can be reduced. This principle has led to the development of the BIPVT collector.

Identifying the potential BIPVT collector to improve the output of a PV system in sunny and warm climates, Chow et al. [64] carried out a comparative analysis of three designs for a hotel located in Macau. The first design was to have an air gap behind the PV panel with open ends to allow natural and wind-induced ventilation of the panel. The second design included means to recover heat from the panels for hotel use via buoyancy induced flow. Finally the third design was a standard BIPV system with no ventilation or heat recovery. Interestingly no significant variation in PV output was calculated from this numerical study between each of the three designs due to the regulated cool indoor temperature of the hotel which effectively cooled the PV cells. However space heat gain through the solar wall was minimised by the PV system with active heat recovery. Additionally between May and October, approximately 70, 000 MJ of warm air was generated, according to the simulation, which could be used for water pre-heating use in the kitchen, etc.

An additional study by Chow et al. [65] experimentally investigated the performance of a BIPVT system mounted on a vertical wall coupled with a thermosyphon-type water cooling system. It was found that the thermal efficiency of the system at zero reduced temperature was 38.9% and the corresponding photovoltaic conversion efficiency was only 8.56%. Similar to the results obtained in the previous study [64], one significant advantage of the building integrated system was the reduced heat gain to the indoor building environment. Consequently space cooling load was reduced by approximately 50%.

2.2 Analysis of PVT collectors

A significant portion of studies in the area of PVT collectors has been largely based on simulation work [24, 66-68]. Models may be used to approximate the output of a collector of various designs operating under different operating conditions making them a valuable tool for economic assessment. Modelling provides a means to investigate areas of interest and avoid the high cost and time consumed in setting up an experiment. This section will discuss the techniques used for the analysis of PVT collectors. The thermal and electrical aspects of the hybrid collector will be individually addressed.

2.2.1 Heat transfer analysis

The thermal analysis of the PVT collector has typically been adapted from the one dimensional analysis of the traditional solar thermal collector, due their operational similarities. However, in order to take into account the effects of the photovoltaic component Florschuetz [69] in the late 1970's proposed an extension to the original procedure developed by Hottel and Woertz [70], Whillier [71], and Hottel and Whillier [72]. The collector analysed by Florschuetz shown in Figure 12 is a typical single glazed sheet and tube collector with photovoltaic cells adhered to the absorber plate.

Temperature distribution in the direction of x for a traditional solar thermal collector operating under steady state conditions is calculated by solving the following second order ordinary differential equation:

$$\frac{d^2T}{dx^2} = \frac{1}{k\delta}\left[U_L(T - T_a) - S\right] \tag{1}$$

Where k is the thermal conductivity of the absorber, δ is the absorber thickness, U_L is the overall heat loss coefficient (W/m K), T is the local absorber temperature, and T_a is the ambient temperature. To take into account the electrical efficiency of the solar cell and its linear drop in conversion efficiency with temperature [73], Florschuetz replaced U_L and S shown in Eq. (1) with modified expressions Eq. (2) and Eq. (3) respectively to give Eq. (4).

$$\hat{U}_L = U_L - \frac{S}{\alpha}\eta_{ref}\beta_{ref} \tag{2}$$

$$\hat{S} = S\left(1 - \frac{\eta_a}{\alpha}\right) \tag{3}$$

$$\frac{d^2T}{dx^2} = \frac{1}{k\delta}\left[\hat{U}_L(T - T_a) - \hat{S}\right] \tag{4}$$

Where η_{ref} is the photovoltaic conversion efficiency of the cell at reference conditions, β_{ref} is the temperature decay coefficient, and η_a is the photovoltaic conversion efficiency of the cell at ambient temperature. The one dimensional thermal analysis of solar collectors has been used extensively due to its simplicity and low computational burden in order to investigate a number of design issues.

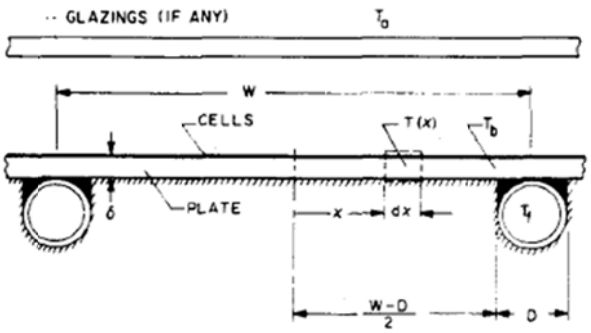

Figure 12 Cross section of the PVT collector analysed by Florschuetz [69].

A one dimensional analysis was conducted by Anderson et al. [74] on a building integrated PVT collector made from coloured steel roofing. Their combined theoretical and experimental study revealed that the attic air space could effectively be used as an insulating barrier and therefore insulating materials at the rear of the collector could be spared, reducing system installation cost. Their analysis makes the assumption that flow within the collector is uniformly distributed [75, 76] yielding a uniform variation in absorber temperature; however, several studies that shall be discussed in section 2.2.2, have demonstrated that fluid flow through a manifold fluid network is not uniform.

2.2.2 Flow distribution within a header riser fluid network

The header/riser fluid network typically used to transport thermal energy away from the absorber in a traditional solar thermal collector is shown in Figure 13. The network shown is comprised of a dividing and combining header and a series of fluid risers. This fluid arrangement is commonly used for applications outside the solar field such as steam generation units and chemical processing plants [77] and has been investigated in several studies.

An early investigation into flow distribution within a manifold system was carried out by Acrivos et al. [78]. The variation in channel flow for a fluid network equivalent to those

shown in Figure 13 and Figure 14 was described by the authors to be a result of a the variation in pressure along the manifold.

A mathematical model was developed in the study by Datta and Majumdar [77] in order to investigate the variation in pressure along the manifolds for a header/riser network operating under both parallel and reverse flow. Their analysis revealed that flow distribution was dependent on three parameters;

a) The ratio of total port areas to header area ($A_R = nd^2/D^2$).

b) The friction parameter ($F = 4f\,LD/nd^2$).

c) The discharge coefficient (C_d) for lateral flows.

Where n is the number of risers or lateral branches, d is the riser diameter, D is the header diameter, f is the friction factor, and L is the header length.

Based on a parametric study of the first two parameters Datta and Majumdar made the following conclusions:

a) The relative variation in lateral flow distribution increases with the ratio of total port areas to header area.

b) Reverse flow in the manifold resulted in the most uniform flow distribution in comparison to parallel flow.

c) In parallel and reverse flow manifolds, maximum branch flow occurs through the last and first ports respectively.

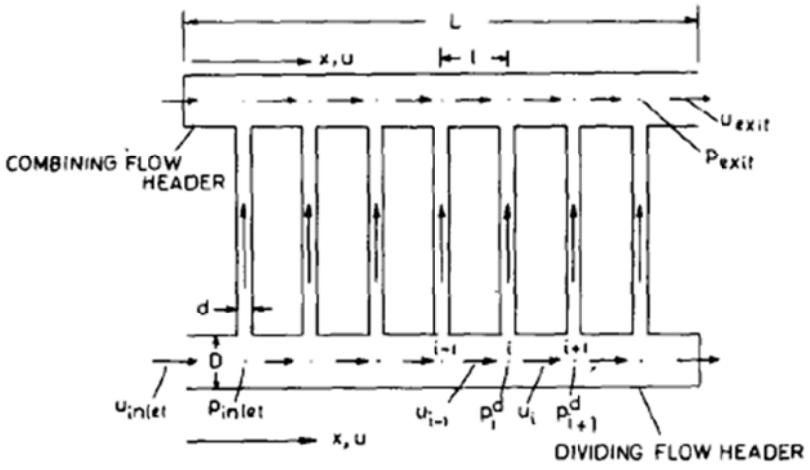

Figure 13 Diagram of a header/riser array under parallel flow [77].

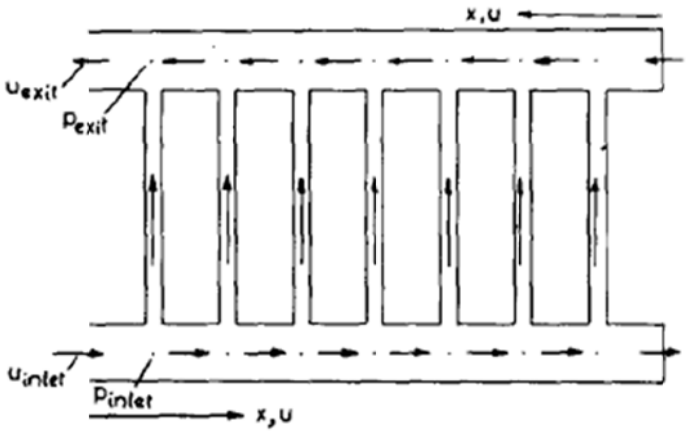

Figure 14 Diagram of a header/riser array under reverse flow.

Their work, however, did not recommend an optimal ratio of dividing/combining manifolds pipe diameter and branch pipe diameters.

Several simulation and experimental studies have since been conducted confirming that flow is not uniformly distributed in a practical installation [79] with flow quality dependent on several factors.

Investigating the issue of non-uniform flow within a solar thermal collector, Chiou [80] developed a numerical model to quantify the flow rate through each individual fluid channel of a solar collector operating under 16 theoretical scenarios. Based on the results

obtained from his fluid analysis, he then plotted the absorber temperature in two spatial co-ordinates demonstrating the large variation obtained due to the non-uniform flow. Consequently a degradation of thermal efficiency between 2-20% was calculated from the analysis when compared to the calculations performed when assuming uniform flow. Based on the results of his study, Chiou concluded that the effects of flow distribution should not be ignored in the analysis of solar thermal collectors.

As opposed to the study of Chiou [76] which was based on numerical simulations, Wang and Wu [81] carried out a combined numerical and experimental study. Their study examined the flow and temperature distribution for an array of ten solar thermal collectors each consisting of 16 risers, giving a total of 160 risers. Additionally, the direction of flow travelling within the inlet and discharge manifolds was varied between parallel and reverse flow. The pattern of flow through each of the arrays was found to be different for parallel and reverse flow directions unlike the results of Datta and Majumdar [77] who reported similar variations in flow for both configurations. For the case of parallel flow, central risers received little flow, while outer risers operated under high flow rates. Consequently a temperature disparity of approximately 30 degrees Celsius was obtained between the two regions. For the case of reverse flow however, only risers closest to the inlet/discharge ports registered significant flow with riser flow rates progressively diminishing. Average thermal efficiencies from each of the arrays were found to be 58.5% and 44.5% for the parallel and reverse flow arrays respectively. From these results it was concluded that reverse flow in the manifold should be avoided. Again, these results contradict the results of Datta and Majumdar [77] which reported that flow distribution was improved with reverse flow in the manifolds.

In addition to the direction of flow in the manifolds, Jones and Lior [82] demonstrated that other factors will similarly influence the quality of flow distribution. By means of a numerical model, the following geometrical factors were varied;

(i) Ratio of the manifold pipe to fluid riser diameter,

(ii) Number of fluid risers, and

(iii) The length of fluid risers.

Their results revealed that the ratio of manifold to riser pipe diameter was the most influential on flow uniformity. Furthermore, by reducing the length of the risers and increasing the number of risers, flow quality was found to diminish. Their study indicates that the shape of the array will have an impact on the flow distribution within a solar array.

Acknowledging the multi-dimensional and transient nature of the solar thermal collector, a numerical model based on the finite volume approach was developed in Spain [83]. One of the objectives of their study was to examine the effect of mal-distribution of coolant flow. Figure 15 displays the results of a computational analysis performed for the absorber temperature operating under uniform and non-inform flow. For the case of uniform flow, riser outlet temperatures for each tube did not differ by more than 0.4 ^{o}C while for non-uniform flow a difference of over 20 ^{o}C was obtained. Their study highlighted the difference between the simplified modelling approach and what can actually be expected from a solar thermal collector.

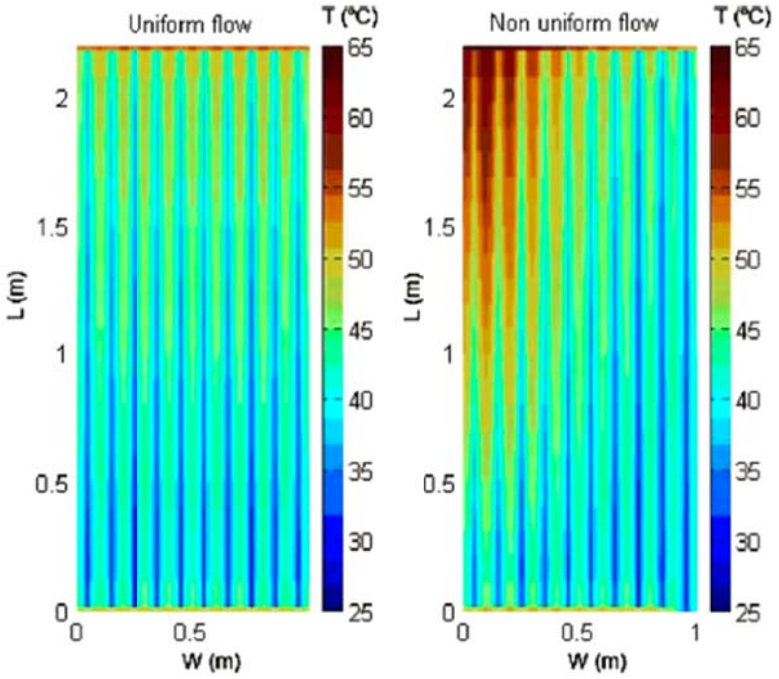

Figure 15 Variation in absorber temperature for a collector under uniform flow (left) and non-uniform flow (right) [83].

Unlike the previous studies which were carried out on conventional solar thermal collectors, research in Thailand more recently investigated the effect of flow uniformity within a PVT collector [84]. The investigation was focused on the geometry of the array which was varied by altering the connection scheme of the PVT modules. Supporting the results of Jones and Lior [82], it was found that by minimising the number of risers (achieved by reducing the number of 'strings' of modules) flow uniformity was improved. Furthermore it was found that by reducing the mass flow rate flow distribution was improved. The limitation of this study, however, was that the net effect on photovoltaic yield was not quantified. To perform this task a model which captures the non-linear behaviour of a photovoltaic system would need to be developed.

2.2.3 Mathematical modelling of photovoltaic cell

The common approach in evaluating the electrical performance of a photovoltaic system is based upon the ability to describe the current-voltage (*I-V*) characteristic for the device under study. The current-voltage characteristics are useful in examining the performance of the cell under various operating conditions and characteristics. Several techniques are generally used to achieve this; however, the lumped parameter approach is most commonly employed [85]. The two most popular variants of this approach are the single and double diode models.

The single diode model describes the behaviour of a solar cell using the modified Shockley diode equation which incorporates a diode quality factor (*n*) to account for the recombination in the space charge region. The double diode model simulates the space charge recombination effect by incorporating a separate current component with its own exponential voltage dependence. It is stated in another study [86] that the double diode model is able to better approximate the behaviour of a solar cell at lower levels of illumination. However the double diode model requires the evaluation of seven parameters which can be difficult to carry out. The single diode model on the other hand requires the evaluation of only five parameters. It has been stated that it offers a good balance between simplicity and accuracy [87], has been shown to adequately fit experimental data at standard test conditions (STC) [88] and has therefore been widely used [89, 90]. The equivalent circuit diagram for this model is shown in Figure 16.

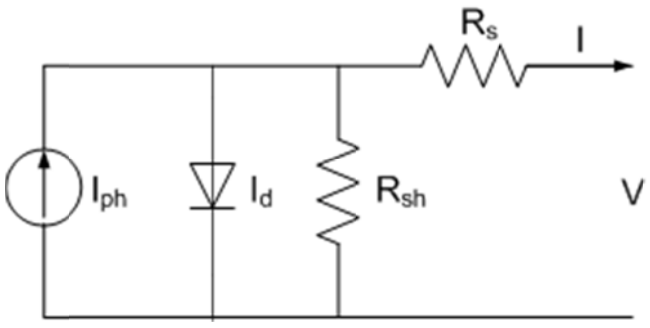

Figure 16 Equivalent circuit diagram of the single diode lumped parameter model [17].

The single diode, five parameter model is represented by Eq. (5) [91].

$$I = I_{ph} - \frac{V + IR_s}{R_{sh}} - I_0 \left[e^{\left(\frac{V + IR_s}{nV_{th}} \right)} - 1 \right] \tag{5}$$

Where I is the current (A), V is the voltage (V), R_s and R_{sh} are the series and shunt resistances respectively (Ω), I_{ph} is the photogenerated current (A), I_0 is the diode saturation current (A), n is the diode ideality factor, and V_{th} is the thermal voltage calculated by Eq. (2).

$$V_{th} = \frac{k_B T}{q} \tag{6}$$

Where k_B is the Boltzmann constant (1.38065 x 10^{-23} J/K), T is the cell junction temperature (K), and q is the value of electron charge (1.6022 x 10^{-19} C).

The five parameter model shown by Eq. (5) may be simplified by assuming the shunt resistance R_{sh} is infinite, eliminating the second term. This is known as the four parameter model. As only four parameters are necessary, it can be a fast and simple method to model a solar cell. This technique has been demonstrated to simulate the behaviour of a solar cell at conditions similar to STC with high accuracy [92]. A comparative study, however, revealed that over the full range of operating conditions, the five parameter model offered superior accuracy over the four parameter model [90]. Several studies have therefore adopted the five parameter approach [93-95].

Modelling accuracy is, however, not only dependent on the type of model used, but also in the accurate calculation of the five modelling parameters required by Eq. (5) [91, 96, 97].

Examination of Eq. (5) shows that current is a nonlinear implicit function of both current and voltage and must therefore be solved numerically for each voltage point along the *I-V* curve (i.e. from 0 to open circuit voltage). This can be computationally burdensome especially when analysing large systems operating under high voltages. An alternative to Eq. (5) has therefore been proposed which models the current equation as an explicit function of voltage using the Lambert *W*-function [98, 99].

$$I = -\frac{V}{R_s + R_{sh}} - \frac{LambertW\left(\frac{R_s I_0 R_{sh}}{nV_{th}(R_s + R_{sh})} e^{\left(\frac{R_{sh}(R_s I_{ph} + R_s I_0 + V)}{nV_{th}(R_s + R_{sh})}\right)}\right) nV_{th}}{R_s} + \frac{R_{sh}(I_0 + I_{ph})}{R_s + R_{sh}} \tag{7}$$

The Lambert *W*-function originated from the work of J.H. Lambert [100] and is defined by the solution of the equation $We^{(W)} = x$. Although it is not often used in the modelling of electronic components, its properties have been well documented [101]. By using the Lambert *W*-function, the transcendental nature of Eq. (1) is transformed into explicit equation Eq. (7) which is a more computationally efficient method of calculating current. This is a particularly useful feature when analysing systems operating under mismatching and heterogeneous conditions such as partial shading [102, 103].

The current-voltage behaviour of a solar cell is heavily dependent on the parameter values such as R_s, R_{sh}, and n found in Eq. (7) [104]. Their effect on the I-V curve and modelling accuracy is discussed in the proceeding section.

2.2.3.1 Effect of R_s, R_{sh}, and n on solar cell behaviour

The performance characteristics of a typical solar cell will deviate from that of an ideal cell due to a number of factors. Two dominant factors are the series (R_s) and shunt resistances (R_{sh}). These resistances shown in Figure 16 are the electrical representations of energy losses within the solar cell. Each loss resistance value embodies losses due to several mechanisms.

The value of series resistance is determined by a number of factors including the bulk resistance of the semiconductor material, the metallic contacts and interconnections, carrier transport through the top diffused layer, and contact resistance between the metallic contacts and semiconductor [105]. One study has demonstrated that daily thermal cycling of the modules installed outdoors will also result in a gradual rise in series resistance [106]. This phenomenon is particularly relevant to PVT collectors. By increasing the series resistance a reduction in the cell's voltage output was obtained reducing both the fill factor and power output. The fill factor is a measure of the 'square-ness' of the IV curve (refer to Figure 17), mathematically defined by the quotient $I_{mp}V_{mp}/I_{sc}V_{oc}$. Ideally the fill factor of a solar cell should be equal to one, however in reality this is difficult to obtain. By increasing the series resistance value from 0.05 to 0.5 ohms, the maximum power output (P_{max}) was reduced by over 60% highlighting the detrimental impact of series resistance on the photovoltaic output of a silicon solar cell. The effect of increasing the series resistance on the I-V relationship is shown in Figure 17.

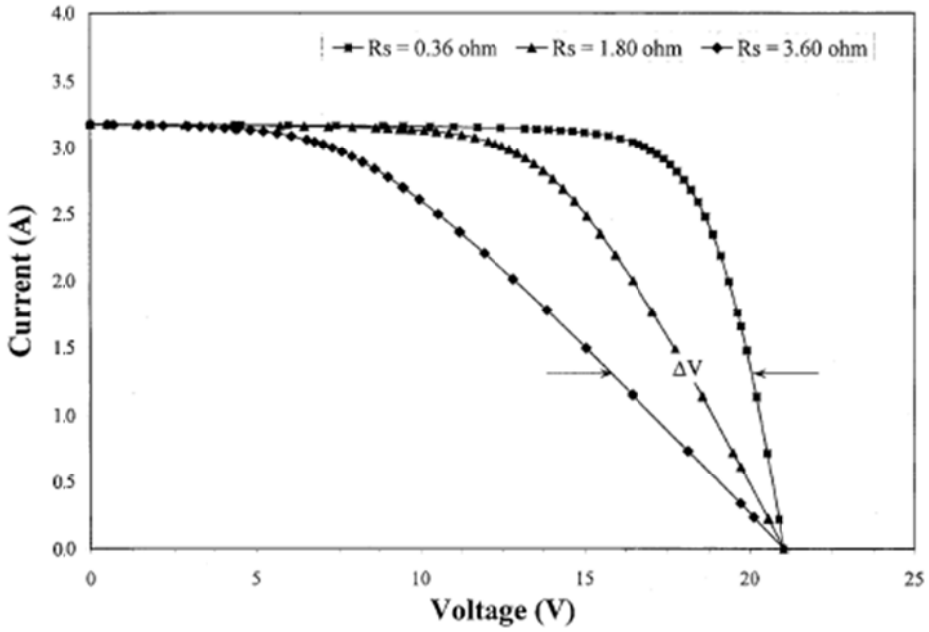

Figure 17 The effect of increasing the series resistance (R_s) on the current-voltage curve of a PV cell [106].

In addition to the losses introduced by the series resistance the shunt resistance, R_{sh}, represents losses that are due to parallel high-conductivity paths across the *p-n* junction or on the cell edges [106]. These are caused by crystal damage and impurities in and near the junction. The presence of a shunt path results in a shunt current which reduces the current flow to the load [106]. By reducing the shunt resistance the current delivered to the load is reduced as a result of an increase in the shunt current. The overall effect is a decrease of both fill factor and maximum power yield [107]. The influence of the shunt resistance on the I-V relationship is shown in Figure 18.

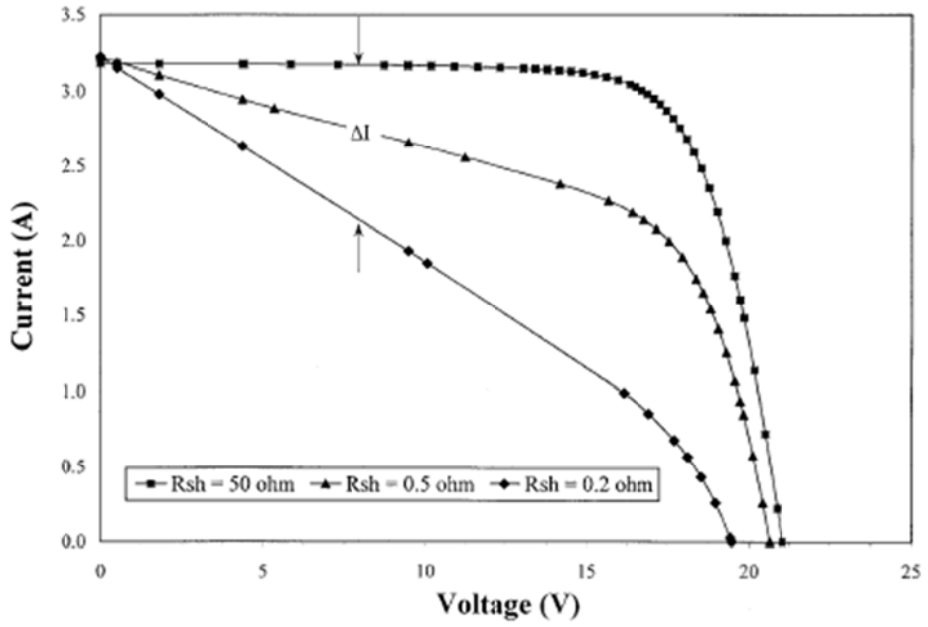

Figure 18 Effect of varying shunt resistance (R_{sh}) on the current-voltage curve a PV cell [106].

Figure 17 and Figure 18 demonstrate the strong influence the resistance values have on the current-voltage relationship. Therefore for accurate modelling of photovoltaic systems it is necessary to determine their values for the system under analysis.

A number of methods have been identified to determine the values of series and shunt resistance. A review of approximately twenty methods by Bashahu and Habyarimana [108] classified the methods under the following groups:

i) Experimental conditions.

ii) Number of diodes to model the solar cell (single or double).

iii) Other assumptions (e.g. Constant ideality factor, infinite/finite shunt resistance).

iv) The simultaneous calculation of other parameters via numerical methods

Experimental work has been carried out previously while the cell is either illuminated or in the dark. Although simple to carry out, carrying out a test in the dark will not provide realistic values due to the unrealistic operating conditions [108].

More recently Villalva et al. [91] proposed a method to calculate the resistance values by using data provided by the manufacturer. The primary advantage of this method is that no experimental work is needed. Their iterative procedure is based on the premise that a single combination of R_s and R_{sh} exists which will allow the mathematical model output to equal the experimentally obtained data published by the manufacturer. By first setting R_s to zero, an equation was produced for calculating the corresponding value of R_{sh}. The paired values for R_{s} and R_{sh} are then used in an equation to determine the value of P_{max}. This value is compared to the data published by the manufacturer. If a mismatch exists, the value for R_s is incremented and the value for R_{sh} re-calculated and the process repeated until this disparity is minimised. An issue with this method, however, is that the diode ideality constant was arbitrarily chosen and no method was provided for its calculation.

Similar to the method of Villalva et al., Carrero et al. [96] also justified the calculation of series and shunt resistance at maximum power point based on the assumption a photovoltaic system will operate while coupled with a maximum power point tracker (MPPT). The method proposed by Carrero is simple to implement and fast to carry out requiring only several iterations. Again however, the authors assumed the diode constant is uniform and equal to unity. The influence of the diode constant on the resistance values was not considered.

In addition to these inherent characteristics of a solar cell, the behaviour of a solar cell is highly dependent on its environment. Temperature will have an effect on the current-voltage curves similar to the parameters just discussed.

2.2.3.2 The effect of temperature on PV output

The electrical conversion efficiency of a typical solar cell lies in the range of 5 - 20% [16]. Theoretically, the remainder of the incidental radiation minus reflection losses is sunk into the cell as heat [15] increasing the operating temperature of the cell. An increase in operating temperature of the cell junction has been demonstrated by a number of studies to result in a reduction of cell performance [109-115]. Several parameters are affected by temperature [116], but the net effects are the changes which occur to the short circuit current (I_{sc}), and open circuit voltage (V_{oc}).

The increase in short circuit current is a direct result of the reduction in bandgap, E_g. The bandgap has been shown to be a function of temperature defined by Eq. (8) [116].

$$E_g(T) = E_g(300K) + \frac{dE_g}{dT}\left(T - 300K\right) \tag{8}$$

For the case of silicon the decay of bandgap with temperature has been reported to be -2.3 x 10^{-4} eV/K [117].

The reduction in bandgap with rising temperature allows the absorption of additional photons which can penetrate the material, generate charge carriers and subsequently increase the short circuit current. The change, however, is marginal [4], e.g. for Silicon solar cells [105],

$$\frac{1}{I_{sc}}\frac{dI_{sc}}{dT} \approx +0.0006°C^{-1} \tag{9}$$

The significant effect of temperature rise is the reduction in open circuit voltage (V_{oc}). The additional thermally generated electrons in the conductivity band and holes in the valence band cause an increase in the reverse saturation current thus reducing open circuit voltage. The decay of open circuit voltage is given by Eq. (10) below [116]:

$$\frac{dV_{oc}}{dT} = -\frac{(E_{g0}/q) - V_{oc}(T_{ref})}{T_{ref}} - \frac{3k_B}{q} \tag{10}$$

Substituting T_{ref} = 300 K, $V_{oc}(T_{ref})$ = 0.55 V, and E_{g0} = 1.12 eV values for a typical silicon solar cell, the derivative of open circuit voltage with temperature is calculated to be approximately -2.3 mV/K [116].

The combined effect of a marginal increase in short circuit current and a linear drop in open circuit voltage is an overall drop in power and conversion efficiency. The traditional linear drop in conversion efficiency is given by Eq. (11) [73].

$$\eta_c = \eta_{T_{ref}}\left[1 - \beta_{ref}(T_c - T_{ref})\right] \tag{11}$$

Where η_{Tref} and β_{ref} are values typically provided by the manufacturer. An extensive review of power and efficiency correlations is provided in other work [118]. Additionally methods to approximate the operating temperature of the photovoltaic panel have been reviewed by the same author [119].

The negative influence of temperature on the performance of photovoltaic devices has been a principal cause for research into the development of the hybrid photovoltaic collector [4, 14, 15, 21, 22, 40, 120, 121]. However as discussed in section 2.3.2, the distribution of coolant will lead to a non-homogeneous array operating temperature. With each cell operating at different temperatures, losses in photovoltaic output will arise due to the issue of mismatching. This area will be discussed in the next section.

2.2.3.3 Photovoltaic mismatch losses

Various studies have revealed that the total yield of an array is less than the summation of each cell's individual output [122]. This reduction in power output, often referred to as mismatch loss (or relative power loss, RPL [123]) occurs due to differences in the current-voltage characteristics of the constituent cells which form the series/parallel connected PV array [124]. As it is highly improbable that a module/array with cells identical in electrical characteristics will be manufactured; some degree of mismatch loss is to be expected in any practical installation. To minimise mismatch losses, classification and sorting of PV cells used to assemble a module with cells of similar characteristics is generally carried out by PV manufacturers. The importance of this manufacturing step was demonstrated in a study which found that mismatch losses could be reduced from 11.2% to 6.1% through appropriate sorting and matching techniques [125]. Originally sorting was done based on the short circuit current of the cell; however, the work by Saha and Bhattacharya [124] argued that the sorting of the photovoltaic cells should be carried out based on the peak-power current (I_{mp}) and fill factor (FF). In addition to the variations in electrical characteristics which arise from the manufacture of PV cells, differences will also arise from shading and cell damage [126, 127], and even from cell aging [128].

The issue of shading, where cells of a PV array are not equally illuminated has been researched extensively [129-132]. Despite the current output from a solar cell being

linearly proportional to the amount of incidental radiation, array losses due to partial shading have been shown to increase non-linearly [133, 134]. Several methods have been investigated to decrease the effects of mismatch losses including the integration of bypass diodes, series/paralleling of cells within modules, and adjusting the shunt resistance of the solar cell.

Discrete bypass diodes are often connected across cells or cell substrings to become forward-biased in the event of mismatch to prevent current limiting [135]. By doing so, power losses due to mismatches are reduced and the maximum power lost in any cell is limited to the power generated by the bypassed cells, thus avoiding hot spot formation [136-138]. Ideally a bypass diode should be installed across each cell; however. this is uneconomical and increases the time and complexity of the module fabrication process. Research into an integrated bypass diode within the cell structure has thus been carried out by the University of New South Wales to overcome these limitations [139-141]. By integrating the diodes, costs can potentially be reduced and module fabrication can be simplified. Roche et al. [142] performed an investigation to compare the performance of two arrays with 64 series-connected cells under shading. One array was fitted with integral bypass diodes (IBDs) and the other was not. The study involved varying the shading of a single cell, multiple columns and multiple rows of the array. It was found that IBDs offered the greatest protection in the case of a single cell being shaded. The disadvantage with the bypass diode however is the additional cost and the marginal reduction in power output as a result of the diode integration. Green [139] estimates the additional cost of the IBD to be less than 5% of the total cell cost. The loss of active cell area with the integration of the diodes results in a power loss of less than 3% but this figure could be reduced with larger cell structures [139, 141].

There is potential to reduce the current limiting effects of a low output cell in a series string by connecting cells in parallel, thereby minimising mismatch losses and maintaining array power output. Roche et al. [142] reported that by increasing redundancy within the series/parallel circuit; the array fill factor and short circuit current can also be improved (see Figure 19). It was stated in this study that the energy benefit of series-paralleling is dependent on the degree of mismatch and the expected prevalence of open circuit defects. Implementation of series-paralleling has been shown to compensate the effects of the small variations in cell output which arise from cell manufacturing by improving performance between 1-3% [143]. In the same study it was shown that arrays subject to partial shading reported improvements of greater than 10%, and in some cases greater than 50%.

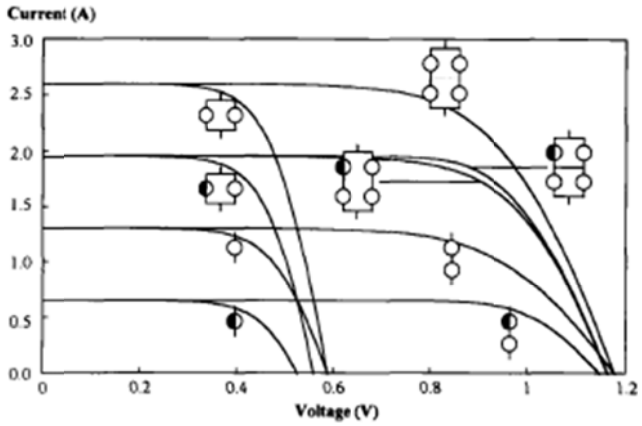

Figure 19 Current voltage curves for a number of PV cell arrangements, showing the effect of redundancy and how an array I-V curve can be determined from its constituent components [142].

Increasing parallelism in the array has been shown to reduce the effects of open-circuit defects, but has also been shown to increase the severity of short-circuit defects. Both effects must be considered when designing large arrays as the expected rates of both defects are similar in magnitude [144]. A study by Goss [145] showed that optimum

levels of series/paralleling exist that minimise both open and short circuit defects. Generally, however, losses due to open circuit defects are likely to exceed short circuit defect losses given the predominance of series over parallel connections. Another disadvantage of this method is the reduction in operating voltage and the high currents produced by the array as a result of paralleling but power conditioning can be employed to overcome this problem at additional system cost [142].

As previously mentioned the shunt resistance is an inherent characteristic of a solar cell. Traditionally, shunt resistances are maximised by cell manufacturers in order to increase the fill factor and power point. However, current limiting, and hence mismatch loss problems arise as a result of these high shunt resistances when cells are connected in a series string [137, 138, 146]. A cell with a low shunt resistance is able to pass a higher current when in reverse bias in comparison to a cell with a higher shunt resistance. Under certain conditions, this has the effect of reducing power losses. In the study by Roche [142] where 36 cells were connected in series, the maximum power was obtained by the array with high shunt resistance under low shading. For the same array, however, power output rapidly declined with increasing shading levels. A performance gain due to shading, however, was partially counteracted by the reduced cell performance as a consequence of the lower shunt resistance. For a cell with a shunt resistance of $10R_{sh,}$ the power loss at zero shading was approximately 5%.

The shunt resistance of a solar cell can be varied during manufacture using a technique known as edge isolation. The outer edge of a doped wafer is a region of high conductivity and forms the shunt path across the p-n junction which must be removed to maximise shunt resistance [147]. By controlling the amount of material used, the value of shunt resistance can be largely varied. Roche [142] suggested that bin sorting of cells based on

their shunt resistance before encapsulation may be a useful way to produce modules with low shunt resistance cells.

Picault et al. [103] investigated the effect of three different topologies on mismatch losses as shown in Figure 20. The traditional series-parallel (SP), total cross tied (TCT), and bridge linked (BL) topologies were all investigated and compared while operating under heterogeneous illumination. The combined numerical and experimental study demonstrated the advantage of connecting the photovoltaic array using the TCT topology. An analysis of the mismatch losses for each of the three configurations revealed that under partial shading the TCT connection scheme suffered half the mismatch loss of the traditional series-parallel (SP) array. These results are also supported by a more recent study [148] which similarly investigated mismatch losses for several topologies.

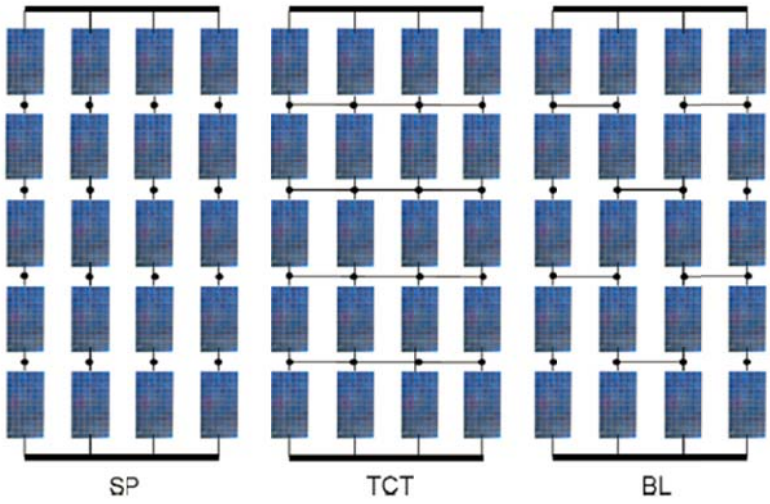

Figure 20 Photovoltaic topologies investigated by Picault et al.[103].

For the case of building integration the choice of topologies is, however, more limited. Examining Figure 1 of the building integrated collector under investigation in this study, the structural ribs will make it difficult to wire cells according to the TCT and BL topologies shown in Figure 20. The series/parallel (SP) scheme on the other hand is possible but will suffer the greatest mismatch loss.

2.3 Summary

The studies discussed have demonstrated that a photovoltaic cell or a region behaving differently to the remainder of the array will have some effect on the total array yield. This has been thoroughly investigated for the case of partial shading as the current output from a cell is linearly proportional to the incidental radiation. However despite the similar relationship which exists between temperature and voltage, the effect of heterogeneous array operating temperature has received limited attention. For a traditional photovoltaic system it is reasonable to assume a homogeneous operating temperature given the basic assumption that the array is exposed to uniform sunlight and cooling. But for the case of a PVT collector a non-homogenous operating temperature is expected due to the non-uniform distribution of coolant flow discussed earlier. In order to investigate this issue further a mathematical model which approximates the fluid flow, calculates the resultant absorber temperature, and finally determines the electrical yield of the array under the heterogeneous operating temperature would be valuable. Additionally, the method for calculating the values of solar cell modelling parameters could also be improved, since the existing methods have limitations, including the fact that the effect of varying the diode constant has not yet been thoroughly investigated.

Therefore, the objectives of this thesis are to:

- Develop a mathematical method to determine the modelling parameters of a photovoltaic cell with greater accuracy than current methods and experimentally validate it.
- Develop a model of a PVT collector which considers the combined effects of fluid flow, heat transfer, and the electrical characteristics of the photovoltaic system.

• Investigate and quantify the effect of flow distribution on photovoltaic output of a PVT collector using the model developed.

• Identify the parameters which will have greatest influence on the distribution of flow and collector output.

Chapter 3: Statistical analysis of factors affecting the flow characteristics and thermal efficiency of a building integrated thermal (BIT) solar collector

Introduction

The literature reviewed in Chapter 2 revealed that several parameters exist which will influence the quality of flow distribution through a traditional solar thermal collector. As a result of non-uniform flow through the fluid network, these studies have demonstrated that an uneven variation in absorber temperature will arise leading to a degradation in thermal efficiency due to heat losses. Previous studies however, have been limited to the case of conventional solar thermal collectors which are generally manufactured to fixed dimensions. In this study however, the building integrated solar collector is under investigation which is unique in comparison to traditional solar thermal collectors in the sense that it can be manufactured to various sizing in order to meet the individual requirements of the customer. As the dimension of the collector fluid array was identified as a parameter to significantly influence the quality of fluid flow in the previous section, this unique characteristic of the building integrated solar collector poses a potential concern. The consequence of non-uniform temperature across the absorber surface as a result of flow mal-distribution and its effect on photovoltaic performance has not been adequately investigated for this specific collector type. This investigation is the focus of this study.

The aim of this chapter is to explore this issue considering the specific traits of the building integrated PVT collector by identifying the main and interaction effects of several parameters identified in previous research to have an effect of flow distribution in a solar collector, and to rank their influence. To achieve this aim, a method to quantify the flow rates through the fluid network and calculate the resultant absorber temperature has been developed. As a large number of variations are possible with respect to the geometry

and operational characteristics of a BIPVT collector, an experimental approach was not feasible for both economic reasons and time constraints. A computational approach was therefore applied to approximate fluid flow through the array using commercial finite element analysis (FEA) software. This approach permitted the exploration of numerous design variations in a short time frame. A heat transfer analysis was then conducted which utilised the individual riser flow rates obtained from the fluid analysis. The method used to determine the fin efficiency of a BIT collector numerically using the finite difference approach is presented. This was carried out in order to take into account the irregular geometry of the BIT collector (i.e. in comparison to the classic fin). For each of the treatment combinations defined in the experiment design, the thermal efficiency was then found.

The influence of four factors; (i) array geometry, (ii) the ratio of the manifold to fluid riser pipe diameters, (iii) direction of flow in the manifolds (i.e. parallel or reverse flow), and (iv) the mass flow rate on the thermal efficiency of a BIT were examined. A two level full factorial (2^k) experiment was designed to identify all main and secondary interactions among the factors.

An examination of the results was carried out by means of an analysis of variance (ANOVA). The results of the analysis demonstrated that the collector geometry does in fact have the greatest impact of the thermal efficiency of a BIT collector. Additionally this work identified two secondary interactions which will also have an impact of thermal efficiency at five per cent significance level. The identification of these secondary interactions has not been previously reported in the literature

The final goal of this thesis is to examine the effect of flow distribution on the photovoltaic output of a BIPVT collector. The work presented in this chapter is an important step to achieve this by first identifying and ranking the factors identified to influence flow distribution. To determine the photovoltaic output the fluid flow and operating temperature of the PV array must first be approximated. A method has been developed in this chapter to quantify the flow distribution and absorber temperature by means of a computational analysis. Furthermore the fin efficiency of the BIT collector of non-classical geometry was approximated using the finite difference method with greater accuracy over the traditional analytical analysis of a rectangular fin.

This paper is currently under review with the journal of International Journal of Heat and Fluid Flow.

Journal Paper: Statistical analysis of factors affecting the flow characteristics and thermal efficiency of a building integrated thermal (BIT) solar collector

F. Ghani[1], M. Duke, J. Carson

[1]Department of Engineering, the University of Waikato, Hamilton 3240, New Zealand
Email: fag2@waikato.ac.nz, Telephone: +64 7 838 4522

Abstract

Previous research has identified four factors (array geometry, manifold to riser channel ratio, flow direction in manifold, and the mass flow rate) which will influence the distribution of coolant flow within a solar thermal collector. In this study, a two level full factorial (2^k) experiment was designed in order to statistically rank their impact and also to identify any significant interactions between these factors. The thermal efficiency of the array, calculated by means of a fluid and heat transfer analysis was taken to be the experiment response. During the heat transfer analysis we approximated the fin efficiency of a BIT collector using the finite difference method which considered the heat losses through the structural ribs of the collector. A statistical analysis of the results revealed that all four main effects had a statistical influence on thermal efficiency of the array at 5 per cent significance level. The main effects ranked from highest to lowest in impact were found to be; geometry, manifold to riser fluid channel diameter, mass flow rate, and the direction of flow in the manifolds. Additionally, two secondary interactions were found to have a statistical influence on the experiment response; the array geometry and the direction of flow in the manifold followed by the array geometry and the ratio of manifold to fluid channel diameter. As the geometry of the BIT collector will vary from customer to customer due to its custom nature, these results indicate that the design of a BIT system should consider the effects of flow distribution. Finally, our numerical analysis of the fin efficiency revealed an approximate 5% drop due to additional heat losses through the structural ribs.

3.0 Introduction

Conversion of solar energy is an attractive alternative to the use of fossil fuels. By harnessing the essentially inexhaustible supply of energy from the sun, we are able to reduce our dependence on fossil fuels and consequently the production of harmful carbon emissions. In addition to growing environmental concerns, seeking alternatives to oil, the supply of which is forecast to diminish significantly in the near future is also of interest to national security. Countries such as China, India, UK, and the USA are all net importers of energy and are heavily dependent on fuel imports [149]. Consequently, global effort is searching for means to enhance this field from both a technological and economic perspective.

A number of methods currently exist in order to convert solar radiation into useful forms of energy such as heat and electricity. In this work, however, we are only concerned with the conversion of solar energy into thermal energy. Solar thermal technology has an extensive history where it has been primarily used for hot water and space heating applications. As hot water heating represents a significant portion of the typical household's electricity consumption, the implementation of solar thermal collectors saw double digit annual growth in Australia and New Zealand over the 2008/2009 period [150]. Further adoption of this technology can be expected by reducing the cost of the system.

A low-cost building integrated type solar thermal collector (Figure 1) henceforth referred to as a BIT collector is currently under development at the University of Waikato. Cost reductions with this collector type are achieved by replacing standard building components with solar conversion materials thereby reducing both material and installation redundancies [57]. The unglazed BIT collector is suitable for various low

temperature applications such as pool heating which requires a low cost solution or for pre-heating domestic hot water systems [151]. Although an unglazed collector will suffer high top heat losses, the absence of a cover and therefore its associated reflection losses results in a higher thermal offset efficiency (when $T_{fluid} = T_{absorber}$) making it ideal for low temperature purposes.

An unglazed building integrated thermal collector fabricated from galvanised and painted sheet metal was investigated by a group in Slovenia [152]. This combined numerical and experimental study demonstrated that the unglazed building integrated thermal collector has substantial economic benefit over conventional glazed solar thermal collectors for low temperature applications. The numerical analysis carried out however in this work makes the assumption that flow within each of the fluid risers is uniform. Several studies have shown this is not the case for practical installations.

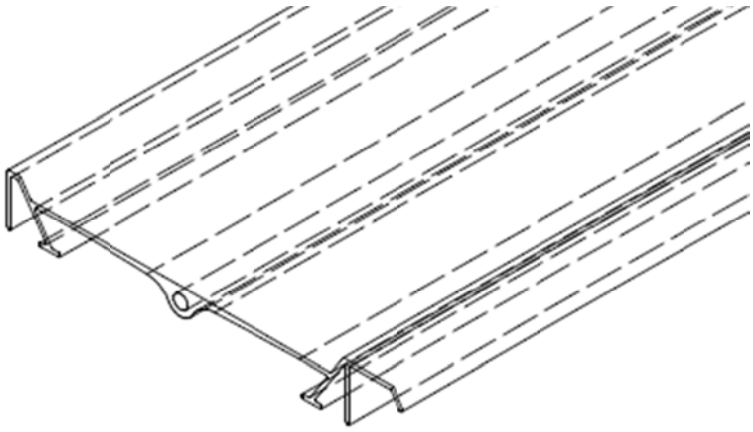

Figure 21 Drawing of BIT concept collector under development at the University of Waikato.

An early numerical study was carried out to investigate the effect of non-uniform flow within a solar thermal collector [80]. Sixteen artificially assumed models were used to demonstrate the correlation between the deterioration of thermal performance and flow

uniformity. It was found in this study that the thermal efficiency deteriorated between 2 and 20 per cent for the flow scenarios investigated.

Another study also showed that the thermal performance of an array of solar thermal collectors will be influenced by distribution of coolant flow [81]. A combined numerical and experimental study was performed on the array of 10 series connected solar thermal collectors operating under parallel and reverse flow in the manifolds. For the case of parallel flow, fluid channel flow rates were found to be greatest near the inlet and outlet ports with little flow registered by the central risers. Consequently collectors near the inlet and outlet ports were substantially cooler than collectors located about the array centre. The pattern of flow distribution was different for the case of reverse flow in the manifolds. For this scenario, it was found that flow was greatest for fluid risers near the inlet/outlet port with a non-linear drop for the proceeding fluid risers. Such a flow pattern meant that the first few collectors operated substantially cooler than the remaining array. Similar results were obtained by the authors in an earlier study [153]. As the array operating under parallel flow was determined to operate with an average thermal efficiency 15% higher than the array operating under reverse flow, the authors recommended avoiding this fluid scheme.

In addition to the direction of flow in the manifolds examined in the previous study Jones and Lior [82] examined other parameters and their effect on flow distribution. In their numerical study, the ratio of the manifold and fluid riser diameters, the number of risers, and the length of the risers were identified to have a significant influence on the flow distribution. Flow distribution was found to worsen if the ratio of the manifold to riser diameters and the riser length reduced and the number of fluid risers increased.

Research conducted so far into the effect of flow distribution has been largely limited to traditional solar thermal technology. In this study we investigate this issue further by

examining the effects of array geometry, the manifold to riser diameter ratio, direction of flow in the manifold, and the mass flow rate on a BIT collector. A numerical approach is outlined in the proceeding sections where the fluid channels flow rates are quantified by carrying out a fluid analysis in a commercial FEA software package Autodesk Simulation Multi-physics®. In order to rank their severity and also to identify the presence of any interaction between main effects, a statistical analysis was performed on the results.

3.1 Method

An overview of the experimental method is provided in Figure 22. Details of the full factorial experiment design shall first be discussed in detail in section 3.2. For each of the treatment combinations (TC's) defined in our experiment design, a numerical fluid analysis was performed using a commercial finite element analysis (FEA) software package. This step was performed in order to quantify the flow rate for each fluid channel of the BIT array. With each fluid channel flow rate calculated, the thermal efficiency for each module of the BIT array was determined via the heat transfer analysis outlined in section 2.3. In this section we also provide detailed steps in the numerical approximation of the BIT fin efficiency using the finite difference method which takes into consideration the unique design of BIT collector.

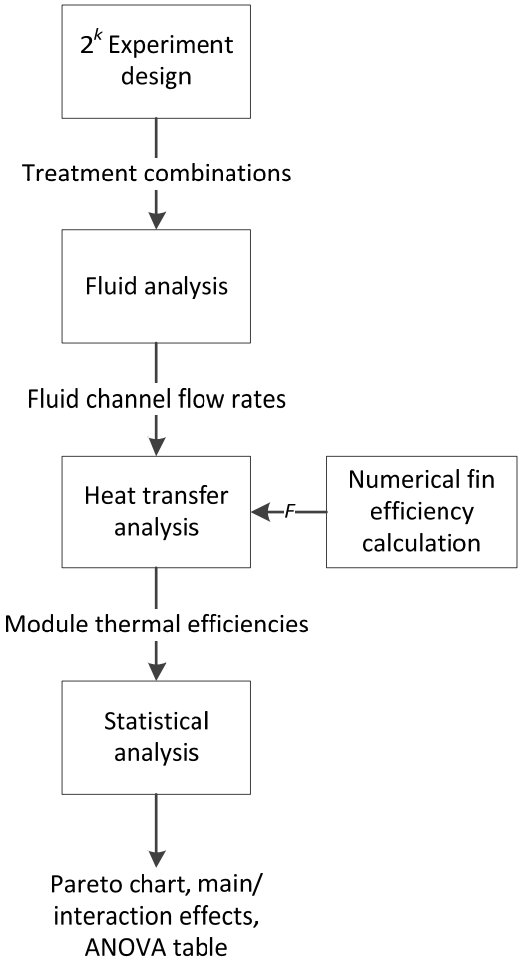

Figure 22 Overview of experiment method.

3.2 Experiment design

A two level full factorial (2^k) experiment was conducted so that the main and interaction effects of the four factors discussed in Section 1.0 could be identified. This experimental design was chosen in order to characterise all the variables under consideration including higher order interactions [154]. One major limitation of the full factorial experiment is that the size of the experiment is a function of the number of factors being considered. However, as we are interested only in four factors (discussed in the previous section), the total number of experiments is acceptable. Indeed it is stated elsewhere that a 2^k experiment is suitable when the number of factors is less than or equal to four [155].

Designated labels and levels for each of the factors investigated are summarised in Table 1.

Table 1 Experiment factors and their levels.

Factor	**Labels**	**Low level**	**High level**
Manifold/Riser ratio	A	1	4
Array geometry	B	24	6
Direction of flow in manifold	C	Reverse	Parallel
Mass flow rate	D	0.0075 kg s^{-1} m^2	0.015 kg s^{-1} m^2

For Factor A, the manifold/riser ratio was varied between a low and high level of $\Phi_{manifold}/\Phi_{riser}$ = 1 and $\Phi_{manifold}/\Phi_{riser}$ = 4 respectively. A ratio of 1 was considered the lowest level by the authors, while a ratio of four was chosen to strike a practical balance between cost and performance. Characteristics of both low and high levels are given by Figure 23.

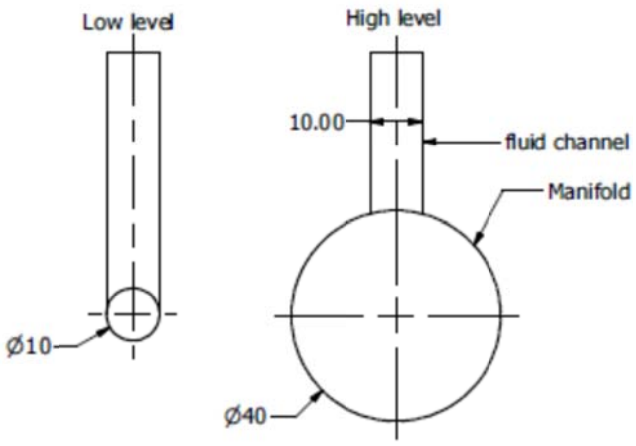

Figure 23 Physical comparison between low and high levels for Factor A.

For Factor B, Array geometry was varied while maintaining a constant absorber area of 3.6 m^2. The array shape was adjusted by varying the number and length of BIT modules altering the aspect ratio of the BIT array. For the low level term, the array consisted of 24

BIT modules of length (L_{abs}) equal to 1 m. For the high level term, the array consisted of only six modules of L_{abs} = 4 m in length. A side-by-side comparison of each of the Arrays is presented in Figure 24.

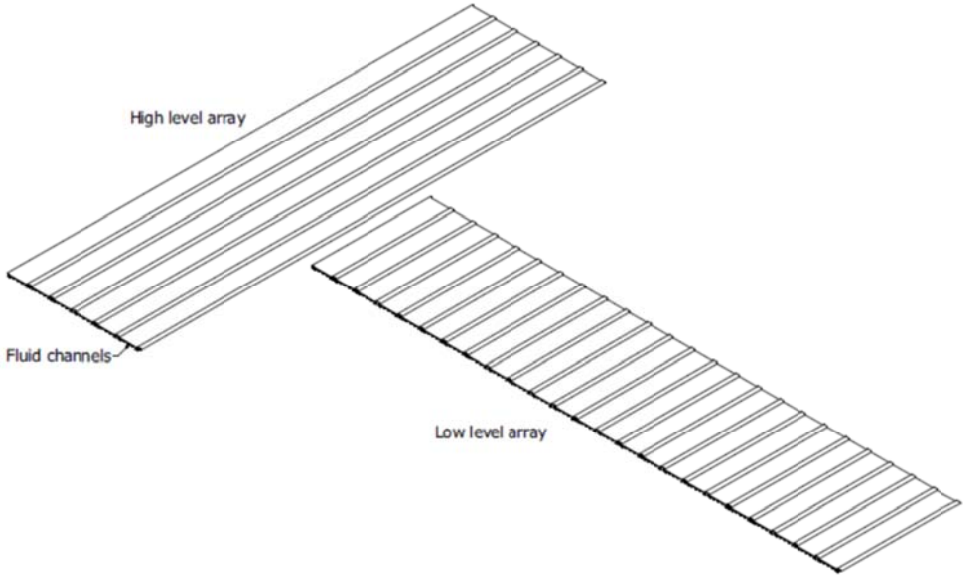

Figure 24 Side-by-side comparison of the two array geometries investigated (Factor B). The low level array consists of 24 BIT modules 1m in length while the high level array is made up of 6 modules 4m in length. Both arrays are 3.6 m2 in area.

The direction of flow in relation to the inlet/discharge manifolds as discussed in the previous section will have an effect on the flow distribution within the array. Factor C therefore is varied between reverse and parallel flow for the low and high levels respectively.

Finally the mass flow rate, Factor D is varied at the low level of m = 0.0075 kg s^{-1} m^2 and at the high level of m = 0.015 kg s^{-1} m^2.

The 2^k factorial experiment carried out was based on four factors (i.e. k = 4), providing a total of 16 treatment combinations. For each treatment combination, the corresponding

factor levels are given in Table 2. The proceeding sections will discuss the method employed to computationally calculate the response of the system (η_{th}).

Table 2 Coded design matrix of experiment providing details of each of the 16 treatment combinations investigated.

TC	**A**	**B**	**C**	**D**
1	-1	-1	-1	-1
2	1	-1	-1	-1
3	-1	1	-1	-1
4	1	1	-1	-1
5	-1	-1	1	-1
6	1	-1	1	-1
7	-1	1	1	-1
8	1	1	1	-1
9	-1	-1	-1	1
10	1	-1	-1	1
11	-1	1	-1	1
12	1	1	-1	1
13	-1	-1	1	1
14	1	-1	1	1
15	-1	1	1	1
16	1	1	1	1

3.3 Fluid Analysis

A 2D planar analysis was performed using Autodesk Simulation Multi-physics to calculate the fluid velocities through each of the fluid channels of the BIT array. For our investigation, water was assumed to be the heat exchange fluid being actively circulated

through the BIT array. As the water is being pumped through the collector, the effects of buoyancy were therefore neglected.

Modelling only the fluid network, the mesh was generated automatically using four node quadrilateral elements operating under the Newtonian viscosity model. Two boundary conditions were specified for our simulation; a surface prescribed velocity at the inlet port of the fluid array which dictated the mass flow rate, and a free surface prescribed at the outlet port face (refer to **Error! Reference source not found.**). Fluid velocity, V at the inlet port was calculated using Eq. (12).

$$m = \rho A V \tag{12}$$

Where m is the desired mass flow rate (Factor D), A is the manifold area (m^2), and ρ is the density of water (kg/m^3).

The location of the outlet port for the array under study (Figure 25) was dependent on whether parallel or reverse flow direction was being analysed as directed by Table 2.

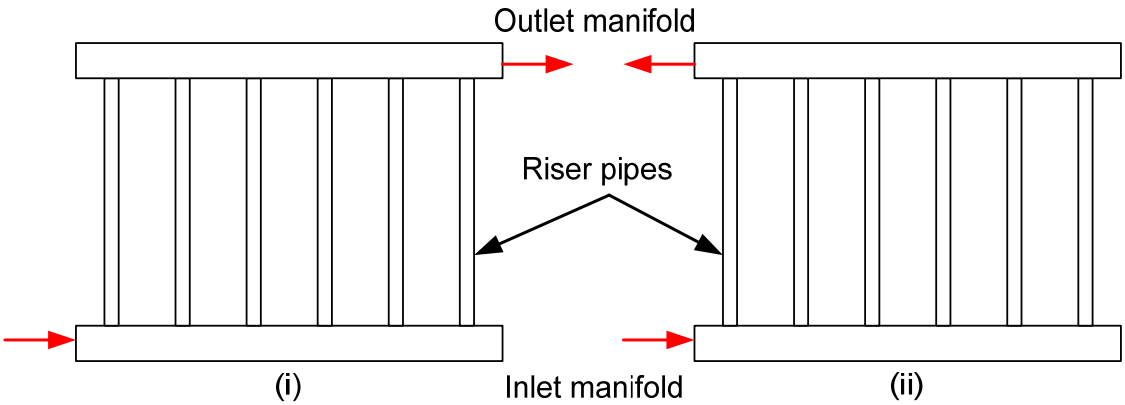

Figure 25 Diagram depicting the difference in flow connections of a header riser flow network for a parallel flow array (left) and a reverse flow array (right) [153].

Sixteen fluid simulations were conducted according to the treatment combinations listed in Table 2. For each simulation the fluid channel flow rates were taken and used for the heat transfer analysis.

3.4 Heat transfer analysis

Each treatment factor investigated in the previous section will result in a unique variation in absorber temperature due to the corresponding variation in fluid flow. The aim of our heat transfer analysis is to determine the thermal efficiency of each module in the BIT array followed by the calculation of the mean module thermal efficiency for each treatment factor. The absorber temperature distribution is calculated using Eq. (13) [7].

$$T(x,y) = \frac{(T_b(y) - T_a - S/U_L)\cosh mx}{\cosh m(W-D)/2} + T_a + (S/U_L) \tag{13}$$

Where T_b is the bond temperature, T_a is the ambient temperature, S is absorbed radiation (W/m^2), x represents an arbitrary distance perpendicular to fluid flow, W is the distance between tubes (m), D is the riser tube diameter (m), and U_L is the overall heat loss coefficient of the collector (W/m^2 K). The overall heat loss co-efficient for our unglazed collector was taken to be a constant value of 22 W/m^2 K [74] in our study. Variable M is calculated using Eq. (14).

$$M = \sqrt{\frac{U_L}{k\delta}} \tag{14}$$

Where k is the thermal conductivity of the absorber material, and δ is the absorber plate thickness (m).

In order to solve Eq. (13), we must first calculate the bond temperature, T_b using Eq. (15) [7].

$$T_b(y) = \frac{WF'\left[S - U_L(T_f(y) - T_a\right]}{h_{fi}\pi D_i} + T_f(y) \tag{15}$$

Where $T_f(y)$ is the temperature of fluid circulating through the collector, F' is the collector efficiency factor, and h_{fi} is the convective heat transfer coefficient. The fluid temperature will vary in the direction of flow and is therefore a function of y (m). The collector efficiency factor is calculated by [7].

$$F' = \frac{1/U_L}{W\left[\frac{1}{U_L\left[D + (W - D)/F\right]} + \frac{1}{\pi D_i h_{fi}}\right]} \tag{16}$$

Calculation of the collector efficiency factor requires the fin efficiency value F. Traditionally this value is determined by carrying out a classical fin analysis on the solar thermal absorber which is assumed to be a fin of rectangular cross section. Given the simple geometry of the classic fin, F is calculated by an analytical expression. However due to the structural ribs required to stiffen the building integrated collector as shown by Figure 26, such an analysis may lead to non-negligible error. To quantify this variation, the finite difference method was applied to calculate the temperature distribution and fin efficiency for a simplified version of the BIT collector under study.

3.4.1 Nu*m*erical calculation of fin efficiency

Geometry of the BIT collector for which the temperature distribution is to be calculated is shown in the bottom of Figure 26. As the collector is made from 2mm thick aluminium, a one dimensional steady state analysis was deemed sufficient for this investigation (as is the common practice in assessing fin performance [156]).

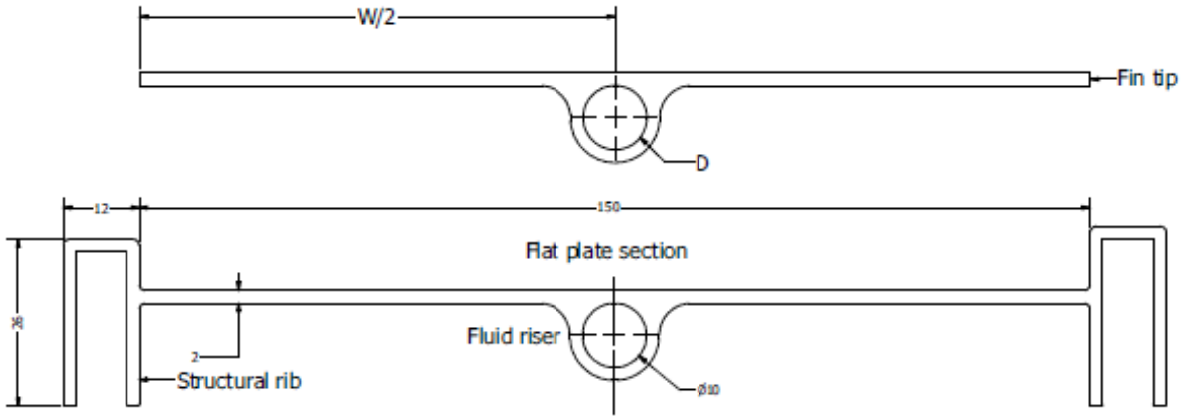

Figure 26 Comparison between the classical fin (top) and the simplified BIT collector designs.

A finite difference control volume analysis was performed for a nodal network structure illustrated in Figure 27. The structure modelled contained significantly more nodes than shown in this figure. As the BIT collector was taken to be symmetrical about a vertical axis through the fluid channel, only half of the geometry was required for the simulation. The red arrows shown in Figure 5 indicate the nodes under radiation flux and the node under convection heat transfer (at the line of symmetry). As incidental radiation is assumed to be normal to the collector, only horizontal surfaces were exposed to radiation in this study. Irradiance, G was taken to be 1000 W/m^2. All nodes were subject to heat loss, q_{loss}.

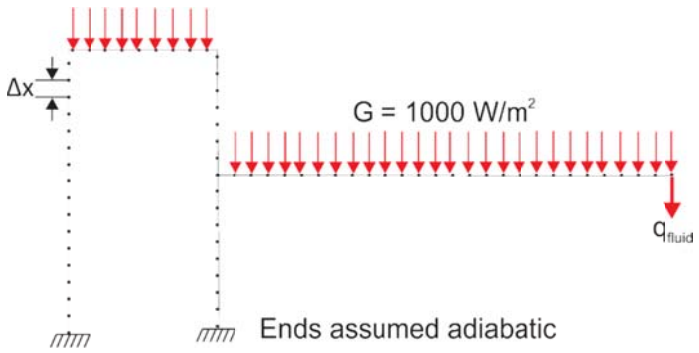

Figure 27 Nodal network of the BIT collector used to determine the temperature distribution using the finite difference method. Additionally, all nodes were subject to heat loss, qloss.

The analysis consists of four nodal types; I) nodes under radiation flux, II) nodes under no radiation flux, III) node under convection heat transfer (i.e. node at fluid riser), and IV) adiabatic nodes at structural rib ends. A control volume analysis for each node type is presented in the following section.

3.4.2 Control volume analysis

Proceeding sections detail the control volume analysis for the nodes shown in Figure 27 operating under each set of boundary conditions. Both overall energy and finite difference equations are provided.

3.4.2.1 Node under radiation flux

Figure 28 below shows the node (*i)* and control volume (dotted box) of width Δx exposed to radiation.

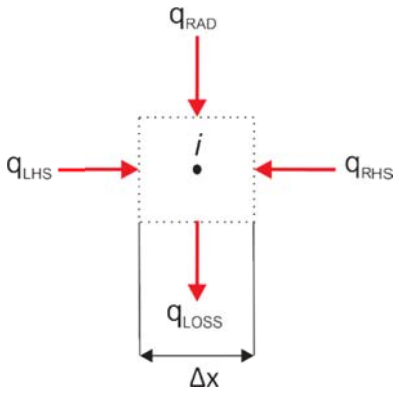

Figure 28 control volume for a node under incidental radiation.

A steady state energy balance yields,

$$q_{LHS} + q_{RHS} + q_{RAD} - q_{LOSS} = 0 \tag{17}$$

Where q_{LHS} and q_{RHS} represent conduction heat transfer with neighbouring nodes, q_{RAD} is radiation heat transfer to control volume, and q_{LOSS} represents heat loss to ambient. Substituting the relevant approximate rate equations (Fourier's Law) [157],

$$\frac{kA}{\Delta x}(T_{i-1} - T_i) + \frac{kA}{\Delta x}(T_{i+1} - T_i) + S\Delta x - U_L \Delta x(T_i - T_a) = 0 \qquad (18)$$

Where S is the absorbed radiation (W/m^2) and U_L is the overall heat loss of the collector coefficient ($W/m^2\ ^oC$). Procedure to calculate the overall heat loss coefficient will be presented in Section 2.2. As the collector panel length was assumed to be unity in the direction of fluid flow, the area A of the control volume perpendicular to conduction heat flux was taken to be equal to the value of fin thickness (δ). T_i represents the temperature of the node (and therefore the control volume), T_a is the ambient temperature, while T_{i-1} and T_{i+1} represent the temperature of nodes to the left and right respectively.

3.4.2.2 Node under no radiation flux

Figure 29 represents a control volume of the BIT collector under no radiation loading interacting with neighbouring nodes via conduction and heat loss to surroundings.

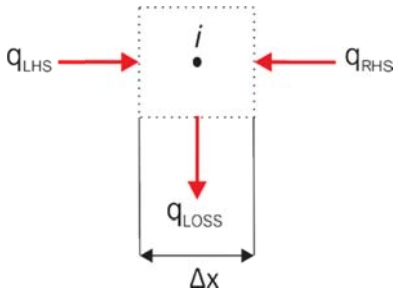

Figure 29 control volume for a node under no incidental radiation.

A steady state energy balance of the control volume shown by Figure 29 yields,

$$q_{LHS} + q_{RHS} - q_{LOSS} = 0 \tag{19}$$

$$\frac{kA}{\Delta x}(T_{i-1} - T_i) + \frac{kA}{\Delta x}(T_{i+1} - T_i) - U_L \Delta x (T_i - T_a) = 0 \tag{20}$$

3.4.2.3 Node under convection heat transfer

A single node (as indicated on the extreme right in Figure 27) is subject to both radiation and convective cooling due to fluid flow in the riser pipe in addition to conduction interaction with neighbouring nodes. Figure 30 represents the energy flow into this control volume.

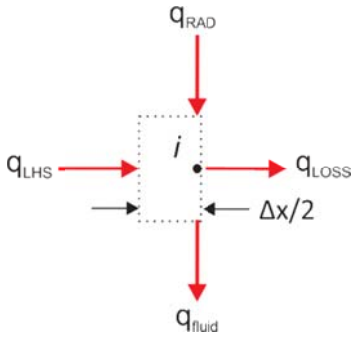

Figure 30 control volume for the node under incidental radiation and convective heat transfer.

An energy balance of the control volume shown by Figure 30 yields,

$$q_{LHS} + q_{RAD} - q_{LOSS} - q_{FLUID} = 0 \tag{21}$$

$$\frac{kA}{\Delta x}(T_{i-1} - T_i) + \frac{\Delta x}{2} S - \frac{\Delta x}{2} U_L (T_i - T_a) - \frac{h_{fi} \pi D}{2}(T_i - T_f) = 0 \tag{22}$$

Where T_f is the fluid temperature, D is the riser pipe diameter (m), and h_{fi} is the forced convection heat transfer coefficient(W/m^2 K) calculated by [156],

$$h_{fi} = \frac{Nuk}{D} \tag{23}$$

For a circular tube, the Nusselt number *Nu* is independent of velocity for laminar flow conditions but is dependent on the thermal boundary condition [156]. The value can be taken as either 4.36 and 3.66 for uniform surface heat flux and constant wall temperature conditions respectively [156]. In this work we assumed a Nusselt number of 4.36. For T_f = 20°C, the thermal conductivity value *k* was taken to be 0.6 W/m K [7]. For a pipe 0.01m in diameter, the heat transfer coefficient h_{fi} was calculated to be 260 W/m^2 K.

3.4.2.4 Nodes at adiabatic boundary conditions

The ends of the roof ribs were assumed to be adiabatic as indicated in Figure 27. For the control volume shown in Figure 31, only two energy flows are presented q_{LHS} and q_{LOSS} representing conduction with its neighbouring node and heat loss to ambient respectively. The energy balance and finite difference equations were determined to be,

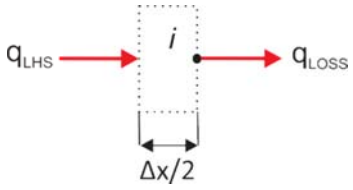

Figure 31 control volume for the nodes at rib ends.

$$q_{LHS} - q_{LOSS} = 0 \tag{24}$$

$$\frac{kA}{\Delta x}(T_{i-1} - T_i) - \frac{\Delta x}{2} U_L (T_i - T_a) = 0 \tag{25}$$

3.4.2.5 Calculation of the overall heat loss coefficient

In the analysis of solar thermal systems, it is useful to represent heat losses from the collector to its surroundings using an overall heat loss coefficient U_L in order to simplify the mathematics behind the analysis. The overall heat loss coefficient is the summation of heat losses experienced from the collector's top, edges, and bottom surfaces [7].

Given the unique design of the collector under study were it is integrated directly into the building envelope without a top cover, the procedure for calculating U_L will vary somewhat from that of a traditional solar thermal collector. Anderson et al. [74] determined the overall heat loss coefficient to be 22 W/m^2 K for an unglazed building integrated PVT collector very similar to the one considered in this study. This value was obtained considering that the building integrated collector is installed above an air-filled, triangular, enclosed attic in which the trapped air essentially acted as a layer of insulation. The value calculated for U_L obtained Anderson et al. was used for our study.

3.4.3 Calculation of temperature distribution *T(x)*

For N nodes, an N number of finite difference equations were developed based on the control volume analysis discussed in previous sections in order to determine N unknown temperatures. Finite difference equations presented in sections 2.11, 2.12, 2.13, and 2.14 were modified to fit the following matrix equation format [158]:

$$\underline{A}\,\underline{X}=\underline{b} \qquad (26)$$

Where $\underline{A}$ is a sparse-type matrix consisting of the unknown temperature coefficients, $\underline{X}$ is the vector of unknown temperatures to be found, and $\underline{b}$ is a vector of the corresponding constant terms for each control volume.

Using Matlab® software, matrix $\underline{A}$ and vector $\underline{b}$ were compiled using the finite difference equations previously discussed. The linear system of N equations was solved using Gaussian Elimination to obtain vector $\underline{X}$ of unknown temperatures. A comparison of the temperature distribution is made in Figure 32 between the BIT collector and a traditional flat plate collector. We can see at $x = 0$, the temperature of the BIT collector is somewhat lower due to additional heat losses through the ribs. Based on these results we can expect a reduction in the fin efficiency value of the BIT collector.

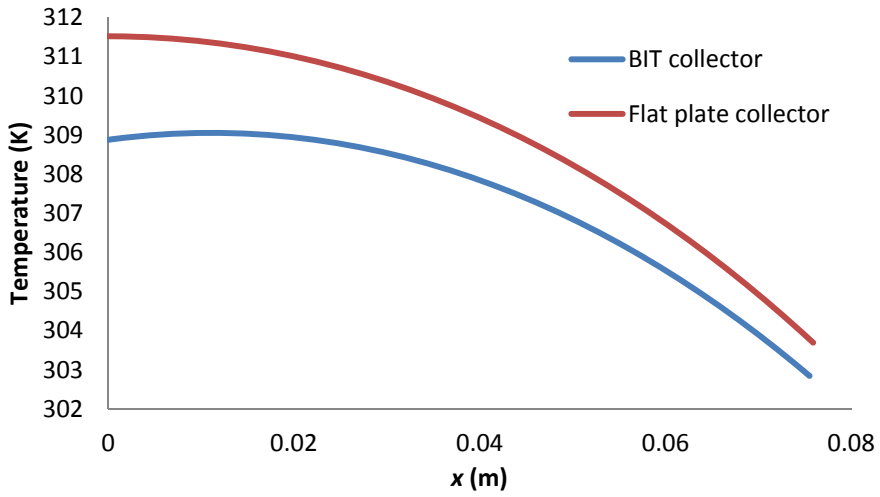

Figure 32 Temperature distribution for the BIT collector along the fin compared with the temperature distribution of a standard flat plate collector. Both sets of data were calculated numerically using the finite difference method.

3.4.4 Calculation of fin efficiency *F*

The fin efficiency for a straight fin with a rectangular profile under uniform radiation is calculated using Eq. (27). This equation is typically used for the analysis of the traditional flat plate solar thermal collector.

$$F = \frac{\tanh[m(W-D)/2]}{m(W-D)/2} \tag{27}$$

The calculation of the fin efficiency value depends on the boundary condition at the fin tip and the geometry of the fin. Eq. (27) assumes a straight, rectangular geometry and hence would not yield an accurate value for the BIT collector fin which must, therefore, be calculated numerically. The fin efficiency is defined as the ratio of the heat transfer away from the actual fin to the heat transfer away from an ideal fin [157]).

The energy conducted to the region of the fluid riser can be determined using Fourier's law. Using Eq. (28) below, the finite difference method is used to calculate conduction heat transfer through the fin above the riser. Where T_N represents the temperature of node N (at fluid riser) and T_{N-1} is the temperature of the adjacent node.

$$q'_{fin} = -k\delta \left.\frac{dT}{dx}\right|_{x=\frac{(W-D)}{2}} = k\delta \frac{T_{N-1} - T_N}{\Delta x} \tag{28}$$

The value obtained using Eq. (28) was multiplied by two as the value obtained represents conduction from one side of the riser tube only. The heat transfer value for the ideal fin was numerically calculated by setting the thermal conductivity of the fin to infinity.

$$F_{BIT} = \frac{q'_{fin}}{q'_{ideal}} \tag{29}$$

Inspecting Figure 32 we can see that the fin edge temperature for the BIT collector is lower compared to the values obtained using Eq. (1) due to conduction losses through the structural ribs. For the BIT collector, we numerically determined the fin efficiencies to be 0.88 while the fin efficiency for a traditional flat plate collector of equivalent characteristics was found to be 0.93, which represents a 5.2% drop in fin efficiency.

3.4.5 Module efficiency calculation

Fluid temperature for each riser, $T_f(y)$ needed for Eq. (15) is calculated by Eq. (30) [7].

$$T_f(y) = (T_{fi} - T_a - S/U_L)e^{\left(-\frac{U_L WF' y}{\dot{m}C_p}\right)} + T_a + S/U_L \quad (30)$$

The process of calculating the absorber temperature, *T(x, y)* begins by initially estimating a value for the mean fluid temperature (T_{fm}) so that fluid properties such as viscosity (μ_f), thermal conductivity (k) and Prandtl number (Pr) can be interpolated from tabulated data. The mean fluid temperature (T_{fm}) is calculated by Eq. (31).

$$T_{fm} = \frac{T_{fo} + T_{fi}}{2} \quad (31)$$

Where T_{fo} and T_{fi} represent the values of outlet and inlet fluid temperature respectively. In our study, the inlet fluid temperature, T_{fi} was kept constant at 20 °C. The outlet fluid temperature is found using Eq. (15) with y set to the length of the absorber.

Using the riser mass flow rates determined in our fluid flow analysis, the Reynolds number (Re_D) was calculated using Eq. (17) with the assumption that flow was steady and incompressible and within a pipe of uniform cross sectional area [7].

$$\mathrm{Re}_D = \frac{4\dot{m}}{\pi D \mu} \quad (32)$$

Where D is the diameter of riser pipe and μ is fluid viscosity. For values of $Re_D < 2300$, flow was considered laminar and fully developed. Conservative heat transfer coefficient values was calculated by making the constant wall temperature assumption [7]. Here, the Nusselt number (Nu) was taken to be 3.66 [159]. The convective heat transfer coefficient (h_{fi}) of fluid circulating in the riser may then be calculated by re-arranging Eq. (33).

$$Nu = \frac{h_{fi} D}{K} \quad (33)$$

Once the convective heat transfer coefficient, h_{fi} was found, the fin efficiency factor, F' and fluid temperature, $T_f(y)$ were calculated. With the new value of outlet fluid temperature found, the new value for mean fluid temperature, $T_{fm,i+1}$ was calculated using Eq. (16) and compared to the previous value of $T_{fm,i}$. The process of calculating F' and T_{fo} was repeated until the error in subsequent iterations was within a user specified tolerance. Final values of F' and T_f were then used to calculate the bond temperature (T_b) and absorber temperature (T) using Eq. (6) and Eq. (4) respectively. This process was repeated in Matlab for each of the 16 treatment combinations.

Finally once T_{fo} was found, the useful energy gain, Q_u was calculated using Eq. (34)

$$Q_u = mC_p(T_{fo} - T_{fi}) \tag{34}$$

Where m is the riser mass flow rate (calculated from our fluid analysis), and C_p is the specific heat of water (kJ/kg K). The thermal efficiency (η_{th}) can now be calculated using Eq. (35) for each module. All module efficiency values were then averaged to give the final array response.

$$\eta_{th} = \frac{Q_u}{GA_c} \tag{35}$$

3.5 Results and Discussion

The thermal efficiency values for each treatment combination are presented in Table 3 along with the levels for each factor. The objective of our analysis was to determine the ranking of the main effects and identify any significant secondary interactions. To achieve this aim a statistical analysis was carried out on the data presented in Table 3. An analysis of variance (ANOVA) study was carried out using Minitab 16 software.

Table 3 Response values (thermal efficiency of array) for each treatment combination investigated.

TC	A	B	C	D	Response

1	-1	-1	-1	-1	0.1007
2	1	-1	-1	-1	0.2016
3	-1	1	-1	-1	0.332
4	1	1	-1	-1	0.3557
5	-1	-1	1	-1	0.1604
6	1	-1	1	-1	0.2861
7	-1	1	1	-1	0.3381
8	1	1	1	-1	0.356
9	-1	-1	-1	1	0.1262
10	1	-1	-1	1	0.2507
11	-1	1	-1	1	0.3756
12	1	1	-1	1	0.3906
13	-1	-1	1	1	0.2757
14	1	-1	1	1	0.3259
15	-1	1	1	1	0.3795
16	1	1	1	1	0.3908

Figure 33 illustrates the Pareto plot [154] of main effects and secondary interactions. Higher order interactions were found to be insignificant and systematically removed in our study. The graph shows that all four main effects are significant at the 5 per cent significance level (i.e. $\alpha = 0.05$). Geometry of the array was shown to have greatest effect on the thermal efficiency followed by the manifold to riser ratio, mass flow rate, and the direction of flow in the manifolds. Interestingly we can see that in addition to the main effects, there is a strong interaction between the array geometry (Factor B) and the direction of flow in the manifold (Factor C), and also between the manifold to riser ratio (Factor A) and array geometry (Factor C). These results identify the need in the appropriate selection of the manifold to riser channel ratio and the direction of flow in the manifolds for a BIT collector of specified geometry.

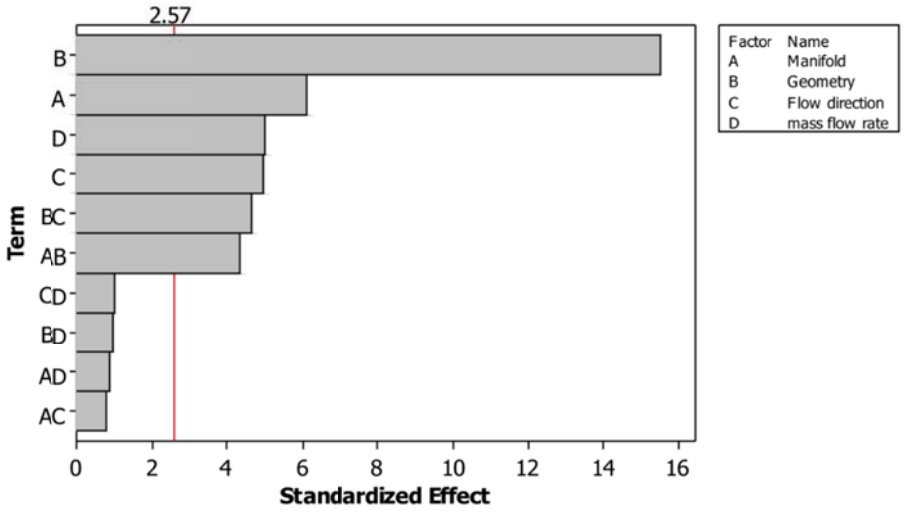

Figure 33 Pareto plot of effects at 5 per cent significance level.

The analysis of a 2^k factorial design makes the assumption that the observations are normal and independently distributed [155]. This assumption was validated by generating a normal probability plot of residuals shown by Figure 34. Inspecting this graph, we observe that the residuals fall approximately along the straight line supporting our assumption that the data has come from a normal distribution. We can also confirm that there are no obvious data points which stray away from the data group thus no outliers exist in our data.

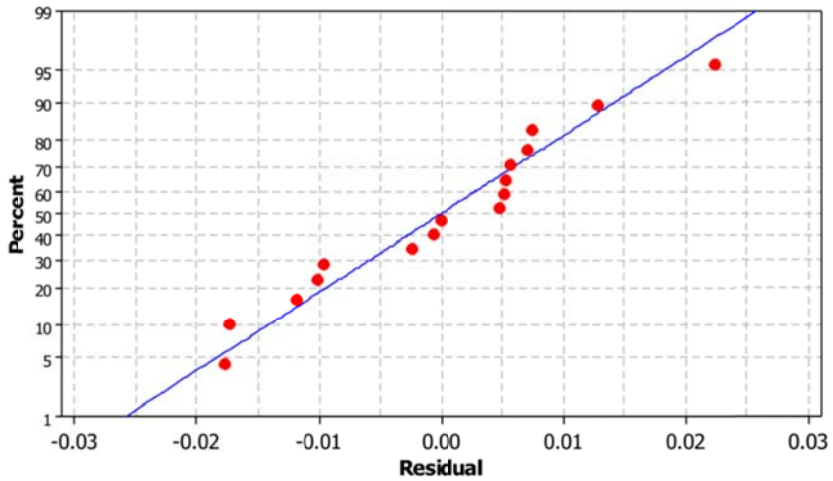

Figure 34 Normal probability plot.

A final data integrity check is to verify that the residuals are independent by plotting the Residual vs Order graph. Examining Figure 35, we can see residuals are randomly scattered about the x-axis and there is no pertinent trend. The residuals are therefore independent.

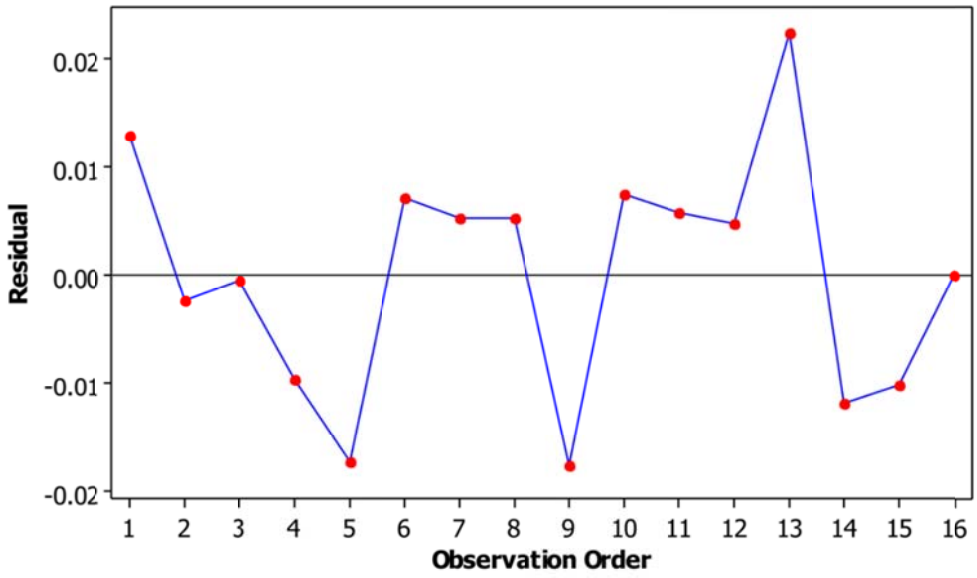

Figure 35 Residual versus order of the data.

3.6 Conclusion

In our study a two level full factorial experiment was designed to determine what effect four design factors and their interactions will have on the thermal efficiency of a building integrated thermal collector. A computational analysis was performed in order to approximate the fluid flow and corresponding temperature distribution of each of the 16 treatment combinations using a commercial FEA package and Matlab software. Furthermore, a numerical analysis was conducted to quantify the fin efficiency of a BIT collector using the finite difference method which revealed the BIT collector will suffer a 5% drop in fin efficiency due to additional fin tip heat losses through the structural ribs of the collector. From these results the thermal efficiency values were calculated for each module and averaged for each treatment factor. A statistical analysis revealed that the

array geometry will have the strongest influence, followed by the manifold to riser channel ratio, mass flow rate, and lastly the direction of flow in the manifold (i.e. parallel or reverse flow). Two secondary interactions were also found to be statistically significant at 5 per cent significance level. The array geometry and direction of flow in the manifold followed by the array geometry and the manifold to riser channel ratio interactions will both affect the thermal yield of a BIT collector.

The authors believe the research presented is valuable to those responsible in the design of BIT systems.

References

[1] M. Asif, T. Muneer, Energy supply, its demand and security issues for developed and emerging economies, Renewable and Sustainable Energy Reviews, 11 (2007) 1388-1413.

[2] W. Weiss, F. Mauthner, Solar heat worldwide markets and contributions to the energy supply 2010, in: Solar Heating & Cooling Programme, International Energy Agency, 2012.

[3] C. Corbin, J.Z. Zhiqiang, Experimental and numerical investigation on thermal and electrical performance of a building integrated photovoltaic-thermal collector system, Energy and Buildings, 42 (2010) 76-82.

[4] X.Q. Zhai, R.Z. Wang, Y.J. Dai, J.Y. Wu, Y.X. Xu, Q. Ma, Solar integrated energy system for a green building, Energy and Buildings, 39 (2007) 985-993.

[5] S. Medved, C. Arkar, B. Cerne, A large-panel unglazed roof-integrated liquid solar collector-energy and economic evaluation, Solar Energy, 75 (2003) 455-467.

[6] J.P. Chiou, The effect of nonuniform fluid flow distribution on the thermal performance of solar collector, Solar Energy, 29 (1982) 487-502.

[7] S.A. Wang, L.G. Wu, Analysis and performance of flat-plate solar collector arrays, Solar Energy, 45 (1990) 71-78.

[8] F. Ghani, M. Duke, J.K. Carson, Effect of flow distribution on the photovoltaic performance of a building integrated photovolatic/thermal (BIPVT) collector, Solar Energy, 86 (2012) 1518-1530.

[9] G.F. Jones, N.L. Lior, Flow distribution in manifold solar collectors with negligible buoyancy effects, Solar Energy, 52 (1994) 289-300.

[10] P. Mathews, Design of experiments with Minitab, ASQ Quality Press, US, 2005.

[11] J. Anthony, Design of experiments for engineers and scientists, Butterworth-Heinemann, Oxford, 2008.

[12] J.A. Duffie, W.A. Beckman, Solar engineering of thermal processes, 3rd ed., John Wiley & Sons, New Jersey, 2006.

[13] T.N. Anderson, M. Duke, G.L. Morrison, J.K. Carson, Performance of a building integrated photovoltaic/thermal (BIPVT) solar collector, Solar Energy, 83 (2009) 445-455.

[14] F.P. Incropera, D.P. DeWitt, T.L. Bergman, A.S. Lavine, Fundamentals of Heat and Mass Transfer, John Wiley & Sons, New York, 2006.

[15] G. Nellis, S.A. Klein, Heat Transfer, Cambridge University Press, New York, 2009.

[16] G.E. Myers, Analytical methods in conduction heat transfer, Genium Publishing Corp, US, 1987.

[17] W.M. Kays, M.E. Crawford, Convective Heat and Mass Transfer, 3rd ed. ed., McGraw-Hill, New York, 1993.

Chapter 4: Numerical determination of parasitic resistances of a solar cell using the Lambert *W*-function

4.0 Introduction

Chapter three demonstrated that several parameters which are expected to vary considerably for the case of building integrated solar collector, will have a statistically proven influence over its thermal performance. As this chapter only examined fluid flow and heat transfer, further work is necessary to understand what effect flow mal-distribution will have on the photovoltaic output due to the negative impact of temperature for the building integrated PVT collector. Similar to the methodology applied in the previous chapter, a number of scenarios must be investigated to examine how influential this issue will be on photovoltaic output for a building integrated solar collector. An experimental investigation was therefore not feasible, consequently a mathematical approach must be employed. A mathematical model of the photovoltaic system which captured the effect of temperature was therefore developed and added to the model created in the previous chapter.

Chapter 2 outlined the procedure commonly utilised to simulate the non-linear behaviour of a crystalline silicon solar cell. It was discussed that the accuracy of a photovoltaic model is heavily dependent on parameter selection. For the popular single diode five parameter model which shall implemented in this study, five parameters (R_s, R_{sh}, n, I_0, I_{ph}) in total must be found. A number of methods currently exist to achieve this task as discussed in Chapter 2 ranging in complexity and accuracy. In this chapter a unique method for calculating two of these parameters is presented.

The method presented here for calculating two parameter values, R_s and R_{sh}, is based on matching the mathematical output of the single diode equation with data provided by the manufacturer. This is achieved by using a multi-dimensional version of the Newton-

Raphson method and equations which express the current-voltage characteristics of a solar cell using the Lambert *W*-function.

Validation of the method was carried out by comparing the values obtained with this method against values published in the literature. Additionally two other published methods were used to calculate the resistance values for comparison. Values were found to be calculated with much higher accuracy using this method and unlike other methods, the values for R_s and R_{sh} were found to approach final values in a rapid and convergent manner. Additionally the method can be employed using only data provided by the manufacturer, therefore avoiding the need of expensive electrical equipment used for acquiring the characteristics current-voltage curve of the device under study.

Research carried out in this chapter provided a necessary step into the development of the mathematical model used to quantify the photovoltaic output of a BIPVT collector. This model can then be applied for the analysis of non-uniform flow distribution conditions.

4.1 Journal Paper: Numerical determination of parasitic resistances of a solar cell using the Lambert *W*-function

Available online at www.sciencedirect.com
ScienceDirect
Solar Energy 85 (2011) 2386–2394
SOLAR ENERGY
www.elsevier.com/locate/solener

Numerical determination of parasitic resistances of a solar cell using the Lambert W-function

F. Ghani *, M. Duke

Department of Engineering, University of Waikato, Hamilton 3240, New Zealand

Received 10 February 2011; received in revised form 4 July 2011; accepted 5 July 2011
Available online 28 July 2011

Communicated by: Associate Editor Arturo Morales-Acevedo

Abstract

Several methods are currently available to determine the values of series and shunt resistance of a solar cell. A new method is presented here to numerically locate these values using the popular Newton–Raphson technique at maximum power point. Equations based on the Lambert W-function and their partial derivatives are provided so that all calculations may be performed in a Matlab or similar environment. The results of this new method are presented and compared with two published methods and the analytically obtained for a blue and grey type solar cell in earlier work (Charles et al., 1981). Additionally, three modules of various type (single, poly, and amorphous crystalline) were investigated. Values determined agreed with experimentally verified results and were obtained with quadratic convergence in all instances provided initial estimates of the roots were within vicinity of the actual roots.

Keywords: Series resistance; Shunt resistance; Lambert W-function; Solar cell modelling; Newton–Raphson; Parameter evaluation

1. Introduction

Modelling and simulation of a photovoltaic systems is typically performed in order to optimise the performance of a system prior to installation. Photovoltaic module manufacturers specify the operating characteristics of their module at standard test conditions (STC) where irradiance and temperature are held constant. Generally speaking, the following characteristics of the cell/module are often published by the manufacturer; open circuit voltage (V_{oc}), short circuit current (I_{sc}), maximum power point (P_{max}), maximum power voltage (V_{mp}) and current (I_{mp}), and temperature coefficients for both short circuit current and open circuit voltage. In reality however, the photovoltaic system will be subject to largely varying environmental conditions resulting in operation outside these published values. Factors including but not limited to irradiance, ambient temperature, wind speed, etc. will have influence on the output of any photovoltaic system. To quantify the output of a photovoltaic system under such circumstances, the behaviour of a solar energy system can be approximated with an equivalent electric circuit. A number of models exist such as the two diode model (Macabebe et al., 2011) which takes into account the recombination process influencing the behaviour of the current–voltage characteristics. The simpler single diode model such as the one shown in Fig. 1 on the other hand has shown to offer an acceptable compromise between simplicity and accuracy (Carrero et al., 2007). The behaviour of such a cell is mathematically defined by,

$$i = I_{ph} - \frac{V + R_s i}{R_{sh}} - I_0\left[e^{\frac{V + R_s i}{nV_t}} - 1\right] \quad (1)$$

where i and V represent the current and voltage of the cell, I_{ph} is the photogenerated current, I_0 the reverse saturation current of the equivalent diode, n is the diode ideality factor of cell or module, R_s and R_{sh} are the series and shunt

* Corresponding author. Tel.: +64 220180398.
E-mail address: fag2@waikato.ac.nz (F. Ghani).

0038-092X/$ - see front matter © 2011 Elsevier Ltd. All rights reserved.
doi:10.1016/j.solener.2011.07.001

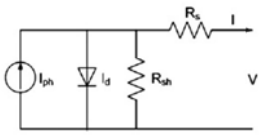

Fig. 1. Single diode equivalent circuit model of a solar cell.

resistances of the cell respectively, and V_{th} is the thermal voltage of the cell ($k_B T/q$). Here, k_B is the Boltzmann constant (1.3806×10^{-23} J/K), T is the absolute temperature (K), and q is the electron charge (1.6022×10^{-19} C).

Parameters necessary for Eq. (1) which have not been explicitly provided such as R_s and R_{sh}, must be extracted from the supplied manufacturer datasheet or determined experimentally. Only the former shall be discussed in this paper.

Evaluation of series and shunt resistance values is by no means a trivial task, consequently a number of methods have been proposed and reviewed by authors (Bashahu and Habyarimana, 1995; Chegaar et al., 2004; de Blas et al., 2002; Jia et al., 1988; Psych et al., 2007). One technique, is to extract parameters, including series resistance from a single diode lumped circuit model using current–voltage data experimentally obtained (Bouzidi et al., 2007). In this method, numerical least squares techniques are employed to find the values of 'C factors' to describe voltage explicitly in terms of current. Another author (Xiao et al., 2004) suggested to determine series resistance iteratively knowing the derivative of power with respect to voltage is equal to zero. This method however did not take into account the effect of shunt resistance.

Some authors (Carrero et al., 2010; Villalva et al., 2009) have proposed to find the values of loss resistances at maximum power point (MPP) considering photovoltaic systems are generally implemented with maximum power point tracking (MPPT) hardware. The method of Villalva et al. is based on finding values of R_s and R_{sh} using an iterative process given that a unique pair of values for R_s and R_{sh} will match the value of P_{max} provided by the manufacturer. This approach involves setting the series resistance to zero initially and calculating the value of R_{sh} using a given relationship. The value for power is calculated and compared with that of the manufacturer. If there is a mismatch within a specified range, the value of R_s is incremented. This process is repeated until the error falls below a threshold value.

The method of Carrero et al. takes a similar approach to the one just discussed. Using several equations, values of parasitic resistance are determined at maximum power point. This method makes the assumption of a high value for shunt resistance initially. Based on this assumption, an expression for R_s is provided which is primarily a function of manufacturer specified data, an initial estimate for R_s and the diode ideality factor, n (assumed to be equal to 1 in their study). As an estimate for R_s is required at the beginning, the process is repeated several times until the value for R_s has converged. This method is simple and can be performed without aid of a computer. Both the methods of Villalva et al. and Carrero et al. have the benefit that they chiefly only require data specified by the manufacturer.

This paper describes the methodology to determine the values of R_s and R_{sh} at maximum power point using a multivariable version of the Newton–Raphson method. The Newton–Raphson method offers the advantage of rapid convergence but this method can only be implemented if the first order derivative can be derived. The transcendental nature of Eq. (1) where current is an implicit function of both current and voltage makes this task difficult. An alternative to Eq. (1) has been proposed which describes the behaviour of the PV system using the Lambert W-function (Jain and Kapoor, 2004).

$$i = -\frac{V}{R_s + R_{sh}} - \frac{LambertW\left(\frac{R_s I_0 R_{sh} e^{\left(\frac{R_{sh}(R_s I_{ph} + R_s I_0 + V)}{nV_{th}(R_s + R_{sh})}\right)}}{nV_{th}(R_s + R_{sh})}\right) nV_{th}}{R_s} + \frac{R_{sh}(I_0 - I_{ph})}{R_s + R_{sh}} \quad (2)$$

Eq. (2) is now an explicit function of voltage only, and can therefore be determined analytically avoiding the numeric approximations necessary to solve Eq. (1). The approach of modelling with the Lambert W-function is attractive based on the simplification made to the numerical analysis of large photovoltaic systems, particularly for systems under the effects of mismatch losses such as shading and temperature (Petrone et al., 2007; Picault et al., 2010). An additional advantage of modelling with the Lambert W-function is its easy differentiability (Barry et al., 1995; Corless et al., 1996) permitting the use of open methods to locate the roots of these non-linear equations numerically. This paper will provide the methodology and the necessary equations to find values of R_s and R_{sh} at maximum power point using the Newton–Raphson method. Results obtained from this method are compared with published values for a blue and grey type solar cell (Charles et al., 1981) and for three modules of different type (Ikegami et al., 2001). Values obtained using the methods published by Villalva et al. and Carrero et al. were also determined for comparison.

2. Theory

Similar to methods discussed in the previous section, the values of R_s and R_{sh} are to be determined at the maximum power point (MPP). Fig. 2 plots the power–voltage characteristics of a typical solar cell for various values of series resistance (R_{sh} constant) using Eq. (2). Increasing series resistance has the overall effect of reducing the maximum power output (P_{max}). At this point, values for current and voltage are typically specified by the

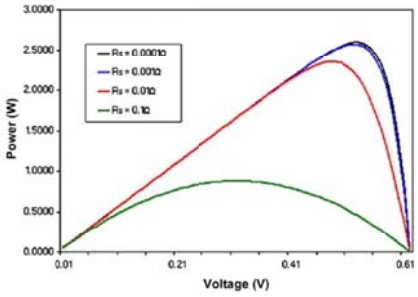

Fig. 2. Power–Voltage curve for a typical solar cell with varying values of R_s (R_{sh} constant).

manufacturer (I_{mp} and V_{mp} respectively). The proposed method begins by first examining the current–voltage relationship of a solar cell. By substituting values I_{mp} and V_{mp} obtained from the manufacturers datasheets for i and V respectively into Eq. (2) and re-arranging to equate to zero, we define expression z at maximum power point.

$$z \equiv \frac{R_{sh}(I_0 + I_{ph})}{(R_s + R_{sh})} - \frac{V_{mp}}{(R_s + R_{sh})} - \frac{nV_{th}}{R_s} LambertW(\theta_1) - I_{MP} = 0 \tag{3}$$

where θ_1 is given by,

$$\theta_1 = \frac{R_s I_0 R_{sh}}{nV_{th}(R_s + R_{sh})} e^{\frac{R_{sh}(R_s I_{ph} + R_s I_0 + V_{mp})}{nV_{th}(R_s + R_{sh})}} \tag{4}$$

Studying Eq. (3), we can see that all values with the exceptions of R_s, R_{sh}, and n can be obtained either from datasheets provided by the manufacturer, or approximated by expressions published in earlier work. If the diode ideality factor, n is known we have two unknowns (R_s and R_{sh}) which must be found. A second expression is therefore needed to solve for R_s and R_{sh}.

Examining the power–voltage data set of Fig. 2, it is evident that a global maximum exists at MPP. Thus the partial derivative of power (P) with respect to voltage (and current) is equal to zero.

$$\frac{\partial P}{\partial i} = 0_{\,i=I_{mp}}, \quad \frac{\partial P}{\partial V} = 0_{\,V=V_{mp}} \tag{5}$$

Equations for the partial derivative of power with respect to i and V have been published in earlier work (Jain and Kapoor, 2004). Similar to Eq. (3) we use the partial derivative of P with respect to current to define expression w at MPP by substituting values for i and V with I_{mp} and V_{mp} respectively giving us our second expression.

$$w \equiv R_{sh}I_{ph} + R_{sh}I_0 - 2I_{mp}R_s - 2I_{mp}R_{sh} - nV_{th}LambertW(\theta_2) - I_{mp}R_{sh}\left\{\frac{LambertW(\theta_2)}{[1 + LambertW(\theta_2)]}\right\} = 0 \tag{6}$$

where θ_2 is given by,

$$\theta_2 = \frac{I_0 R_{sh}}{nV_{th}} e^{\frac{R_{sh}(-I_{mp} - I_{ph} - I_0)}{nV_{th}}} \tag{7}$$

If the diode ideality factor n is arbitrarily selected (typically a value between 1 and 2) (Faulkner and Buckingham, 1968), R_s and R_{sh} can be numerically located by solving non-linear expressions z and w. A multidimensional version of the Newton–Raphson method shown below was used to iteratively solve for R_s and R_{sh} (Chapra and Canale, 2002; Press et al., 2002).

$$R_{s,i+1} = R_{s,i} - \frac{z_i \frac{\partial w_i}{\partial R_{sh}} - w_i \frac{\partial z_i}{\partial R_{sh}}}{\frac{\partial z_i}{\partial R_s}\frac{\partial w_i}{\partial R_{sh}} - \frac{\partial z_i}{\partial R_{sh}}\frac{\partial w_i}{\partial R_s}} \tag{8}$$

$$R_{sh,i+1} = R_{sh,i} - \frac{w_i \frac{\partial z_i}{\partial R_s} - z_i \frac{\partial w_i}{\partial R_s}}{\frac{\partial z_i}{\partial R_s}\frac{\partial w_i}{\partial R_{sh}} - \frac{\partial z_i}{\partial R_{sh}}\frac{\partial w_i}{\partial R_s}} \tag{9}$$

Beginning with initial estimates $R_{s,i}$ and $R_{sh,i}$, new values $R_{s,i+1}$ and $R_{sh,i+1}$ converging towards the root are found by applying equations Eqs. (8) and (9). The partial derivatives necessary to perform these calculations are given below.

$$\frac{\partial z}{\partial R_s} = \frac{V_{mp}}{(R_s + R_{sh})^2} - \frac{(R_{sh}I_0 - R_{sh}I_{ph})}{(R_s + R_{sh})^2} + \frac{nV_{th}}{R_s^2} LambertW(\theta_1) - \frac{nV_{th}}{R_s} \times \frac{LambertW(\theta_1)}{[1 + LambertW(\theta_1)]\theta_1} \frac{\partial \theta_1}{\partial R_s} \tag{10}$$

$$\frac{\partial \theta_1}{\partial R_s} = \frac{I_0 R_{sh}(nV_{th}R_s + nV_{th}R_{sh}) - nV_{th}(R_s I_0 R_{sh})}{(nV_{th}R_s + nV_{th}R_{sh})^2} + \frac{R_s I_0 R_{sh}}{nV_{th}(R_s - R_{sh})} \times \frac{(R_{sh}I_{ph} + R_{sh}I_0)(nV_{th}R_s + nV_{th}R_{sh}) - nV_{th}(R_{sh}R_s I_{ph} + R_{sh}R_s I_0 + R_{sh}V_{mp})}{[nV_{th}(R_s + R_{sh})]^2} e^{\frac{R_{sh}(R_s I_{ph} + R_s I_0 + V_{mp})}{nV_{th}(R_s + R_{sh})}} \tag{11}$$

$$\frac{\partial z}{\partial R_{sh}} = \frac{V_{mp}}{(R_s + R_{sh})^2} - \frac{(I_0 + I_{ph})(R_s + R_{sh}) - (R_{sh}I_0 + R_{sh}I_{ph})}{(R_s + R_{sh})^2} - \frac{nV_{th}}{R_s} \frac{LambertW(\theta_1)}{[1 + LambertW(\theta_1)]\theta_1} \frac{\partial \theta_1}{\partial R_{sh}} \tag{12}$$

$$\frac{\partial\theta_1}{\partial R_{sh}} = \frac{R_s I_0 (nV_{th}R_s + nV_{th}R_{sh}) - nV_{th}(R_s I_0 R_{sh})}{[nV_{th}(R_s + R_{sh})]^2} \cdot e^{\frac{R_{sh}(R_s I_{ph} - R_s I_0 - V_{mp})}{nV_{th}(R_s + R_{sh})}} + \frac{R_s I_0 R_{sh}}{nV_{th}(R_s + R_{sh})} \times \frac{(R_s I_{ph} - R_s I_0 + V_{mp})(nV_{th}R_s + nV_{th}R_{sh}) - nV_{th}(R_{sh}R_s I_{ph} + R_{sh}R_s I_0 + R_{sh}V_{mp})}{(nV_{th}R_s - nV_{th}R_{sh})^2} e^{\frac{R_{sh}(R_s I_{ph} + R_s I_0 - V_{mp})}{nV_{th}(R_s + R_{sh})}} \quad (13)$$

$$\frac{\partial w}{\partial R_s} = -2I_{mp} \quad (14)$$

$$\frac{\partial w}{\partial R_{sh}} = I_{ph} + I_0 - 2I_{mp} - V_{th}\left\{\frac{LambertW(\theta_2)}{[1 + LambertW(\theta_2)]\theta_2}\frac{\partial\theta_2}{\partial R_{sh}}\right\} + I_{mp}\left\{\frac{LambertW(\theta_2)}{[1 + LambertW(\theta_2)]\theta_2}\right\} + I_{mp}R_{sh}\left\{\frac{LambertW(\theta_2)}{[1 + LambertW(\theta_2)]^3\theta_2}\frac{\partial\theta_2}{\partial R_{sh}}\right\} \quad (15)$$

$$\frac{\partial\theta_2}{\partial R_{sh}} = \frac{I_0}{nV_{th}} e^{\frac{R_{sh}(-I_{mp} - I_{ph} - I_0)}{nV_{th}}}\left\{1 - \frac{R_{sh}(-I_{mp} - I_{ph} - I_0)}{nV_{th}}\right\} \quad (16)$$

The popular Newton–Raphson method is known to offer an elegant method of locating the roots of non-linear equations with quadratic convergence provided the initial estimates ($R_{s,i}$ and $R_{sh,i}$) are located within the vicinity of the actual roots (Press et al., 2002). Equally well known is its failure to converge should the initial estimate lie far from the actual root and/or the presence of a local maximum or minimum lying between an initial estimate and the root. To avoid this scenario, a contour plot of expressions z and w (with R_s and R_{sh} the independent variables) based on the properties of the cell under study can be created. Such plots can be readily generated in Matlab using the standard *meshgrid* and *contour* functions. Generating the contour map will confirm the existence of the root (intersection of zero contours) and also reveal its approximate location which can be used to start the analysis. The contour plots of the blue and grey cells (for properties see Table 1) used to evaluate the proposed method are shown in Figs. 3 and 4 respectively.

The contour plots of Figs. 3 and 4 can be interpreted in the following manner: (1) locate intersection of zero contours for functions z and w, (2) x-axis co-ordinate of intersection is the approximate value for series resistance, and (3) y-axis co-ordinate of intersection is the approximate value for shunt resistance. Using values in the vicinity of this area will result in rapid convergence. This step however may be avoided if an approximate value for series and shunt resistance is known.

Table 1
Characteristics of the blue and grey cells used for our analysis (Charles et al., 1981).

Parameter	Blue solar cell	Grey solar cell
n	1.51 + 0.07	1.72 − 0.08
V_{mp} (V)	0.433	0.387
I_{mp} (A)	0.0934	0.485
P_{max} (W)	0.0404	0.188
FF	0.737	0.638
T (K)	300	307

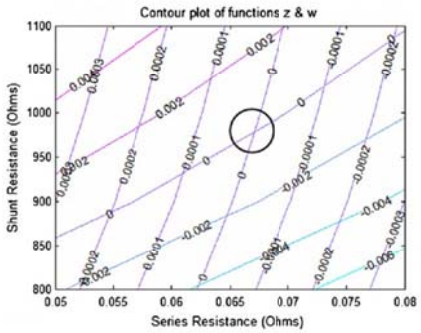

Fig. 3. Contour maps of functions z and w for the blue cell based on data supplied by manufacturer. Intersection of zero contours reveals approximate values for R_s and R_{sh} which can be used to begin the numerical analysis.

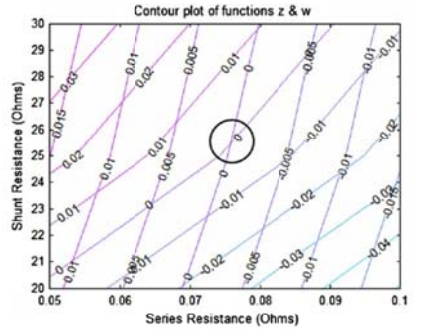

Fig. 4. Contour maps of functions z and w for the grey cell based on data supplied by manufacturer. Intersection of zero contours reveals approximate values for R_s and R_{sh} which can be used to begin the numerical analysis.

3. Calculations

The proposed method shall be used to determine the values for series and shunt resistance at maximum power point for two cells (a blue and grey type) and three modules (c-Si, pc-Si, and a-Si types). For the analysis of the blue and grey cells, the results published in earlier work (Charles et al., 1981) which were confirmed to be within 1% of experimental values, will be used as the analysis benchmark. The second part of our study will involve the analysis of three modules with the results obtained compared against published work (Ikegami et al., 2001). For comparison, the methods of Villalva et al. and Carrero et al. shall also be used to determine the values of loss resistances for the blue and grey cells.

Additional to the values obtained from the manufacturers datasheet, we must calculate the photogenerated current (I_{ph}) and the diode saturation current (I_0). The photogenerated current of the solar cell (I_{ph}) is assumed to be equal to short circuit current (I_{sc}) (Chenni et al., 2007). The diode saturation current can be determined by (De Soto et al., 2006),

$$I_0 = I_{0,n}\left(\frac{T_n}{T}\right)^3 e^{\left[\frac{qE_g}{nk}\left(\frac{1}{T_n}-\frac{1}{T}\right)\right]} \tag{17}$$

where T and T_n are the actual and nominal cell temperatures respectively in Kelvin, E_g is the bandgap energy of the semiconductor ($E_g = 1.12$ eV for silicon at 25 °C) and $I_{0,n}$ is the saturation current at nominal condition given by (De Soto et al., 2006),

$$I_{0,n} = \frac{I_{sc,n}}{e^{\left(\frac{V_{oc,n}}{aV_{t,n}}\right)} - 1} \tag{18}$$

The algorithm of the method proposed to determine the values of R_s and R_{sh} is summarised by Fig. 5.

Eqs. (3), (4) and (6)–(16) were coded into Matlab to determine values of z and w and their partial derivatives. Matlab is able to determine values of the Lambert function using the *lambertw(x)* function. A *while* loop structure was used to stop iterations once the error was below an arbitrarily selected value. As the aim is to determine the values of R_s and R_{sh} which make expressions z and w zero, error is defined as the maximum absolute value obtained from these two expressions. That is,

$$\varepsilon = \max[|z|, |w|] \tag{19}$$

For our investigation we will initially set ε to 1×10^{-7}. The influence of this value on the analysis will be discussed in Section 4. The proceeding sections will detail the parameters of the devices studied.

3.1. Blue and grey cell analysis parameters

The properties of the blue and grey type cells whose loss resistances are to be calculated are given in Table 1.

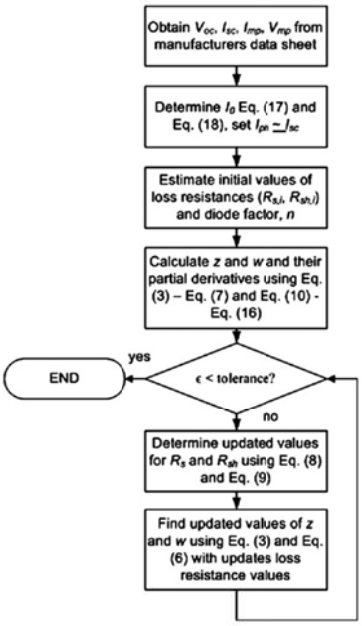

Fig. 5. Algorithm of proposed method to determine values of series and shunt resistance values at maximum power point.

Contour plots shown (Figs. 3 and 4) confirm for both cells that a unique solution exists for R_s and R_{sh} which permit the model output of the cell to equal the experimentally obtained maximum power point. We know this as there exists only one intersection of zero contours for each cell. Additionally the contour plots reveal the approximate location of the roots and therefore the initial pair set ($R_{s,i}$, $R_{sh,i}$) to be (0.065, 950) and (0.08, 25) for the blue cell and grey cell respectively. These values will be used to initiate the analysis.

3.2. Single, polycrystalline, and amorphous modules analysis parameters

In addition to the analysis of the blue and grey cells, the loss resistances of three modules (single, poly, and

Table 2
Characteristics of three modules whose loss resistances are to be found (Ikegami et al., 2001).

Parameter	Single-crystalline	Polycrystalline	Amorphous
n	49.53	46.6	104.95
V_{mp} (V)	14.7	14.8	15.1
I_{mp} (A)	3.18	2.88	1.53
FF (%)	68.6	70.6	57.9
T (K)	321.3	323.1	309.5

amorphous) with operating characteristics given in Table 2 shall be found.

4. Results and discussion

An approach to determine the parasitic resistance values R_s and R_{sh} using a multidimensional version of the Newton–Raphson method has been made for devices of varying type using the method outlined in the previous section. Predominantly using data available from the manufacturer (I_{mp} and V_{mp}); values for R_s and R_{sh} were found which permit the model output to equal the experimentally obtained value of maximum power (P_{max}). Results and discussion for the blue and grey cells will first be presented followed by the analysis of the single-crystalline, poly-crystalline, and amorphous modules.

4.1. Analysis of blue and grey cells

The calculated results of Charles et al. were used as the analysis benchmark as these results have been experimentally verified and found to be on average within 1% accuracy. Tables 3 and 4 summarise results obtained for the analysis of a blue and grey type solar cell respectively using the proposed, Villalva et al., and Carrero et al. methods.

From the results presented in Tables 3 and 4, we can see that all values obtained using the proposed method matched (within specified tolerance) the results of Charles et al. The results of the alternative methods however varied significantly. Examining each method individually, the outcome of the Villalva et al. method was that all values were well outside tolerance in all cases. For the grey cell, the method of Carrero et al. was effective to determine the value of series resistance but marginally outside tolerance for the value of shunt resistance. Despite the large variation in characteristics of the blue and grey cells, the proposed Newton–Raphson method consistently produced accurate results. Additional to its accuracy, the proposed method demonstrated its ability to find values in a stable and convergent manner. This is made clear from Figs. 6 and 7 which plot values for R_s and R_{sh} with each iteration respectively for the blue cell as an example.

All methods studied here are based on finding values of R_s and R_{sh} which permit the model output at P_{max} to equal the experimentally acquired value of maximum power.

Table 3
Comparison between analytical results of Charles et al. and the proposed method for the blue cell.

Parameter	Benchmark[a]	Method 1[b]	Method 2[c]	Method 3[d]
R_s (Ω)	0.07 ± 0.009	0.0671	0.002	0.0207
R_{sh} (Ω)	1000 ± 50	977	253.65	256.41

[a] (Charles et al., 1981).
[b] Proposed method.
[c] (Villalva et al., 2009).
[d] (Carrero et al., 2010).

Table 4
Comparison between analytical results of Charles et al. and the proposed method for the grey cell.

Parameter	Benchmark[a]	Method 1[b]	Method 2[c]	Method 3[d]
R_s Ω	0.08 ± 0.01	0.0784	0.0559	0.0841
R_{sh} Ω	26 ± 1	26.09	14.109	24.303

[a] (Charles et al., 1981).
[b] Method proposed.
[c] (Villalva et al., 2009).
[d] (Carrero et al., 2010).

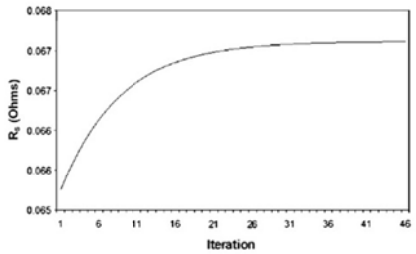

Fig. 6. Values for R_s for each iteration for the blue cell using the proposed Newton Raphson method.

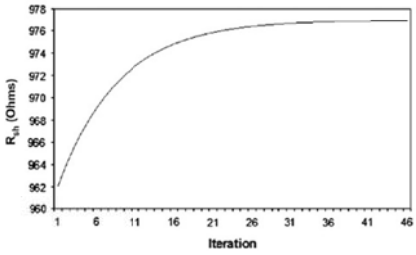

Fig. 7. Values for R_{sh} for each iteration for the blue cell using the proposed Newton–Raphson method.

Using Eq. (2), current was calculated based on the loss resistances determined from each of the four methods for the blue and grey cells. The power output of the cell was then found simply by,

$$P = iV \tag{20}$$

For the method of Charles et al. values for $R_s = 0.07\ \Omega$ and $R_{sh} = 1000\ \Omega$ for the blue cell and $R_s = 0.08\ \Omega$ and $R_{sh} = 26\ \Omega$ for the grey cell were used. To understand the significance of the large variation in values obtained for R_s and R_{sh} from each of the methods studied, Eq. (20) was used to determine the maximum power output for varying levels of irradiance (G). This was carried out as the value of loss resistances has been shown to have an effect on the module

Table 5
Values calculated for maximum power output using Eq. (2) based on loss resistance values obtained from each of the methods studied for the blue cell. Relative error to values for Charles et al. are also given.

G (W/m^2)	Benchmark (Charles et al., 1981)	Method 1 proposed		Method 2 (Villalva et al., 2009)		Method 3 (Carrero et al., 2010)	
	P_{max} (W)	P_{max} (W)	Error (%)	P_{max} (W)	Error (%)	P_{max} (W)	Error (%)
1000	0.0404	0.0404	0.00	0.0405	0.25	0.0403	0.25
800	0.0318	0.0318	0.00	0.0316	0.63	0.0315	0.94
600	0.0232	0.0232	0.00	0.0229	1.29	0.0229	1.29
400	0.0149	0.0149	0.00	0.0145	2.68	0.0145	2.68
200	0.0069	0.0069	0.00	0.0065	5.80	0.0065	5.80

Table 6
Values calculated for maximum power output using Eq. (2) based on loss resistance values obtained from each of the methods studied for the grey cell. Relative error to values for Charles et al. are also given.

G (W/m^2)	Benchmark (Charles et al., 1981)	Method 1 proposed		Method 2 (Villalva et al., 2009)		Method 3 (Carrero et al., 2010)	
	P_{max} (W)	P_{max} (W)	Error (%)	P_{max} (W)	Error (%)	P_{max} (W)	Error (%)
1000	0.1877	0.1877	0.00	0.1879	0.11	0.1859	0.96
800	0.1482	0.1482	0.00	0.1467	1.01	0.147	0.81
600	0.1085	0.1085	0.00	0.1056	2.67	0.1076	0.83
400	0.0688	0.0688	0.00	0.0652	5.23	0.0682	0.87
200	0.0302	0.0302	0.00	0.0267	11.59	0.0298	1.32

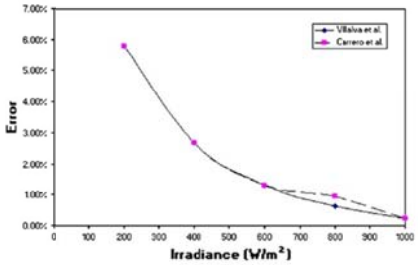

Fig. 8. Error plot for varying levels of irradiance for the blue cell modelled with values obtained from the methods of Villalva et al. and Carrero et al.

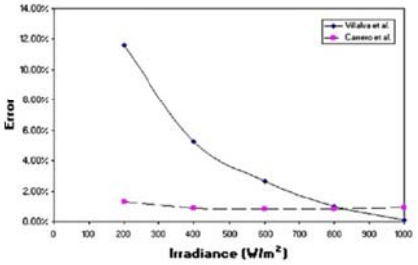

Fig. 9. Error plot for varying levels of irradiance for the grey cell modelled with values obtained from the methods of Villalva et al. and Carrero et al. The method of Carrero et al. in this case produced values similar to those of Charles et al. and therefore resulted in higher accuracy.

Table 7
The effect of changing the error threshold on the final values of R_s and R_{sh} and number of iterations necessary for the blue cell obtained using the proposed Newton–Raphson method.

Error threshold, ϵ	R_s	R_{sh}	Number of iterations
1.00E−07	0.0671	977.002	48
1.00E−06	0.0672	977.343	31
1.00E−05	0.0676	981.064	13
1.00E−04	0.0621	938.405	3
1.00E−03	0.0615	933.589	2

Table 8
The effect of changing the error threshold on the final values of R_s and R_{sh} and number of iterations necessary for the grey cell obtained using the proposed Newton Raphson method.

Error threshold, ϵ	R_s	R_{sh}	Number of iterations
1.00E−07	0.0784	26.089	19
1.00E−06	0.0784	26.089	15
1.00E−05	0.0784	26.092	10
1.00E−04	0.0785	26.125	5
1.00E−03	0.0790	26.252	2

output (Swaleh and Green, 1982). Results for the blue and grey cells are shown in Tables 5 and 6 respectively.

Interestingly values of maximum power output for all methods at conditions similar to STC ($G = 1000$ W/m^2) were within 1% of the values of Charles et al. despite the large variation in loss resistance values. However, as irradiance is varied the consequence of modelling with different values of loss resistances becomes clear. As values obtained from the proposed Newton–Raphson technique were within tolerance of the values obtained by Charles et al., all values for maximum power at all variations of irradiance were approximately equal to the values of Charles

Table 9
Summary of loss resistance values for three modules. Values obtained using the proposed Newton–Raphson method are compared with the values obtained by Carrero et al. and those published by Ikegami et al.

Module type	Method 1 proposed Newton–Raphson		Method 2 (Carrero et al., 2010)		Method 3 (Ikegami et al., 2001)	
	R_s (Ω)	R_{sh} (Ω)	R_s (Ω)	R_{sh} (Ω)	R_s (Ω)	R_{sh} (Ω)
Single-crystalline	0.219	129.24	0.250	125.40	0.346	193.70
Polycrystalline	0.214	184.66	0.239	179.80	0.360	972.60
Amorphous	0.328	164.99	0.550	176.88	0.420	138.40

Table 10
Values for maximum power output determined using the Lambert W-function model and values for loss resistances determined by each method.

Module type	Exp. results (Ikegami et al., 2001)	Method 1 proposed Newton–Raphson		Method 2 (Carrero et al., 2010)		Method 3 (Ikegami et al., 2001)	
	P_{max} (W)	P_{max} (W)	Error (%)	P_{max} (W)	Error (%)	P_{max} (W)	Error (%)
Single-crystalline	46.75	46.75	0.00	46.38	0.78	45.99	1.62
Poly-crystalline	42.62	42.62	0.00	42.38	0.56	42.33	0.68
Amorphous	23.10	23.10	0.00	22.68	1.85	22.63	2.07

et al. However, because of the large variation in loss resistances found by the alternative methods, errors in model output increased with a reduction in irradiance. Looking at Table 6, the method of Villalva et al. for example, underestimated the value of power by over 11% at $G = 200$ W/m^2. As a photovoltaic array will be subject to a large variation in irradiance over its useful life, we can infer that modelling with inaccurate values of loss resistances will similarly result in a variation in model accuracy. Figs. 8 and 9 plot the trend in error versus irradiance when modelling with loss resistances values obtained from the methods of Villalva et al. and Carrero et al. for the blue and grey cells respectively.

4.1.1. Selection of error threshold value, ε

For the proposed method, an error threshold value must be specified to end the Newton–Raphson iterative process. For the study carried out in the previous section, a significantly small value of $\varepsilon = 1 \times 10^{-7}$ was arbitrarily chosen. Varying this value will have the effect of changing final values for R_s and R_{sh}, and also the number of iterations needed for the analysis. Tables 7 and 8 summarise the effect of changing ε on these values for the blue and grey cells respectively. From these results, it is recommended that a value of at least $\varepsilon = 1 \times 10^{-6}$ be used to ensure a sufficient number of iterations are carried out to confirm values have converged to their final values.

4.2. Analysis of single, poly, and amorphous silicon modules

Having looked at two cells in the previous section, we now look to determine values of loss resistance for three modules of different type in order to assess the scalability of the proposed method. Characteristics of each of the modules studied is given in Table 2. Values of R_s and R_{sh} obtained for the three modules using the proposed method, the method of Carrero et al. and the values published by Ikegami et al. are presented in Table 9.

Examining Table 9 we can see that all values obtained from the three methods varied, however generally speaking the values obtained using the method of Carrero et al. were closer matched to those obtained by the proposed Newton–Raphson method. Similar to the procedure carried out in the previous section, the maximum power output of the model using Eqs. (2) and (20) were found based on the module characteristics given in Table 2 and the loss resistance values of Table 9. Diode saturation currents were again found using Eqs. (17) and (18). Model calculations for P_{max} were compared to the experimentally obtained values for I_{mp} and V_{mp} which was used to calculate P_{max} published by Ikegami et al. Results of this analysis is presented in Table 10.

Values obtained from the proposed method equalled the experimentally obtained values published by Ikegami et al. for all modules. When modelled with values obtained from methods 2 and 3, error in output varied from module to module. Poly-crystalline modules suffered the least loss in accuracy followed by the single-crystalline and amorphous modules. No such variation in accuracy was found with the proposed method.

5. Conclusion

This paper presents a new method to determine series and shunt resistance at maximum power point modelled with Lambert W-function equations using a multivariable version of the Newton–Raphson formula. Values obtained using this method were found to be in better agreement with the results of Charles et al. compared to the methods of Villalva et al. and Carrero et al. Although both

alternative methods proved to match experimental values of P_{max} at conditions similar to STC, our study of the blue and grey cells revealed that errors would arise when subject to varying levels in irradiance. Additionally, values for series and shunt resistance were determined with fast convergence stabilising towards their final values. The second part of our study which looked at three modules, demonstrated that the proposed Newton–Raphson method is more capable to determine loss resistance values for modules of different type. Limitations with this method however include the initial software coding of the partial derivative equations and the computational burden associated with the evaluation of the Lambert function. This method is therefore limited to use on a personal computer.

References

Barry, D.A., Culligan-Hensley, P.J., Barry, S.J., 1995. Real values of the W-Function. ACM transactions on Mathematical Software 21, 161–171.

Bashahu, M., Habyarimana, A., 1995. Review and test of methods for determination of the solar cell series resistance. Renewable Energy 6, 129–138.

Bouzidi, A., Chegaar, M., Bouhemadou, A., 2007. Solar cells parameters evaluation considering the series and shunt resistance. Solar Energy & Materials 91, 1647–1651.

Carrero, C., Amadow, J., Arnaltes, S., 2007. A single procedure for helping PV designers to select silicon PV modules and evaluate the loss resistances. Renewable Energy 32, 2579 2589.

Carrero, C., Rodriguez, J., Ramirez, D., Platero, C., 2010. Simple estimation of PV modules loss resistances for low error modelling. Renewable Energy, 1103 1108.

Chapra, S.C., Canale, R.P., 2002. Numerical methods for engineers: with software and programming applications. McGraw-Hill, New York.

Charles, J.P., Abdelkrim, M., Muoy, Y.H., Mialhe, P., 1981. A practical method of analysis of the current–voltage characteristics of solar cells. Solar Cells 4, 169–178.

Chegaar, M., Ouennoughi, Z., Guechi, F., 2004. Extracting dc parameters of solar cells under illumination. Vacuum 75, 367–372.

Chenni, R., Makhlouf, M., Kerbache, T., Bouzid, A., 2007. A detailed modeling method for photovoltaic cells. Energy 32, 1724 1730.

Corless, R.M., Gonnet, G.H., Hare, D.E.G., Jeffery, D.J., Knuth, D.E., 1996. On the Lambert W function. Advances in Computational Mathematics 5, 329 359.

de Blas, M.A., Torres, J.L., Garcia, A., 2002. Selecting a suitable model for characterizing photovoltaic devices. Renewable Energy 25, 371–380.

De Soto, W., Klein, S.A., Beckman, W.A., 2006. Improvement and validation of a model for photovoltaic array performance. Solar Energy 80, 78–88.

Faulkner, E.A., Buckingham, M.J., 1968. Electronics Letters 4, 359 360.

Ikegami, T., Maezono, T., Nakanishi, F., Yamagata, Y., Ebihara, K., 2001. Estimation of equivalent circuit parameters of PV module and its application to optimal operation of PV system. Solar Energy Materials & Solar Cells 67, 389 395.

Jain, A., Kapoor, A., 2004. Exact analytical solutions of the parameters of real solar cells using Lambert W-function. Solar Energy & Materials 81, 269 277.

Jia, Q., Anderson, W.A., Liu, E., Zhang, S., 1988. A novel approach for evaluating the series resistances of solar cells. Solar Cells 25, 311–318.

Macabebe, E.Q.B., Sheppard, C.J., Ernest van Dyk, E., 2011. Parameter extraction from I V characteristics of PV devices. Solar Energy 85, 12 18.

Petrone, G., Spagnuolo, G., Vitelli, M., 2007. Analytical model of mismatched photovoltaic fields by means of Lambert W-function. Solar Energy Materials and Solar Cells 91, 1652–1657.

Picault, D., Raison, B., Bacha, S., de la Casa, J., Aguilera, J., 2010. Forecasting photovoltaic array power production subject to mismatch losses. Solar Energy 84, 1301 1309.

Press, W.H., Teukolsky, S.A., Vetterling, W.T., Flannery, B.P., 2002. Numerical Recipes in C++: The Art of Scientific Computing. Cambridge University Press, Cambridge.

Psych, D., Mette, A., Glunz, S.W., 2007. A review and comparison of different methods to determine the series resistance of solar cells. Solar Energy & Materials 91, 1698 1706.

Swaleh, M.S., Green, M.A., 1982. Effect of shunt resistance and bypass diodes on the shadow tolerance of solar cell modules. Solar Cells 5, 183 198.

Villalva, M.G., Gazoli, J.R., Filho, E.R., 2009. Comprehensive approach to modeling and simulation of photovoltaic arrays. IEEE Transactions on Power Electronics 24, 1198 1208.

Xiao, W., Dunford, W.G., Capel, A., 2004. A novel modeling method for photovoltaic cells. In: 35th Annual IEEE Power Electronics Specialists Conference. Aachen, Germany, pp. 1950–1956.

Chapter 5: Numerical calculation of series and shunt resistance of a photovoltaic cell using the Lambert *W*-function: Experimental evaluation

5.0 Introduction

The method presented in Chapter 4 to determine the values of series and shunt resistances was validated by comparing the calculated values of two cells against data published in previous studies. These values are mandatory inputs for modelling the electrical behaviour of a solar cell. This chapter describes the experimental investigation performed to further validate the numerical method. Current-voltage curves for a single multi-crystalline cell were obtained while under varying levels of outdoor illumination in Hamilton, New Zealand. From these current-voltage curves, data typically provided by the manufacturer of a solar cell/module were extracted; (i) the short circuit current (I_{sc}), (ii) the open circuit voltage (V_{oc}), (iii) current at MPP (I_{mp}), and (iv) voltage at MPP (V_{mp}). This data was obtained by using a precise National Instrument source measuring unit which is (model NI-SMU-4130) able to measure the current response from the cell under varying loads.

Using the experimentally acquired data, the method described in Chapter 4 along with two other published methods was used to determine the values of series and shunt resistances. These values were then applied to the explicit current-voltage equation to obtain simulated current-voltage curves and compared to the original experimental curves.

A root mean square error analysis was conducted to compare the accuracy of each of the three methods investigated. The analysis revealed that the method described in Chapter 4 provided the closest match with the experimental P_{max} value and also that error between simulated and experimental data over the entire current-voltage curves was minimised over two existing methods.

Based on the results obtained from this research work, the method developed to calculate the values of series and shunt resistances could be confidently applied to further work investigating the effect of flow distribution and its effect on photovoltaic performance within a BIPVT collector.

5.1 Journal paper: Numerical calculation of series and shunt resistance of a photovoltaic cell using the Lambert *W*-function: Experimental evaluation

Available online at www.sciencedirect.com
SciVerse ScienceDirect
Solar Energy 87 (2013) 246–253
SOLAR ENERGY
www.elsevier.com/locate/solener

Numerical calculation of series and shunt resistance of a photovoltaic cell using the Lambert *W*-function: Experimental evaluation

F. Ghani [a,b,*], M. Duke [a], J. Carson [a]

[a] Department of Engineering, University of Waikato, Hamilton 3240, New Zealand
[b] School of Aerospace, Mechanical and Manufacturing Engineering, RMIT University, Melbourne 3002, Australia

Received 22 February 2012; received in revised form 5 November 2012; accepted 5 November 2012

Communicated by: Associate Editor Arturo Morales-Acevedo

Abstract

The values of series and shunt resistances play an important role in the modelling behaviour of a photovoltaic cell. The authors proposed in earlier work a new method to determine these values numerically at maximum power point using the Newton–Raphson method and equations based on the Lambert *W*-function. Here, an experimental investigation has been carried out to further validate this method and observe its behaviour over the entire current–voltage curve. Current–voltage curves from a single multi-crystalline cell were obtained under outdoor testing in Hamilton, New Zealand under three levels of illumination (800, 900, and 1000 W/m^2). In addition to the method of Ghani and Duke (2011), two other methods were also used to calculate series and shunt resistances based on the parameters extracted from the experimental data. A comparative study of each methods output current vector using a root mean square error analysis revealed that greatest accuracy was achieved with the proposed approach.

Keywords: Series resistance; Shunt resistance; Numerical calculation; Lambert *W*-function; Photovoltaic parameters; Solar modelling

1. Introduction

It is typical to utilise the five lumped parameter model in order to simulate the behaviour of a photovoltaic system. It has been shown (de Blas et al., 2002; De Soto et al., 2006) to yield results consistent with experimental values while avoiding excessive complexity. However, the accuracy of a model is not only dependent on the structure and functionality used to represent the physical system, but also by the parameters employed which govern the characteristics of the specific system under study (Carrero et al., 2010). Values such as the series (R_s) and shunt resistances (R_{sh}) for example are generally unpublished by solar cell and module manufacturers and must be obtained independently.

The series resistance is a lumped parameter value which represents the summation of several loss mechanisms in a solar cell. For example, losses due to resistance introduced in cell solder bonds, emitter and base regions, cell metallisation, and cell-interconnect busbars all contribute to the value of R_s (Green, 1998). Similarly the shunt resistance value represents any parallel high-conductivity paths across the solar cell *p–n* junction. An increase in series resistance results in a drop in voltage output while a decrease in shunt resistance will reduce current output (van Dyk and Meyer, 2004). Work by van Dyk and Meyer demonstrated that by increasing R_s from 0.36 to 1.80 ohms, both the maximum power (P_{max}) and fill factor (FF) were reduced by 25% making it clear that model yield is strongly influenced by loss resistance values.

By neglecting or failing to determine the correct resistance values of a cell or system under study, the modelling results obtained may be misleading. For instance, when modelling over a wide range of conditions as typically

* Corresponding author. Tel.: +64 61426599305.
E-mail address: faisal.ghani@rmit.edu.au (F. Ghani).

0038-092X/$ - see front matter © 2012 Elsevier Ltd. All rights reserved.
http://dx.doi.org/10.1016/j.solener.2012.11.002

experienced by a photovoltaic system, the predicted output of a maximum power point tracked system may be off from 5% to 8% by neglecting the series resistance term (Chenni et al., 2007). The influence of shunt resistance on modelling accuracy has a similar effect. An investigation on a 120 Wp mono-crystalline photovoltaic module which was carried out in another study (Celik and Acikgoz, 2007) in order to compare the modelling accuracy of the four and five parameter models against experimental data. Results from the four parameter model (which neglects the effects of shunt resistance) was found to produce greatest error with maximum error reported to be near 11% for the calculation of daily energy output. This is over double the maximum error obtained by the five parameter model (4.4%) which includes the effect of shunt resistance. The more complex two diode model is also encountered in the literature (Ishaque et al., 2011) which is composed of seven parameters. The additional complexity introduced by the two new modelling parameters however favours the implementation of the single diode five parameter model which is well known to yield accurate results (Villalva et al., 2009).

Given the importance of determining these parasitic values, a number of methods currently exist to determine the series and shunt resistances of a photovoltaic cell/module. Methods include analytical, experimental, and numerical types. One analytical five point model was proposed to determine the values of photogenerated current (I_{ph}), diode quality factor (n) saturation current (I_s), and R_s and R_{sh} (Chan and Phang, 1987; Chan et al., 1986). This method however requires the experimentally obtained values of open circuit voltage (V_{oc}), short circuit current (I_{sc}), voltage at maximum power point (V_{mp}), current at maximum power point, and slopes R_{so} and R_{sho} of the I–V curve at short circuit and open circuit respectively. An analytical approach was also adopted more recently in an another study (de Blas et al., 2002). The analytical approach has the advantage that it is fast to calculate by avoiding the iterative process required by a numerical approach. However, the approach used by these studies required the values of R_{so} and R_{sho} which must be found experimentally by examining the slopes at open circuit and short circuit points respectively as these values are generally unpublished by the manufacturer. Other methods such as particle swarm optimisation (PSO) which employs an algorithm to extract parameters including R_s and R_{sh} similarly requires experimentally acquired I–V curves (Macabebe et al., 2011). Two methods (Carrero et al., 2010; Villalva et al., 2009) currently exist which look to obtain the values of these resistance values numerically at maximum power point. As photovoltaic systems are generally coupled with maximum power point trackers (MPPTs), this approach seems justified and has the advantage that it can be carried out using only data provided by the manufacturer.

A method proposed previously by the authors (Ghani and Duke, 2011) numerically determines the values of series and shunt resistance at maximum power point (*MPP*) based primarily on values obtained by the data sheets supplied by the manufacturer (i.e. I_{sc}, V_{oc}, I_{mp}, and V_{mp}). This way, experimentation is not required unlike the methods discussed previously. This numerical method solves a system of non-linear equations derived by examining the I–V and P–V characteristic equations using a multi-variable version of the Newton–Raphson algorithm. Equations modelled with the Lambert W-function were used to model the current equation explicitly in terms of voltage and permit calculation of the necessary partial derivatives for the Jacobian matrix. Although mathematically rigorous, the method published by the authors was shown to determine the values of R_s and R_{sh} with quadratic convergence. This work however was only supported by comparing to previously published data and at maximum power point only. Here we present experimental work carried out to validate this method in comparison to the methods of Villalva et al. (2009) and Carrero et al. (2010) for the experimentally acquired I–V curve of a single multi-crystalline cell exposed to varying levels outdoor illumination. The aim is to compare the modelling accuracy of a photovoltaic cell for each of the three approaches.

2. Research methods

2.1. Overview

The current–voltage curves of a single multi-crystalline silicon (mc-Si) cell with the basic electrical characteristics provided in Table 1 was obtained experimentally under various levels of outdoor illumination in Hamilton, New Zealand from which the values of I_{sc}, V_{oc}, I_{mp}, and V_{mp} were extracted.

Extracting the values for I_{mp}, V_{mp}, and $P_{\max}$ from these experimental curves, the values for R_s and R_{sh} were calculated using the method of Ghani and Duke (2011) for each level of illumination. Additionally two other methods (Carrero et al., 2010; Villalva et al., 2009) were used to determine the resistance values for comparative purpose. Throughout this study the diode constant (n) was assumed to be constant with the value of one.

These values were then used in Eq. (1) (Jain and Kapoor, 2004) to obtain the current vector based on the equivalent voltage vector used to sweep the solar cell and obtain the experimental I–V curve. Curves obtained from the mathematical model were then compared to the original experimental I–V curve and statistically compared using a root mean square error analysis. Details for each step are provided in the proceeding sections.

$$i = -\frac{V}{R_s + R_{sh}} - \frac{\text{Lambert } W\left(\frac{R_s I_0 R_{sh}}{nV_{th}(R_s+R_{sh})} e^{\left(\frac{R_{sh}(R_s I_{ph} + R_s I_0 + V)}{nV_{th}(R_s+R_{sh})}\right)}\right) nV_{th}}{R_s} + \frac{R_{sh}(I_0 + I_{ph})}{R_s + R_{sh}} \quad (1)$$

Table 1
Current–voltage properties of the mc-Si cell used for this study at standard test conditions (STC).

J_{sc} (mA/cm^2)	32.36
V_{oc} (V)	0.596
J_{mp} (mA/cm^2)	28.04
V_{mp} (V)	0.424

2.2. Experimental acquisition of I–V curves

The wiring diagram of the equipment used to collect the current–voltage data of the mc-Si cell is shown in Fig. 1. The current voltage curve of the photovoltaic cell (for properties see Table 1) manufactured by Silicon Solar was obtained using a high speed programmable source measuring unit (SMU) manufactured by National Instruments (model NI-PXI-4130). The SMU was connected to the cell using a four wire or remote sensing scheme to eliminate measurement error introduced by the lead resistance as used in other work (Chan et al., 1986). With the four wire approach, a voltage is sourced across the cell using one pair of leads (Force HI and Force LO, Fig. 1), and the voltage drop across the cell using another pair of leads (Sense HI and Sense LO, Fig. 1). This way any lead resistance could be compensated during measurement. The current–voltage characterisation was performed on a cell illuminated outdoors in Hamilton, New Zealand (37°47′S, 175°19′E). We chose to perform an outdoor forward bias test over a dark reverse bias test as it has been acknowledged to yield more accurate values given the realistic operating conditions (Bashahu and Habyarimana, 1995). Radiation was measured using a Middleton Solar EQ-08 pyranometer and logged during measurement. Current–voltage measurements were taken at 800, 900 and 1000 W/m^2 of irradiance.

In total, the DC voltage sweep consisted of 75 points from 0 V to V_{oc} (approximately 0.6 V at STC – see Table 1). For the current range measured, the NI-PXI 130 SMU is stated by the manufacturer to have a current measurement resolution of 100 μA. The cell under test was mounted with good thermal contact using a thin layer (less than 1 mm thick) of thermal adhesive to a high efficiency aluminium heat sink which was mechanically coupled to two 12VDC fans. Convection cooling of the heat sink fins was implemented in order to reduce the rise in operating temperature of the cell during the measurement period which was <5 s. A k-type thermocouple was thermally adhered to the rear side of the cell using a curing heat transfer compound to provide an approximate value of the cell operating temperature (T_{cell}). It was found that temperature rise of the cell was <1 °C for the I V measurement period at 1000 W/m^2. The entire measurement process was controlled using National Instruments LabView software and the National Instruments PXI-1033 hardware platform. This included all hardware control, parameter extraction, and data logging.

2.3. Numerical calculation of R_s and R_{sh} using the Lambert W-function

Theory behind the method of numerically calculating the series and shunt resistance using the Lambert W-function is provided elsewhere (Ghani and Duke, 2011); however, the essential equations are reproduced here for completeness. A multi-variable version of the Newton–Raphson method (Chapra and Canale, 2002) was used to solve a system of non-linear equations for R_s and R_{sh} at maximum power point. Values for R_s and R_{sh} were calculated iteratively using Eqs. (2) and (3) starting with initial values $R_{s,i}$ and $R_{sh,i}$.

$$R_{s_{i+1}} = R_{s,i} - \frac{z_i \frac{\partial w_i}{\partial R_{sh}} - w_i \frac{\partial z_i}{\partial R_{sh}}}{\frac{\partial z_i}{\partial R_s}\frac{\partial w_i}{\partial R_{sh}} - \frac{\partial z_i}{\partial R_{sh}}\frac{\partial w_i}{\partial R_s}} \tag{2}$$

$$R_{sh,i+1} = R_{sh,i} - \frac{w_i \frac{\partial z_i}{\partial R_s} - z_i \frac{\partial w_i}{\partial R_s}}{\frac{\partial z_i}{\partial R_s}\frac{\partial w_i}{\partial R_{sh}} - \frac{\partial z_i}{\partial R_{sh}}\frac{\partial w_i}{\partial R_s}} \tag{3}$$

where expression z was derived by substituting the values of I_{mp} and V_{mp} for I and V respectively into Eq. (1) yielding Eq. (4).

$$z \equiv \frac{R_{sh}(I_0 + I_{ph})}{(R_s + R_{sh})} - \frac{V_{mp}}{(R_s + R_{sh})} - \frac{nV_{th}}{R_s}\,\text{Lambert}\,W(\theta_1) - I_{MP} = 0 \tag{4}$$

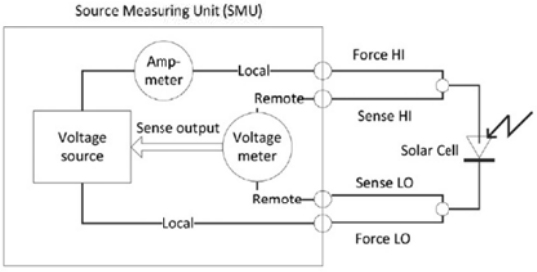

Fig. 1. Wire connection diagram for I V measurement of cell with SMU.

where θ_1 is given by,

$$\theta_1 = \frac{R_s I_0 R_{sh}}{nV_{th}(R_s + R_{sh})} e^{\frac{R_{sh}(R_s I_{ph} - R_s I_0 + V_{mp})}{nV_{th}(R_s + R_{sh})}} \quad (5)$$

Similarly expression w was obtained by examining the P–V curve and knowledge that a global maximum exists at maximum power point. Therefore,

$$\frac{\partial P}{\partial V} = 0|_{V=V_{mp}} \quad (6)$$

Equations for the partial derivative of power with respect to i and V have been published previously (Jain and Kapoor, 2004). Similar to Eq. (4) we use the partial derivative of P with respect to current to define expression w at MPP by substituting values for i and V with I_{mp} and V_{mp} respectively.

$$w \equiv R_{sh}I_{ph} + R_{sh}I_0 - 2I_{mp}R_s - 2I_{mp}R_{sh} - nV_{th}\text{Lambert } W(\theta_2) - I_{mp}R_{sh}\left\{\frac{\text{Lambert } W(\theta_2)}{[1 + \text{Lambert } W(\theta_2)]}\right\} = 0 \quad (7)$$

where θ_2 is given by,

$$\theta_2 = \frac{I_0 R_{sh}}{nV_{th}} e^{\frac{R_{sh}(-I_{mp} - I_{ph} - I_0)}{nV_{th}}} \quad (8)$$

where the partial derivatives needed for Eqs. (2) and (3) are provided in Appendix A.

Ghani and Duke (2011) demonstrated that the proposed numerical method to determine the values of R_s and R_{sh} was fast and also accurate in comparison to two recently published methods (Carrero et al., 2010; Villalva et al., 2009) at maximum power point. The current vector was then generated using parameters calculated from each of the three methods using Eq. (1) and compared against the experimental data.

3. Results and discussion

A single 78 × 24 mm multi-crystalline cell (see Table 1) was tested outdoors at 800, 900, and 1000 W/m^2 of illumination. From the data collected, values for I_{sc}, V_{oc}, I_{mp}, and V_{mp} were obtained and used to approximate the lumped parameter values of R_s and R_{sh} using three methods:

(a) By the method of Ghani and Duke (2011).
(b) By the method of Carrero et al. (2010).
(c) By the method of Villalva et al. (2009).

The values obtained for R_s and R_{sh} by each method at each level of illumination is presented in Table 2.

Examining Table 1, we make the following general observations;

1. The values for R_s are similar between the author's method and the method of Carrero et al. (2010). However, the values for R_{sh} are approximately 15–20% higher.
2. Comparing the author's method to the method of Villalva et al. (2009), both R_s and R_{sh} values differ significantly, with values obtained with the latter method always less for both resistances.
3. The values obtained by Ghani and Duke (2011) for R_s decrease with irradiance supporting the results of another study (Benda and Machacek, 2010).

It was assumed for our modelling study that the photo-generated current (I_{ph}) was equal to the short circuit current (I_{sc}) (Chenni et al., 2007). The diode saturation current (I_0) was determined by Eqs. (9) and (10) (De Soto et al., 2006).

$$I_0 = I_{0,n}\left(\frac{T_n}{T}\right)^3 e^{\left[\frac{qE_g}{Ak_B}\left(\frac{1}{T_n} - \frac{1}{T}\right)\right]} \quad (9)$$

where,

$$I_{0,n} = \frac{I_{sc,n}}{e^{\left(\frac{V_{oc,n}}{aV_{th,n}}\right)} - 1} \quad (10)$$

T and T_n represent the actual and nominal cell temperatures respectively in Kelvin, E_g is the band gap energy of the semi-conductor, k_B is the Boltzmann constant (1.38×10^{-23} J/K), and q is the value of electron charge (1.6×10^{-19} C).

Substituting the values listed in Table 2 into Eq. (1), the current vector for each method and illumination was calculated. Tables 3–5 summarises the six parameters (I_{sc}, V_{oc}, I_{mp}, V_{mp}, P_{max}, and FF) extracted from the current–voltage array calculated by each method for each illumination level along with the corresponding experimental values.

Comparing the data presented in Tables 3–5 we can see that the proposed method for calculating R_s and R_{sh}, results in the most accurate model output for P_{max} with negligible variation from the experimental value. The method of Carrero et al. (2010) however marginally yields the closest correct value of fill factor (FF).

Table 2
Values of R_s and R_{sh} obtained from each of the three methods investigated.

	800 W/m^2			900 W/m^2			1000 W/m^2		
	Ghani and Duke (2011)	Carrero et al. (2010)	Villalva et al. (2009)	Ghani and Duke (2011)	Carrero et al. (2010)	Villalva et al. (2009)	Ghani and Duke (2011)	Carrero et al. (2010)	Villalva et al. (2009)
R_s (Ω)	0.2171	0.2170	0.1727	0.2160	0.2178	0.1878	0.2023	0.2024	0.1742
R_{sh} (Ω)	25.338	22.056	15.734	18.190	15.404	13.913	19.295	16.276	13.417

Table 3
Experimental and model parameters extracted from the I–V curves at 800 W/m^2.

	I_{sc} (A)	V_{oc} (V)	I_{mp} (A)	V_{mp} (V)	P_{max} (W)	FF
Experimental data	0.4574	0.5792	0.4069	0.4212	0.1714	0.6468
Ghani and Duke (2011)	0.4535	0.5758	0.4050	0.4232	0.1714	0.6562
Carrero et al. (2010) method	0.4529	0.5758	0.4027	0.4232	0.1704	0.6533
Villalva et al. (2009) method	0.4524	0.5758	0.3996	0.4362	0.1743	0.6691

Table 4
Experimental and model parameters extracted from the I–V curve at 900 W/m^2.

	I_{sc} (A)	V_{oc} (V)	I_{mp} (A)	V_{mp} (V)	P_{max} (W)	FF
Experimental data	0.5122	0.5879	0.4495	0.4213	0.1894	0.6288
Ghani and Duke (2011)	0.5062	0.5846	0.4475	0.4232	0.1893	0.6399
Carrero et al. (2010) method	0.5051	0.5846	0.4426	0.4232	0.1873	0.6344
Villalva et al. (2009) method	0.5054	0.5846	0.4447	0.4319	0.1921	0.6501

Table 5
Experimental and model parameters extracted from the I–V curve at 1000 W/m^2.

	I_{sc} (A)	V_{oc} (V)	I_{mp} (A)	V_{mp} (V)	P_{max} (W)	FF
Experimental data	0.5768	0.5965	0.5100	0.4244	0.2164	0.6290
Ghani and Duke (2011)	0.5708	0.5933	0.5115	0.4232	0.2164	0.6391
Carrero et al. (2010) method	0.5697	0.5933	0.5076	0.4232	0.2148	0.6354
Villalva et al. (2009) method	0.5694	0.5933	0.5035	0.4362	0.2197	0.6502

Table 6
Mean square and root mean square error analysis for each method and illumination.

	800 W/m^2			900 W/m^2			1000 W/m^2		
	Ghani and Duke (2011)	Carrero et al. (2010)	Villalva et al. (2009)	Ghani and Duke (2011)	Carrero et al. (2010)	Villalva et al. (2009)	Ghani and Duke (2011)	Carrero et al. (2010)	Villalva et al. (2009)
MSE	0.0001	0.0001	0.0003	0.0001	0.0002	0.0001	0.0001	0.0002	0.0002
RMSE	0.0105	0.0115	0.0161	0.0113	0.0135	0.0122	0.0101	0.0124	0.0141

Table 7
Relative efficiency values determined using Eq. (13) for each level of illumination.

	800 W/m^2		900 W/m^2		1000 W/m^2	
	Carrero et al. (2010)	Villalva et al. (2009)	Carrero et al. (2010)	Villalva et al. (2009)	Carrero et al. (2010)	Villalva et al. (2009)
Relative efficiency	0.8276	0.4223	0.7038	0.8574	0.6632	0.5177

To compare the accuracy of each method over the entire I V curve, the mean square error (MSE) and root mean square error (RMSE) values were calculated for the current vectors as calculated by Eqs. (11) and (12) respectively. Results are listed in Table 6.

$$MSE(i_{\exp}, i_{\text{model}}) = \frac{1}{N}\sum_{i=1}^{N}(i_{\exp} - i_{\text{model}})^2 \tag{11}$$

where N is the number of samples, $i_{\exp}$ and i_{model} are the experimental and model values for current respectively. The root mean square error is found by taking the square root of the MSE.

$$RMSE = \sqrt{MSE} \tag{12}$$

From Table 6 the root mean square error (RMSE) value of the model current vector is minimised by obtaining values of R_s and R_{sh} using the proposed method in all cases. The relative efficiency calculation defined by Eq. (13) (Montogomery et al., 2011) further demonstrates the improved model efficiency of the proposed method to the alternative methods studied. Relative efficiency values are given in Table 7.

$$\text{Relative efficiency} = \frac{MSE(\varphi_{\text{proposed}})}{MSE(\varphi_{\text{alternative}})} \tag{13}$$

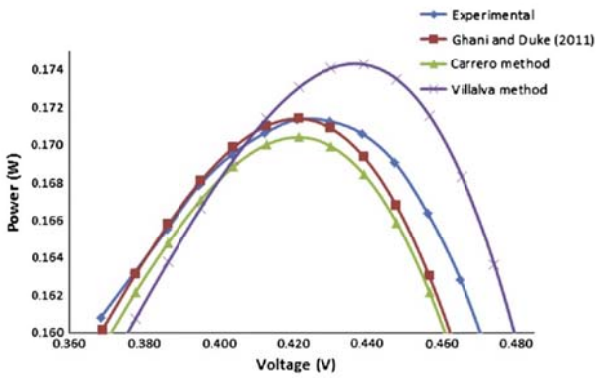

Fig. 2. *P–V* curves at *MPP* for experimental and model data at 800 W/m2.

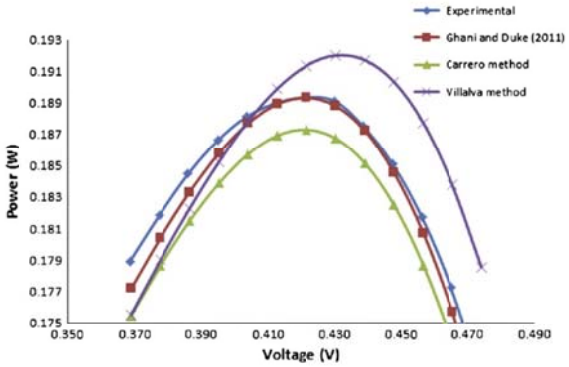

Fig. 3. *P–V* curves at *MPP* for experimental and model data at 900 W/m2.

Relative efficiency values in all cases were found to be less than unity indicating superiority of the proposed method with respect to a mean square error analysis.

The influence of varying the values of R_s and R_{sh} on the power-voltage curves is demonstrated by Figs. 2–4 which examines the *P V* curve near *MPP* at 800, 900, and 1000 W/m^2 of illumination respectively. From each figure we make the general comment that the model output when characterised with values obtained from the proposed method is most accurate at *MPP*. The method of Villalva et al. (2009) over estimates this value, while the method of Carrero et al. (2010) slightly underestimates it.

Inspecting Figs. 2–4 we can see that the model output matches the experimental data at *MPP* only. Away from this point, the model output deviates from the experimental data. The authors found that by adjusting the diode quality factor *n*, this disparity is minimised. Consequently research in this area is currently being undertaken by the authors.

4. Conclusions

The proposed method to calculate the lumped parameter values of series and shunt resistance using the Newton–Raphson method and equations based on the Lambert *W*-function has been experimentally shown to accurately describe the behaviour of a multi-crystalline solar cell. Based on a RMSE analysis of the entire current vector, this method has demonstrated improved accuracy over two existing methods at various levels of illumination. The proposed method like the alternatives studied in this paper requires only values typically provided by the manufacturer and the diode quality factor. The obvious

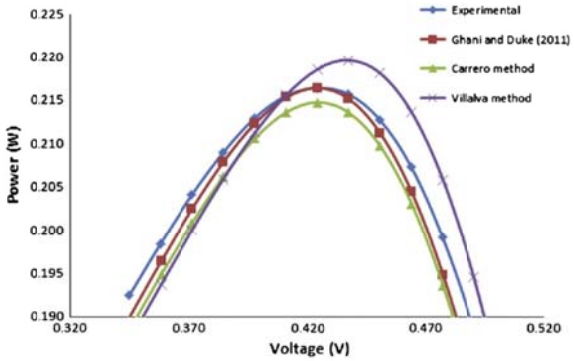

Fig. 4. *P V* curves at *MPP* for experimental and model data at 1000 W/m2.

limitation however is the initial programming of the necessary equations in a Matlab or similar environment.

Appendix A. Partial differential equations

Partial differential equations required for the method of Ghani and Duke (2011).

$$\frac{\partial z}{\partial R_s} = \frac{V_{mp}}{(R_s + R_{sh})^2} - \frac{(R_{sh}I_0 + R_{sh}I_{ph})}{(R_s + R_{sh})^2} - \frac{nV_{th}}{R_s^2}\text{Lambert } W(\theta_1) - \frac{nV_{th}}{R_s}\frac{\text{Lambert } W(\theta_1)}{[1 + \text{Lambert } W(\theta_1)]\theta_1}\frac{\partial \theta_1}{\partial R_s} \quad \text{(A.1)}$$

$$\frac{\partial \theta_1}{\partial R_s} = \frac{I_0 R_{sh}(nV_{th}R_s + nV_{th}R_{sh}) - nV_{th}(R_s I_0 R_{sh})}{(nV_{th}R_s + nV_{th}R_{sh})^2} e^{\frac{R_{sh}(R_s I_{ph} + R_s I_0 + V_{mp})}{nV_{th}(R_s + R_{sh})}} + \frac{R_s I_0 R_{sh}}{nV_{th}(R_s + R_{sh})} \times \frac{(R_{sh}I_{ph} + R_{sh}I_0)(nV_{th}R_s + nV_{th}R_{sh}) - nV_{th}(R_{sh}R_s I_{ph} + R_{sh}R_s I_0 + R_{sh}V_{mp})}{[nV_{th}(R_s + R_{sh})]^2} e^{\frac{R_{sh}(R_s I_{ph} + R_s I_0 + V_{mp})}{nV_{th}(R_s + R_{sh})}} \quad \text{(A.2)}$$

$$\frac{\partial z}{\partial R_{sh}} = \frac{V_{mp}}{(R_s + R_{sh})^2} - \frac{(I_0 + I_{ph})(R_s + R_{sh}) - (R_{sh}I_0 + R_{sh}I_{ph})}{(R_s + R_{sh})^2} - \frac{nV_{th}}{R_s}\frac{\text{Lambert } W(\theta_1)}{[1 + \text{Lambert } W(\theta_1)]\theta_1}\frac{\partial \theta_1}{\partial R_{sh}} \quad \text{(A.3)}$$

$$\frac{\partial \theta_1}{\partial R_{sh}} = \frac{R_s I_0(nV_{th}R_s + nV_{th}R_{sh}) - nV_{th}(R_s I_0 R_{sh})}{[nV_{th}(R_s - R_{sh})]^2} e^{\frac{R_{sh}(R_s I_{ph} + R_s I_0 + V_{mp})}{nV_{th}(R_s + R_{sh})}} + \frac{R_s I_0 R_{sh}}{nV_{th}(R_s + R_{sh})} \times \frac{(R_s I_{ph} + R_s I_0 + V_{mp})(nV_{th}R_s + nV_{th}R_{sh}) - nV_{th}(R_{sh}R_s I_{ph} + R_{sh}R_s I_0 + R_{sh}V_{mp})}{(nV_{th}R_s - nV_{th}R_{sh})^2} e^{\frac{R_{sh}(R_s I_{ph} + R_s I_0 + V_{mp})}{nV_{th}(R_s - R^{sh})}} \quad \text{(A.4)}$$

$$\frac{\partial w}{\partial R_s} = -2I_{mp} \quad \text{(A.5)}$$

$$\frac{\partial w}{\partial R_{sh}} = I_{ph} + I_0 - 2I_{mp} - V_{th}\left\{\frac{\text{Lambert } W(\theta_2)}{[1 + \text{Lambert } W(\theta_2)]\theta_2}\frac{\partial \theta_2}{\partial R_{sh}}\right\} + I_{mp}\left\{\frac{\text{Lambert } W(\theta_2)}{[1 + \text{Lambert } W(\theta_2)]\theta_2}\right\} + I_{mp}R_{sh}\left\{\frac{\text{Lambert } W(\theta_2)}{[1 + \text{Lambert } W(\theta_2)]^3\theta_2}\frac{\partial \theta_2}{\partial R_{sh}}\right\} \quad \text{(A.6)}$$

$$\frac{\partial \theta_2}{\partial R_{sh}} = \frac{I_0}{nV_{th}} e^{\frac{R_{sh}(-I_{mp} + I_{ph} + I_0)}{nV_{th}}}\left\{1 + \frac{R_{sh}(-I_{mp} + I_{ph} + I_0)}{nV_{th}}\right\} \quad \text{(A.7)}$$

References

Bashahu, M., Habyarimana, A., 1995. Review and test of methods for determination of the solar cell series resistance. Renewable Energy 6, 129–138.

Benda V., Machacek Z., 2010. A note on parameters of photovoltaic cells in dependence on irradiance and temperature. In: Presented at the 7th Mediterranean Conference on Power Generation, Distribution and Energy Conversion, Agia Napa, Cyprus.

Carrero, C., Rodriguez, J., Ramirez, D., Platero, C., 2010. Simple estimation of PV modules loss resistances for low error modelling. Renewable Energy, 1103–1108.

Celik, A.N., Acikgoz, N., 2007. Modelling and experimental verification of the operating current of mono-crystalline photovoltaic modules using four- and five-parameter models. Applied Energy 84, 1–15.

Chan, D.S., Phang, J.C.H., 1987. Analytical methods for the extraction of solar-cell single- and double-diode model parameters from *I–V* characteristics. IEEE Transactions on Electron devices 34, 286–293.

Chan, D.S., Phillips, J.R., Phang, J.C.H., 1986. A comparative study of extraction methods for solar cell model parameters. Solid-State Electronics 29, 329–337.

Chapra, S.C., Canale, R.P., 2002. Numerical methods for engineers: with software and programming applications, fourth ed. McGraw-Hill, New York.

Chenni, R., Makhlouf, M., Kerbache, T., Bouzid, A., 2007. A detailed modeling method for photovoltaic cells. Energy 32, 1724–1730.

de Blas, M.A., Torres, J.L., Garcia, A., 2002. Selecting a suitable model for characterizing photovoltaic devices. Renewable Energy 25, 371–380.

De Soto, W., Klein, S.A., Beckman, W.A., 2006. Improvement and validation of a model for photovoltaic array performance. Solar Energy 80, 78–88.

Ghani, F., Duke, M., 2011. Numerical determination of parasitic resistances of a solar cell using the Lambert *W*-function. Solar Energy 85, 2386–2394.

Green, M.A., 1998. Solar Cells Operating Principles, Technology and System Applications. University of New South Wales.

Ishaque, K., Salam, Z., Taheri, H., Syafaruddin, 2011. Simple, fast and accurate two-diode model for photovoltaic modules. Solar Energy Materials and Solar Cells 95, 1613–1626.

Jain, A., Kapoor, A., 2004. Exact analytical solutions of the parameters of real solar cells using Lambert W-function. Solar Energy and Materials 81, 269–277.

Macabebe, E.Q.B., Sheppard, C.J., Ernest van Dyk, E., 2011. Parameter extraction from *I–V* characteristics of PV devices. Solar Energy 85, 12–18.

Montogomery, D.C., Runger, G.C., Hubele, N.F., 2011. Engineering Statistics, 5th ed. John Wiley & Sons, Chichester.

van Dyk, E.E., Meyer, E.L., 2004. Analysis of the effect of parasitic resistances on the performance of photovoltaic modules. Renewable Energy 29, 333–344.

Villalva, M.G., Gazoli, J.R., Filho, E.R., 2009. Comprehensive approach to modeling and simulation of photovoltaic arrays. IEEE Transactions on Power Electronics 24, 1198–1208.

Chapter 6: Numerical calculation of series and shunt resistances and diode quality factor of a photovoltaic cell using the Lambert *W*-function

6.0 Introduction

Previous research work has been focused on the development of a novel method to determine the series and shunt resistance values of a crystalline silicon cell. These two parameter values are necessary to accurately model the electrical behaviour of a photovoltaic cell and are therefore needed for the final goal of creating a model of a building integrated solar collector which examines the effect of flow mal-distribution on photovoltaic performance. The novel method outlined in Chapter 4 however was initially validated by calculating resistance values for two cells (blue and grey types) and comparing calculated values with published values. It was shown that the method produced values matching those published, additionally it was demonstrated that it offered greater accuracy over two other recently published methods. Chapter 5 discussed the work carried out to further validate this method by experimental means. Complete current-voltage data for a crystalline silicon cell (the predominant cell type today) were measured while exposed to varying levels of irradiance in Hamilton, New Zealand. Extracting the data that is typically provided by the manufacturer from this data (i.e. I_{mp}, V_{mp}, I_{sc}, and V_{oc}), the values for R_s and R_{sh} were calculated and used to generate current-voltage data using the single diode, five parameter equation. The simulated current-voltage data was then compared to the original experimental data.

Examination of the combined experimental and simulated data revealed that a growing disparity between the method described in Chapter 4 and experimental data would occur moving away from the maximum power point. By means of a sensitivity analysis, it was found that by adjusting the diode constant value n, this disparity could be reduced thereby improving modelling accuracy. A modification to the original algorithm presented in

Chapter 5 was therefore made so that the diode constant could also be evaluated from data provided by the manufacturer.

Initially the algorithm assumes the diode constant is equal to one. Based on this value, the values for R_s and R_{sh} are then calculated using the method described in Chapter 4. The current-voltage curve is then generated for a voltage vector between 0 V and V_{oc} from which the fill factor (FF) is calculated. The modelled FF is compared to the fill factor provided by the manufacturer. If an error is present, the diode constant value is incremented and the process is repeated until the error falls below a specified threshold.

To validate this new method, the experimental procedure outlined in Chapter 5 was again applied to compare the simulated data against experimental data. For comparative purpose, the proposed algorithm was again compared against the method described in Chapter 4 and another published method. It was found that the modified algorithm was able to substantially improve modelling accuracy calculated based on a root mean square error analysis.

This method permits the calculation of three parameters: R_s, R_{sh}, and n, all of which are needed for the final mathematical model used to calculate the total yield of a PV system operating under heterogeneous operating temperature which shall be discussed. The improved performance obtained in the calculation of the third parameter (n) will consequently improve the performance of the final model which is to be developed in this study.

6.1 Journal Paper: Numerical calculation of series and shunt resistances and diode quality factor of a photovoltaic cell using the Lambert *W*-function

Available online at www.sciencedirect.com
SciVerse ScienceDirect
Solar Energy 91 (2013) 422–431
SOLAR ENERGY
www.elsevier.com/locate/solener

Numerical calculation of series and shunt resistances and diode quality factor of a photovoltaic cell using the Lambert *W*-function

F. Ghani *, M. Duke, J. Carson

Department of Engineering, University of Waikato, Hamilton 3240, New Zealand

Received 7 March 2012; received in revised form 5 August 2012; accepted 8 September 2012
Available online 23 October 2012

Communicated by: Associate Editor Arturo Morales-Acevedo

Abstract

A number of methods currently exist to determine the modeling parameters of a solar cell. The authors presented in earlier a work a method to numerically determine the values of series and shunt resistance using the Lambert *W*-function at maximum power point primarily using data provided by the manufacturer. This method however assumes the diode constant value is known. An experimental investigation revealed that by setting the diode constant to unity as suggested in other work, a growing disparity between model output and experimental values would arise away from the maximum power point. To address this issue, a modification is proposed to the method of Ghani and Duke (2011) which permits the calculation of the diode constant and the corresponding values of series and shunt resistances. The method was experimentally validated by collecting the current–voltage characteristics of a multi-crystalline cell exposed to 800, 900, and 1000 W/m^2 of outdoor illumination in Hamilton, New Zealand. A comparative analysis of the model generated data using parameters found by the proposed method and two additional methods against experimental data revealed a significant reduction in the root mean square error over the entire current vector was obtained using the proposed method. The method is simple to apply and can be carried out using data provided the manufacturer.

Keywords: Series resistance; Shunt resistance; Diode constant; Lambert function; Cell modeling; Solar parameters

1. Introduction

The single diode, five parameter model represented by Eq. (1) is typically utilised to mathematically model the behaviour of a photovoltaic cell or device (Villalva et al., 2009).

$$I = I_{ph} - \frac{V + IR_s}{R_{sh}} - I_0\left[e^{\left(\frac{V+IR_s}{nV_{th}}\right)} - 1\right] \quad (1)$$

where I is the current, V is the voltage, R_s and R_{sh} are the series and shunt resistances respectively, I_{ph} is the photo-generated current, n is the diode quality factor, and V_{th} is the thermal voltage calculated by,

$$V_{th} = \frac{k_B T}{q} \quad (2)$$

And the diode saturation current (I_0) was determined by Eqs. (3) and (4) (De Soto et al., 2006).

$$I_0 = I_{0,n}\left(\frac{T_n}{T}\right)^3 e^{\left[\frac{qE_g}{nk_B}\left(\frac{1}{T_n}-\frac{1}{T}\right)\right]} \quad (3)$$

where,

$$I_{0,n} = \frac{I_{sc,n}}{e^{\left(\frac{V_{oc,n}}{nV_{th,n}}\right)} - 1} \quad (4)$$

T and T_n represent the actual and nominal cell temperatures respectively in Kelvin, E_g is the band gap energy of the semi-conductor (eV), k_B is the Boltzmann constant (1.38065×10^{-23} J/K), and q is the value of electron charge (1.6022×10^{-19} C).

* Corresponding author. Tel.: +64 7 838 4522.
E-mail address: fag2@waikato.ac.nz (F. Ghani).

0038-092X/$ - see front matter © 2012 Elsevier Ltd. All rights reserved.
http://dx.doi.org/10.1016/j.solener.2012.09.005

The five parameter model has been shown to offer improved accuracy over the more basic four parameter model which neglects the effects of shunt resistance (Celik and Acikgoz, 2007) while avoiding the additional complexity of the double diode model (Chan and Phang, 1987).

The implicit nature of Eq. (1) and its computationally burdensome evaluation has however resulted in the growing use of an alternative expression based on the Lambert W-function (Jain and Kapoor, 2004; Jain et al., 2006; Petrone et al., 2007; Picault et al., 2010). By using the Lambert W-function the current can be expressed as an explicit function of voltage as shown by Eq. (5). The result is a more convenient and computationally efficient calculation of current.

$$i = -\frac{V}{R_s + R_{sh}} - \frac{LambertW\left(\frac{R_s I_0 R_{sh}}{nV_{th}(R_s+R_{sh})} e^{\left(\frac{R_{sh}(R_s I_{ph} + R_s i_0 + V)}{nV_{th}(R_s+R_{sh})}\right)}\right) nV_{th}}{R_s} + \frac{R_{sh}(I_0 + I_{ph})}{R_s + R_{sh}} \quad (5)$$

To obtain the current–voltage characteristic of a cell using Eq. (5) however, a number of parameters such as the series (R_s) and shunt (R_{sh}) resistances and the diode quality factor (n) must first be found for the particular device under study. The series resistance is a lumped parameter value which represents the summation of several loss mechanisms in a solar cell. For example, losses due to resistance introduced in cell solder bonds, emitter and base regions, cell metallisation, and cell-interconnect busbars all contribute to the value of R_s (Green, 1998). Similarly the shunt resistance value represents any parallel high-conductivity paths across the solar cell p–n junction. An increase in series resistance results in a drop in voltage output while a decrease in shunt resistance will reduce current output (van Dyk and Meyer, 2004). Work by van Dyk and Meyer demonstrated that by increasing R_s from 0.36 to 1.80 Ω, both the maximum power (P_{max}) and fill factor (FF) were reduced by 25% making it clear that the behaviour of a photovoltaic device is strongly influenced by loss resistance values.

In earlier work (Ghani and Duke, 2011), the authors provided a method to numerically calculate the values of series and shunt resistances using the Newton Raphson algorithm based on using the Lambert W-function. The purpose of this method was to calculate the values of R_s and R_{sh} so that the maximum power output (P_{max}) of the model would equal the value provided by the manufacturer. Equations based on the Lambert W-function were utilised so that the current could be expressed explicitly in terms of voltage and also for its relatively straightforward differentiation. The primary advantages of this method were its high level of accuracy and need for only input values often provided by the manufacturer such as the short circuit current (I_{sc}), open circuit voltage (V_{oc}), and the values of current and voltage at maximum power point (I_{mp} and V_{mp} respectively). The value of the diode quality factor was assumed to be known or otherwise set to one as suggested elsewhere (Carrero et al., 2010) for this method. It was found, however, that making the latter assumption resulted in significant error when examining the model performance over the entire I–V curve in comparison to experimental data as shown by Fig. 1. By adjusting the value of n, and re-calculating the values of R_s and R_{sh}, the authors observed a reduction in this disparity between model output and experimental values yielding an improved fit overall.

A sensitivity analysis was carried out by the authors to examine the effect of changing the diode constant (n) on the series and shunt resistance values. Fig. 2 plots the variation obtained in resistance values as the diode constant is incremented in steps of 0.05 starting from a value of one.

From Fig. 2 we can see that by increasing the diode constant, a drop in R_s and a rise in R_{sh} are obtained. The ideal combination of R_s, R_{sh}, and n will minimise some error criterion. In this study, the root mean square error (RMSE) analysis was performed in order to compare results of the simulated current vector against experimental values (see Sections 3 and 4 for detailed method). The simulated current vector was calculated using Eq. (5) utilising values for R_s and R_{sh} found by applying the method of Ghani and Duke (2011) for each value of n conducted in the sensitivity analysis. This simulated current vector was then compared to experimental values. Fig. 3 plots the RMSE value against the diode constant value. From Fig. 3 we can see that RMSE is gradually reduced as we increment the diode constant from one however a local minimum exists at approximately $n = 1.55$. From this point on, RMSE begins to rise.

The results of this sensitivity analysis have demonstrated that the simulated results of a photovoltaic system analysis can be improved with the appropriate selection of values R_s, R_{sh}, and n. Consequently we propose here a modifica-

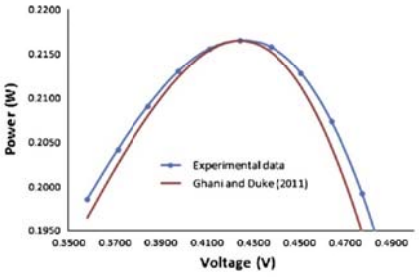

Fig. 1. A comparison of the power-voltage curve generated using the method of Ghani and Duke (2011) against experimental data for a multicrystalline cell exposed to 1000 W/m^2 of illumination.

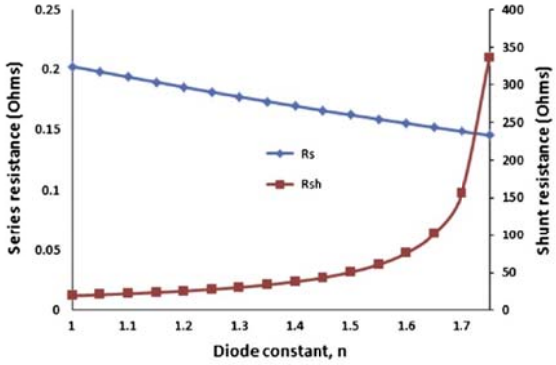

Fig. 2. Values for R_s and R_{sh} for different values of n using the method of Ghani and Duke (2011).

tion to the method of Ghani and Duke (2011) so that the value of the diode constant may also be determined. The method is simple to apply and was found to significantly reduce error based on a root mean square analysis of the model and experimental current vectors.

2. Theory of method

An overview of the proposed method is shown by Fig. 4. The proposed method is a modification to the method of Ghani and Duke (2011) however the part of the method devoted to calculating the values of R_s and R_{sh} is unchanged. In this work, the values of R_s and R_{sh} are numerically calculated at maximum power point (MPP) using data provided by the manufacturer (i.e. I_{sc}, V_{oc}, I_{mp}, and V_{mp}) and a value for the diode quality factor. Here we provide a modification to the original algorithm so that n, the diode constant may also be calculated with coupled values R_s and R_{sh} without introducing further experimentation.

The values of R_s and R_{sh} are calculated by solving a system of non-linear equations which describe the behaviour of a solar cell at maximum power point. This system is solved for R_s and R_{sh} by using a multi-variable version of the Newton–Raphson equation. By starting with two initial estimates for series ($R_{s,i}$) and shunt resistance ($R_{sh,i}$), the updated values (R_{si+1} and R_{shi+1} respectively) can be found using Eqs. (5) and (6) (Chapra and Canale, 2002). Convergence is rapidly achieved provided initial estimates for R_s and R_{sh} are chosen within vicinity of the actual roots. If these values are not local, an error may result. To avoid this scenario, the approximate location of the roots can be obtained by generating contour plots as recommended by Ghani and Duke (2011) for a diode constant value of one.

$$R_{si+1} = R_{s,i} - \frac{z_i \frac{\partial w_i}{\partial R_{sh}} - w_i \frac{\partial z_i}{\partial R_{sh}}}{\frac{\partial z_i}{\partial R_s}\frac{\partial w_i}{\partial R_{sh}} - \frac{\partial z_i}{\partial R_{sh}}\frac{\partial w_i}{\partial R_s}} \tag{6}$$

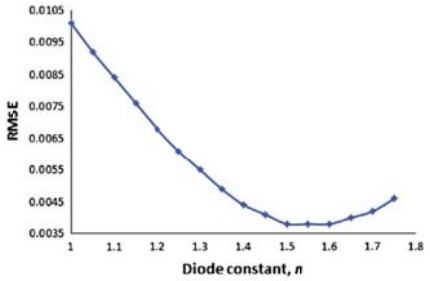

Fig. 3. Root mean square error values as a result of varying the diode constant n. Values for series and shunt resistance used for Eq. (5) were found using Ghani and Duke (2011). Simulated values were compared against experimental value collected for a single multi-crystalline cell exposed to 1000 W/m^2 of illumination.

$$R_{shi+1} = R_{sh,i} - \frac{w_i \frac{\partial z_i}{\partial R_s} - z_i \frac{\partial w_i}{\partial R_s}}{\frac{\partial z_i}{\partial R_s}\frac{\partial w_i}{\partial R_{sh}} - \frac{\partial z_i}{\partial R_{sh}}\frac{\partial w_i}{\partial R_s}} \tag{7}$$

where expression z was derived by substituting the values of I_{mp} and V_{mp} for I and V respectively into Eq. (5) yielding Eq. (7).

$$z = \frac{R_{sh}(I_0 + I_{ph})}{(R_s + R_{sh})} - \frac{V_{mp}}{(R_s + R_{sh})} - \frac{nV_{th}}{R_s} LambertW(\theta_1) - I_{MP} = 0 \tag{8}$$

where θ_1 is given by,

$$\theta_1 = \frac{R_s I_0 R_{sh}}{nV_{th}(R_s + R_{sh})} e^{\frac{R_{sh}(R_s I_{ph} + R_s I_0 + V_{mp})}{nV_{th}(R_s + R_{sh})}} \tag{9}$$

Similarly expression w was obtained by examining the P–i curve and knowledge that a global maximum exists at MPP. Therefore,

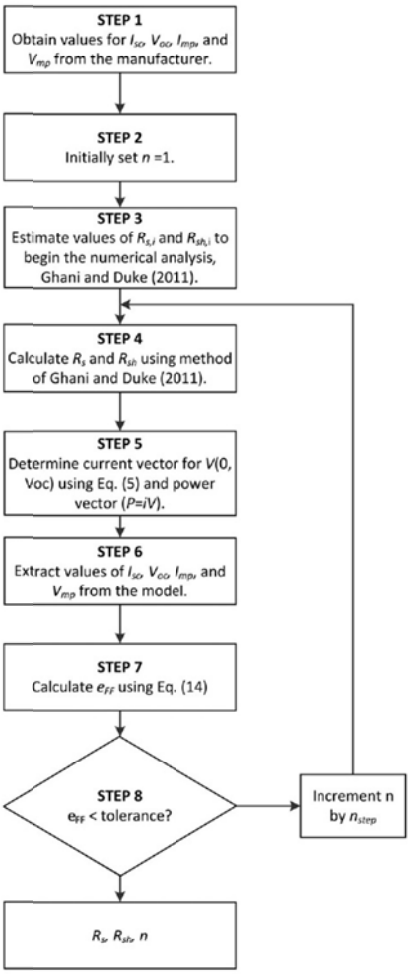

Fig. 4. Algorithm of proposed method to determine the values of R_s, R_{sh}, and n.

$$\frac{\partial P}{\partial i} = 0 \quad _{i=I_{mp}} \tag{10}$$

Equations for the partial derivative of power with respect to i and V have been published previously (Jain and Kapoor, 2004). Similar to Eq. (7) we use the partial derivative of P with respect to current to define expression w at MPP by substituting values for i with I_{mp} appropriately.

$$w \equiv R_{sh}I_{ph} + R_{sh}I_0 - 2I_{mp}R_s - 2I_{mp}R_{sh} - nV_{th}LambertW(\theta_2) + I_{mp}R_{sh}\left\{\frac{LambertW(\theta_2)}{[1 - LambertW(\theta_2)]}\right\} - 0 \tag{11}$$

where θ_2 is given by,

$$\theta_2 = \frac{I_0R_{sh}}{nV_{th}}e^{\frac{R_{sh}[I_{mp} + I_{ph} - I_0]}{nV_{th}}} \tag{12}$$

The partial derivatives needed for Eqs. (6) and (7) are provided in Appendix A.

It was assumed for our modelling study that the photogenerated current (I_{ph}) was equal to the short circuit current (I_{sc}) (Chenni et al., 2007).

The method of Ghani and Duke (2011) assumes that the value of the diode constant, n is known. However, by introducing an iterative modification to this method, the value of n can be found to better match the values provided by the manufacturer. If we initially assume a value of unity for the diode constant as recommended elsewhere (Carrero et al., 2010), the corresponding values for R_s and R_{sh} can be found using the method of Ghani and Duke (2011). Applying these calculated values for R_s, and R_{sh}, and the value for n into Eq. (5) we can then obtain the current–voltage as well as the power-voltage array ($P = IV$) from which the values of short circuit current (I_{sc}), open circuit voltage (V_{oc}), current at MPP (I_{mp}), and voltage at MPP (V_{mp}) may be extracted from the model. These values can be applied to find the value of the model output fill factor (FF_{model}) using Eq. (13) (Green, 1998).

$$FF_{model} = \frac{I_{mp,model}V_{mp,model}}{I_{sc,model}V_{oc,model}} \tag{13}$$

The experimental values provided by the manufacturer's data sheets can similarly be used to determine the actual fill factor (FF_{actual}) by substituting the corresponding published values into Eq. (13). Using these two values we introduce the fill factor error term defined by Eq. (14).

$$\varepsilon_{FF} = |FF_{actual} - FF_{model}| \tag{14}$$

The work by Ghani and Duke (2011) demonstrated that high model accuracy at maximum power point was obtained. By introducing an error criterion based on the fill factor, the values of short circuit current and open circuit voltage provided by the manufacturer are now also taken into consideration by the model. By incrementing the value of n by a value which we term n_{step} and calculating the new coupled values of R_s and R_{sh}, ε_{FF} can be incrementally reduced resulting in an improved fit of model data to experimental values. The iterations are stopped once a criterion ($\varepsilon_{tolerance}$) is satisfied. For our study we selected values of 0.0015 and 0.0005 for $\varepsilon_{tolerance}$ and n_{step} respectively. These values were chosen to balance an accurate fit with computational burden and simulation time.

The proposed method was evaluated experimentally using a multi-crystalline cell rated at 500 mA exposed to

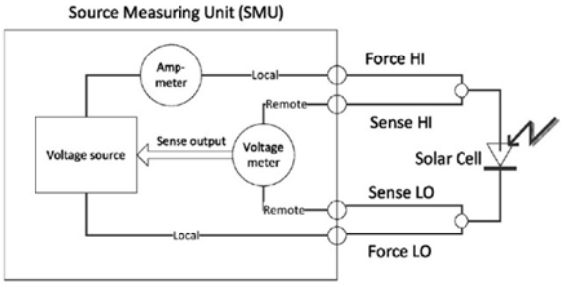

Fig. 5. Wire connection diagram for I–V measurement of cell with SMU.

outdoor illumination at 800, 900, and 1000 W/m^2 in Hamilton, New Zealand.

3. Experimental method

The experimental apparatus is shown in Fig. 3. The current–voltage characteristics of a 500 mA multi-crystalline photovoltaic cell manufactured by Silicon Solar was obtained using a high speed programmable source measuring unit (SMU) manufactured by National Instruments (model NI-PXI-4130). The source measuring unit was used over a traditional power supply because of its precision with respect to both sensitivity and accuracy. For the current range measured in this work, the NI-PXI 130 SMU is stated by the manufacturer to have a current measurement resolution of 10 μA and a measurement accuracy of 0.12%. The SMU was connected to the cell using a four wire or remote sensing scheme to eliminate measurement error introduced by the lead resistance as used in other work (Chan et al., 1986). With the four wire approach, a voltage is sourced across the cell using one pair of leads (Force HI and Force LO, Fig. 5), and the voltage drop across the cell using another pair of leads (Sense HI and Sense LO, Fig. 5). This way any lead resistance could be compensated during measurement. The current voltage characterisation was performed on a cell illuminated outdoors in Hamilton, New Zealand (37°47′S, 175°19′E). An outdoor forward bias test was performed in preference over a dark reverse bias test as it has been acknowledged to yield more accurate values given the realistic operating conditions (Bashahu and Habyarimana, 1995). Radiation was measured using a Middleton Solar EQ-08 pyranometer and logged during measurement. Current voltage measurements were taken at 800, 900, and 1000 W/m^2.

In total, the DC voltage sweep consisted of 75 points from 0 V to V_{oc} (approximately 0.6 V). For each measurement point, 100 samples were taken from which the average value was taken to reduce noise and measurement uncertainty. The cell under test was mounted with good thermal contact using a thin layer (less than 1 mm thick) of thermal adhesive to a high efficiency aluminium heat sink which was mechanically coupled to two 12VDC fans. Convection cooling of the heat sink fins was implemented in order to reduce the rise in operating temperature of the cell during the measurement period which was <5 s. A k-type thermocouple was thermally adhered to the rear side of the cell using a curing heat transfer compound to provide an approximate value of the cell operating temperature (T_{cell}). It was found that temperature rise of the cell was <1 °C for the I–V measurement period at 1000 W/m^2. The entire measurement process was controlled using National Instruments LabView software and the National Instruments PXI-1033 hardware platform. This included all hardware control, parameter extraction, and data logging.

Values for I_{sc}, V_{oc}, I_{mp}, and V_{mp} were extracted directly from the measured current–voltage data in LabView. These values were then used for the method outlined in the previous section and also by the method of Carrero et al. (2010) to determine the values of R_s, R_{sh}, and n.

4. Results and discussion

A single multi-crystalline photovoltaic cell of dimensions 78 × 24 mm was exposed to three levels (800, 900, and 1000 W/m^2) of outdoor illumination in Hamilton, New Zealand. From these current–voltage measurements, the values provided by the manufacturer (I_{sc}, V_{oc}, I_{mp}, and V_{mp}) were obtained and used by three methods to determine certain model characteristics of the cell.These methods were:

(a) The proposed method.
(b) The method of Ghani and Duke (2011).
(c) The method of Carrero et al. (2010).

Results provided in this section indicate that the proposed model offered an improved fit to experimental data over the alternative methods investigated. Values for R_s, R_{sh}, and n obtained by each of the three methods and levels

Table 1
Values for R_s, R_{sh}, and n calculated by each method at 800, 900, and 1000 W/m^2 of illumination.

	800 W/m^2			900 W/m^2			1000 W/m^2		
	Proposed method	Ghani and Duke (2011)	Carrero et al. (2010)	Proposed method	Ghani and Duke (2011)	Carrero et al. (2010)	Proposed method	Ghani and Duke (2011)	Carrero et al. (2010)
R_s	0.1667	0.2171	0.217	0.1541	0.216	0.2178	0.1576	0.2023	0.2024
R_{sh}	71.4699	25.3377	22.0557	63.9571	18.1902	15.4044	65.1712	19.2953	16.2764
n	1.4945	1	1	1.699	1	1	1.5675	1	1

of illumination calculated using Matlab are summarised in Table 1.

The high values for n calculated by the proposed method resulted in significantly higher values of R_{sh} and reduced values for R_s in comparison to the values obtained by Ghani and Duke (2011) and Carrero et al. (2010). A value of $n = 1.5675$ is obtained when illuminated at 1000 W/m^2 which coincides with the global maximum of Fig. 3.

Parameter values summarised in Table 1 were then used as inputs into Eq. (5) to determine the model current–voltage characteristics. Values of I_{sc}, V_{oc}, I_{mp}, V_{mp}, P_{max}, and FF summarised in Tables 2–4 were extracted from this simulated data and compared to the experimental data for each level of illumination studied.

Examining the data in Tables 2–4 we make the following observations:

(a) Values for I_{mp}, V_{mp}, and P_{max} using the proposed method and the method of Ghani and Duke (2011) remain essentially unchanged and match their corresponding experimental values with negligible error.
(b) Values obtained using the proposed method for I_{sc} is a better match to experimental values over the method of Ghani and Duke (2011) resulting in a more accurate value of the fill factor.

In order to assess the accuracy of each method over the entire I–V curve, a mean square error (MSE) and root mean square error (RMSE) analysis was carried out. The mean square error and root mean square error values were calculated using Eqs. (15) and (16) respectively.

$$\mathrm{MSE}(i_{\exp}, i_{model}) = \frac{1}{N}\sum_{i=1}^{N}(i_{\exp} - i_{model})^2 \tag{15}$$

$$\mathrm{RMSE} = \sqrt{\mathrm{MSE}} \tag{16}$$

Table 2
Experimental and model parameters extracted from the I–V curves at 800 W/m^2.

	I_{sc}	V_{oc}	I_{mp}	V_{mp}	P_{max}	FF
Experimental	0.4574	0.5792	0.4069	0.4212	0.1714	0.6468
Proposed method	0.4563	0.5797	0.4065	0.4216	0.1714	0.6478
Ghani and Duke (2011)	0.4535	0.5797	0.4065	0.4216	0.1714	0.6519
Carrero et al. (2010)	0.4529	0.5797	0.4042	0.4216	0.1704	0.6490

Table 3
Experimental and model parameters extracted from the I–V curves at 900 W/m^2.

	I_{sc}	V_{oc}	I_{mp}	V_{mp}	P_{max}	FF
Experimental	0.5122	0.5879	0.4495	0.4213	0.1894	0.6288
Proposed method	0.5110	0.5885	0.4491	0.4216	0.1894	0.6297
Ghani and Duke (2011)	0.5062	0.5885	0.4491	0.4216	0.1894	0.6357
Carrero et al. (2010)	0.5051	0.5885	0.4443	0.4216	0.1873	0.6303

Table 4
Experimental and model parameters extracted from the I V curves at 1000 W/m^2.

	I_{sc}	V_{oc}	I_{mp}	V_{mp}	P_{max}	FF
Experimental	0.5768	0.5965	0.5100	0.4244	0.2164	0.6290
Proposed method	0.5754	0.5969	0.5098	0.4245	0.2164	0.6301
Ghani and Duke (2011)	0.5708	0.5969	0.5099	0.4245	0.2165	0.6352
Carrero et al. (2010)	0.5697	0.5969	0.5060	0.4245	0.2148	0.6316

where N is the number of samples, i_{exp} and i_{model} are the experimental and model values for current respectively. Table 5 summarises the results of our statistical analysis.

The results presented in Table 5, demonstrate greatest accuracy is observed in all cases using the proposed method. For instance, looking at the data for 1000 W/m^2 the proposed method yields over 60% and 70% improvement over the methods of Ghani and Duke (2011) and Carrero et al. (2010) respectively based on a root mean square error analysis.The relative efficiency calculation defined by Eq. (17) (Montogomery et al., 2011) further validates the improved model efficiency of the proposed method to the alternative methods studied. Relative efficiency values are given in Table 6.

$$RelativeEfficiency = \frac{\mathrm{MSE}(\varphi_{proposed})}{\mathrm{MSE}(\varphi_{alternative})} \tag{17}$$

Values of relative efficiencies presented in Table 6 are less than one in all cases indicating a better model match with experimental data with the proposed method.

Current–voltage curves for each level of illumination using the proposed method and the method of Ghani and Duke (2011) are plotted against experimental data in Fig. 6. An accurate fit is obtained by both models at

Table 5
Mean square and root mean square error analysis for each method and illumination.

	800 W/m^2			900 W/m^2			1000 W/m^2		
	Proposed method	Ghani and Duke (2011)	Carrero et al. (2010)	Proposed method	Ghani and Duke (2011)	Carrero et al. (2010)	Proposed method	Ghani and Duke (2011)	Carrero et al. (2010)
MSE	0.00006	0.00011	0.00013	0.00002	0.00013	0.00018	0.00001	0.00010	0.00015
RMSE	0.0080	0.0105	0.0115	0.0045	0.0113	0.0135	0.0037	0.0101	0.0124

Table 6
Relative efficiency values determined using Eq. (17) for each level of illumination.

	800 W/m^2	900 W/m^2	1000 W/m^2
Ghani and Duke (2011)	0.576	0.161	0.137
Carrero et al. (2010)	0.477	0.113	0.091

Table 7
RMSE error values against experimental data at varying levels of illumination. Values for R_s, R_{sh}, and n were determined at 1000 W/m^2 only using the method of Ghani and Duke (2011) and the proposed method.

Method	n	RMSE			
		800 W/m^2	900 W/m^2	1000 W/m^2	Average
Ghani and Duke (2011)	1	0.0108	0.0092	0.0101	0.0100
Proposed method	1.5675	0.0091	0.0065	0.0037	0.0064

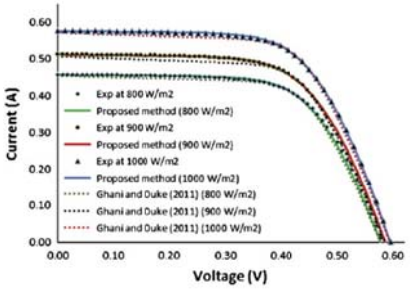

Fig. 6. Model and experimental current–Voltage curves at 800, 900, and 1000 W/m^2 of radiation. Solid circles represent experimental data while solid and dashed lines represent data obtained using the proposed method and the method of Ghani and Duke (2011) respectively.

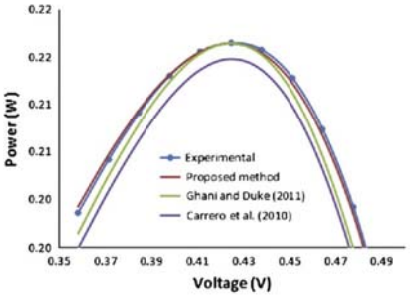

Fig. 7. Experimental and model P–V curves at MPP for1000 W/m^2 of illumination.

MPP but the proposed method demonstrates an improved fit over the entire voltage array.

Fig. 7 plots the experimental power-voltage data along with data generated by each of the methods investigated in this study in the vicinity of maximum power point at 1000 W/m^2 of illumination. The methods of Ghani and Duke (2011) and Carrero et al. (2010) with a diode constant of one both deviate from experimental data particularly away from MPP. The proposed method however closely matches experimental data over a greater range of voltage values.

The accuracy of the proposed method is dependent on the criterion value $\varepsilon_{tolerance}$ and the value for n_{step} chosen. By choosing selecting small values for both however, the simulation time is increased. A compromise must therefore be made to balance accuracy and computational burden.

Inspecting Table 1, we can see that parameter values are a function of the irradiance intensity. Simulation results presented so far have been carried out using parameter values R_s, R_{sh}, and n that have been calculated at each level of irradiance. The question arises, which values should be used for simulating photovoltaic systems? A dynamic model would be ideal, where parameters values [R_s, R_{sh}, and n] are calculated for a given irradiance value. Such a model will reduce error however this would require extensive experimental work for the specific device under analysis as well as significant computational effort in parameter evaluation. The advantage of the method proposed in this work is that it can be performed using data provided by the manufacturer. The manufacturer of a photovoltaic device typically publishes the values for I_{sc}, V_{oc}, I_{mp}, and V_{mp} at standard test conditions (1000 W/m^2, 25 °C). Using these published values, the proposed method can be used to determine R_s, R_{sh}, and n and implemented to simulate the behaviour of the device operating under vary-

Table B1
Experimental and simulated data for each method investigated at $G = 1000\ W/m^2$.

	$G = 1000\ W/m^2$							
	Experimental data		Proposed		Ghani and Duke (2011)		Carrero et al. (2010)	
Voltage (V)	I (A)	P (W)	I (A)	P (W)	I (A)	P (W)	I (A)	P (W)
0.0000	0.5768	0.0000	0.5754	0.0000	0.5708	0.0000	0.5697	0.0000
0.0133	0.5768	0.0077	0.5752	0.0076	0.5701	0.0076	0.5689	0.0075
0.0265	0.5772	0.0153	0.5750	0.0153	0.5695	0.0151	0.5681	0.0151
0.0398	0.5763	0.0229	0.5748	0.0229	0.5688	0.0226	0.5673	0.0226
0.0531	0.5757	0.0305	0.5746	0.0305	0.5681	0.0301	0.5665	0.0301
0.0663	0.5760	0.0382	0.5744	0.0381	0.5674	0.0376	0.5657	0.0375
0.0796	0.5755	0.0458	0.5742	0.0457	0.5667	0.0451	0.5649	0.0450
0.0929	0.5754	0.0534	0.5740	0.0533	0.5661	0.0526	0.5641	0.0524
0.1061	0.5750	0.0610	0.5738	0.0609	0.5654	0.0600	0.5633	0.0598
0.1194	0.5748	0.0686	0.5735	0.0685	0.5647	0.0674	0.5625	0.0672
0.1327	0.5747	0.0762	0.5733	0.0761	0.5640	0.0748	0.5617	0.0745
0.1459	0.5745	0.0838	0.5731	0.0836	0.5633	0.0822	0.5609	0.0818
0.1592	0.5742	0.0914	0.5729	0.0912	0.5626	0.0896	0.5601	0.0892
0.1724	0.5735	0.0989	0.5726	0.0987	0.5620	0.0969	0.5592	0.0964
0.1857	0.5730	0.1064	0.5724	0.1063	0.5613	0.1042	0.5584	0.1037
0.1990	0.5725	0.1139	0.5721	0.1138	0.5606	0.1115	0.5576	0.1110
0.2122	0.5715	0.1213	0.5718	0.1214	0.5599	0.1188	0.5568	0.1182
0.2255	0.5707	0.1287	0.5714	0.1289	0.5592	0.1261	0.5560	0.1254
0.2388	0.5704	0.1362	0.5710	0.1363	0.5585	0.1334	0.5552	0.1326
0.2520	0.5696	0.1436	0.5705	0.1438	0.5578	0.1406	0.5544	0.1397
0.2653	0.5691	0.1510	0.5699	0.1512	0.5571	0.1478	0.5535	0.1468
0.2786	0.5682	0.1583	0.5692	0.1586	0.5563	0.1550	0.5526	0.1539
0.2918	0.5669	0.1655	0.5682	0.1658	0.5555	0.1621	0.5517	0.1610
0.3051	0.5653	0.1725	0.5669	0.1730	0.5546	0.1692	0.5507	0.1680
0.3184	0.5634	0.1794	0.5653	0.1800	0.5536	0.1762	0.5495	0.1750
0.3316	0.5613	0.1861	0.5631	0.1867	0.5523	0.1832	0.5482	0.1818
0.3449	0.5581	0.1925	0.5602	0.1932	0.5507	0.1899	0.5464	0.1885
0.3582	0.5544	0.1986	0.5563	0.1992	0.5484	0.1964	0.5441	0.1949
0.3714	0.5497	0.2042	0.5511	0.2047	0.5452	0.2025	0.5408	0.2009
0.3847	0.5435	0.2091	0.5444	0.2094	0.5405	0.2079	0.5362	0.2063
0.3980	0.5353	0.2130	0.5355	0.2131	0.5336	0.2124	0.5293	0.2107
0.4112	0.5242	0.2156	0.5242	0.2156	0.5237	0.2154	0.5196	0.2137
0.4245	0.5100	0.2165	0.5098	0.2164	0.5099	0.2165	0.5060	0.2148
0.4378	0.4929	0.2158	0.4921	0.2154	0.4916	0.2152	0.4880	0.2136
0.4510	0.4718	0.2128	0.4706	0.2122	0.4684	0.2113	0.4651	0.2098
0.4643	0.4466	0.2074	0.4451	0.2067	0.4404	0.2045	0.4375	0.2031
0.4776	0.4172	0.1992	0.4155	0.1984	0.4080	0.1948	0.4053	0.1936
0.4908	0.3837	0.1883	0.3820	0.1875	0.3716	0.1824	0.3692	0.1812
0.5041	0.3465	0.1747	0.3445	0.1736	0.3318	0.1672	0.3296	0.1662
0.5173	0.3055	0.1581	0.3033	0.1569	0.2891	0.1495	0.2871	0.1485
0.5306	0.2612	0.1386	0.2588	0.1373	0.2439	0.1294	0.2422	0.1285
0.5439	0.2140	0.1164	0.2112	0.1148	0.1966	0.1070	0.1951	0.1061
0.5571	0.1642	0.0915	0.1607	0.0895	0.1477	0.0823	0.1462	0.0815
0.5704	0.1122	0.0640	0.1078	0.0615	0.0972	0.0554	0.0959	0.0547
0.5837	0.0579	0.0338	0.0525	0.0307	0.0454	0.0265	0.0443	0.0258
0.5969	0.0024	0.0014	−0.0047	−0.0028	−0. 0074	−0.0044	−0.0085	−0.0051

ing levels of illumination as typically carried out. Table 7 summarises the results of a root mean square error analysis conducted against experimental data and simulated data at three level of illumination. Parameter values were found using the method of Ghani and Duke (2011) and the proposed method at 1000 W/m^2 of irradiance only. Based on these results we can see that the average RMSE error is over 30% less using the proposed method as a result of calculating the diode constant. The proposed method therefore can be used to determine parameters values [R_s, R_{sh}, and n] at STC using data provided by the manufacturer. These values can then be applied for simulating PV output at varying levels of irradiance with improved accuracy over alternative methods which assumes a diode constant of unity.

5. Conclusion

A new method has been proposed to determine the values of series and shunt resistances and diode constant

of a solar cell by modifying the method of Ghani and Duke (2011). An experimental assessment has revealed that the proposed method offers an improvement in modelling accuracy over two alternative methods. By altering the value of the diode constant, the coupled values of R_s and R_{sh} were shown to change significantly. The principal advantage of this method is that it only requires data often provided by the manufacturer. A disadvantage however is the computational burden and time needed to carry out the additional calculations over the original method of Ghani and Duke (2011) and the need to evaluate the Lambert W-function. It was found that although parameter values will vary with irradiance, values calculated with the proposed method at 1000 W/m^2 yield more accurate results over parameter values found assuming a diode constant of unity.

Appendix A. Partial differential equations

Partial differential equations required for Eqs. (6) and (7) (Ghani and Duke, 2011).

$$\frac{\partial z}{\partial R_s} = \frac{V_{mp}}{(R_s+R_{sh})^2} - \frac{(R_{sh}I_0 + R_{sh}I_{ph})}{(R_s+R_{sh})^2} + \frac{nV_{th}}{R_s^2} LambertW(\theta_1) - \frac{nV_{th}}{R_s}\frac{LambertW(\theta_1)}{[1+LambertW(\theta_1)]\theta_1}\frac{\partial \theta_1}{\partial R_s} \quad (A.1)$$

$$\frac{\partial \theta_1}{\partial R_s} = \frac{I_0 R_{sh}(nV_{th}R_s + nV_{th}R_{sh}) - nV_{th}(R_sI_0R_{sh})}{(nV_{th}R_s + nV_{th}R_{sh})^2} e^{\frac{R_{sh}(R_sI_{ph}+R_sI_0-V_{mp})}{nV_{th}(R_s+R_{sh})}} - \frac{R_sI_0R_{sh}}{nV_{th}(R_s+R_{sh})} \times \frac{(R_{sh}I_{ph}+R_{sh}I_0)(nV_{th}R_s+nV_{th}R_{sh}) - nV_{th}(R_{sh}R_sI_{ph}+R_{sh}R_sI_0-R_{sh}V_{mp})}{[nV_{th}(R_s+R_{sh})]^2} e^{\frac{R_{sh}(R_sI_{ph}+R_sI_0+V_{mp})}{nV_{th}(R_s+R_{sh})}} \quad (A.2)$$

$$\frac{\partial z}{\partial R_{sh}} = \frac{V_{mp}}{(R_s+R_{sh})^2} - \frac{(I_0+I_{ph})(R_s+R_{sh}) - (R_{sh}I_0+R_{sh}I_{ph})}{(R_s+R_{sh})^2} - \frac{nV_{th}}{R_s}\frac{LambertW(\theta_1)}{[1+LambertW(\theta_1)]\theta_1}\frac{\partial \theta_1}{\partial R_{sh}} \quad (A.3)$$

$$\frac{\partial \theta_1}{\partial R_{sh}} = \frac{R_sI_0(nV_{th}R_s + nV_{th}R_{sh}) - nV_{th}(R_sI_0R_{sh})}{[nV_{th}(R_s+R_{sh})]^2} e^{\frac{R_{sh}(R_sI_{ph}+R_sI_0+V_{mp})}{nV_{th}(R_s+R_{sh})}} + \frac{R_sI_0R_{sh}}{nV_{th}(R_s-R_{sh})} \times \frac{(R_sI_{ph}+R_sI_0+V_{mp})(nV_{th}R_s+nV_{th}R_{sh}) - nV_{th}(R_{sh}R_sI_{ph}+R_{sh}R_sI_0+R_{sh}V_{mp})}{(nV_{th}R_s-nV_{th}R_{sh})^2} e^{\frac{R_{sh}(R_sI_{ph}+R_sI_0+V_{mp})}{nV_{th}(R_s+R^{sh})}} \quad (A.4)$$

$$\frac{\partial w}{\partial R_s} = -2I_{mp} \quad (A.5)$$

$$\frac{\partial w}{\partial R_{sh}} = I_{ph} + I_0 - 2I_{mp} - V_{th}\left\{\frac{LambertW(\theta_2)}{[1+LambertW(\theta_2)]\theta_2}\frac{\partial \theta_2}{\partial R_{sh}}\right\} + I_{mp}\left\{\frac{LambertW(\theta_2)}{[1+LambertW(\theta_2)]\theta_2}\right\} + I_{mp}R_{sh}\left\{\frac{LambertW(\theta_2)}{[1-LambertW(\theta_2)]^2\theta_2}\frac{\partial \theta_2}{\partial R_{sh}}\right\} \quad (A.6)$$

$$\frac{\partial \theta_2}{\partial R_{sh}} = \frac{I_0}{nV_{th}} e^{\frac{R_{sh}(-I_{mp}+I_{ph}+I_0)}{nV_{th}}}\left\{1 + \frac{R_{sh}(-I_{mp}+I_{ph}+I_0)}{nV_{th}}\right\} \quad (A.7)$$

Appendix B. Experimental data

Table B1 provides experimental and simulated data for each of the three methods investigated at $G = 1000$ W/m^2. Data is provided up to approximately V_{oc}.

References

Bashahu, M., Habyarimana, A., 1995. Review and test of methods for determination of the solar cell series resistance. Renewable Energy 6, 129–138.

Carrero, C., Rodriguez, J., Ramirez, D., Platero, C., 2010. Simple estimation of PV modules loss resistances for low error modelling. Renewable Energy, 1103–1108.

Celik, A.N., Acikgoz, N., 2007. Modelling and experimental verification of the operating current of mono-crystalline photovoltaic modules using four-and five-parameter models. Applied Energy 84, 1–15.

Chan, D.S., Phang, J.C.H., 1987. Analytical methods for the extraction of solar-cell single- and double-diode model parameters from I–V characteristics. IEEE Transactions on Electron devices 34, 286–293.

Chan, D.S., Phillips, J.R., Phang, J.C.H., 1986. A comparative study of extraction methods for solar cell model parameters. Solid-State Electronics 29, 329–337.

Chapra, S.C., Canale, R.P., 2002. Numerical methods for engineers: with software and programming applications, fourth ed. McGraw-Hill, New York.

Chenni, R., Makhlouf, M., Kerbache, T., Bouzid, A., 2007. A detailed modeling method for photovoltaic cells. Energy 32, 1724–1730.

De Soto, W., Klein, S.A., Beckman, W.A., 2006. Improvement and validation of a model for photovoltaic array performance. Solar Energy 80, 78–88.

Ghani, F., Duke, M., 2011. Numerical determination of parasitic resistances of a solar cell using the Lambert *W*-function. Solar Energy 85, 2386–2394.

Green, M.A., 1998. Solar Cells Operating Principles, Technology and System Applications. University of New South Wales.

Jain, A., Kapoor, A., 2004. Exact analytical solutions of the parameters of real solar cells using Lambert *W*-function. Solar Energy & Materials 81, 269–277.

Jain, A., Sharma, S., Kapoor, A., 2006. Solar cell array parameters using Lambert *W*-function. Solar Energy & Materials 90, 25–31.

Montogomery, D.C., Runger, G.C., Hubele, N.F., 2011. Engineering Statistics, fifth ed. John Wiley & Sons, Chichester.

Petrone, G., Spagnuolo, G., Vitelli, M., 2007. Analytical model of mismatched photovoltaic fields by means of Lambert *W*-function. Solar Energy Materials and Solar Cells 91, 1652–1657.

Picault, D., Raison, B., Bacha, S., de la Casa, J., Aguilera, J., 2010. Forecasting photovoltaic array power production subject to mismatch losses. Solar Energy 84, 1301–1309.

van Dyk, E.E., Meyer, E.L., 2004. Analysis of the effect of parasitic resistances on the performance of photovoltaic modules. Renewable Energy 29, 333–344.

Villalva, M.G., Gazoli, J.R., Filho, E.R., 2009. Comprehensive approach to modeling and simulation of photovoltaic arrays. IEEE Transactions on Power Electronics 24, 1198–1208.

Chapter 7: Effect of flow distribution on the photovoltaic performance of a building integrated photovoltaic/thermal (BIPVT) collector

7.0 Introduction

Combining the results from Chapters 3 to 6, a numerical investigation was performed to analyse the effect of flow distribution on the photovoltaic yield of a BIPVT collector. The four factors examined in Chapter 3 were again varied as the results indicated that influences of all four factors were statistically significant to flow distribution. A three-step analysis consisting of a fluid analysis, a heat transfer analysis, and a photovoltaic system analysis was executed. The finite element method was again used to quantify the flow rates through each riser; however for this investigation, nine array geometries were investigated (as opposed to only two) given its significant impact on flow distribution.

The significant addition to this investigation in comparison to the study presented in Chapter 3 is the photovoltaic system model. The model generated incorporates the research conducted into the photovoltaic system parameter calculation discussed in Chapters 4 through to 6. By applying Kirchhoff's current and voltage laws, the system of non-linear equations was solved using numerical methods such that the individual operating temperature of each cell in the array was taken into consideration. All programming was performed using Matlab software.

Results indicated that flow distribution will have a strong influence on the photovoltaic output of a BIPVT collector. For the case where flow distribution was poorest, photovoltaic output was improved by only 2% over a traditional photovoltaic system with no cooling. However for the case where flow distribution was optimal, photovoltaic output was improved by over 9%. If the issue of flow distribution is not appropriately addressed, the theoretical improvement in electric output from the photovoltaic system as

a result of cooling may be minimal. Such a scenario would not justify the additional costs and complexity associated with the implementation of the active heat recovery system.

7.1 Journal Paper: Effect of flow distribution on the photovoltaic performance of a building integrated photovoltaic/thermal (BIPVT) collector

Available online at www.sciencedirect.com
SciVerse ScienceDirect
Solar Energy 86 (2012) 1518–1530
SOLAR ENERGY
www.elsevier.com/locate/solener

Effect of flow distribution on the photovoltaic performance of a building integrated photovoltaic/thermal (BIPV/T) collector

F. Ghani *, M. Duke, J.K. Carson

School of Engineering, University of Waikato, Hamilton 3240, New Zealand

Received 15 October 2011; received in revised form 12 January 2012; accepted 16 February 2012
Available online 23 March 2012

Communicated by: Associative Editor Brian Norton

Abstract

The phenomenon of non-uniform flow distribution and its influence on thermal performance within a traditional solar thermal collector is well known. Its effect on the photovoltaic conversion of a hybrid photovoltaic/thermal (PV/T) collector however has received little attention. In this study an investigation has been carried out to determine what effect flow distribution will have on the photovoltaic yield of a BIPV/T collector of various size. A three step numerical analysis was conducted to model flow distribution, temperature variation, and photovoltaic yield for a PV/T collector of various design (manifold sizes), geometric shape (aspect ratio), and operating characteristics (mass flow rate and flow direction in manifolds) in order to vary flow uniformity within the collector. The results revealed that flow distribution within the collector will have a significant influence on the photovoltaic performance of a hybrid PV/T collector. For the scenario where flow distribution was most uniform, photovoltaic performance was improved by over 9% in comparison to a traditional photovoltaic (PV) collector operating under the same conditions. For poor flow however, performance was only improved by approximately 2%. Parameters found to influence flow distribution include the manifold to riser pipe ratio where a ratio of 4:1 was found to be ideal and that increasing to a 6:1 ratio offered negligible improvement. Additionally it was found that array geometry (characterised by its aspect ratio in this study) plays an important role on both flow distribution and photovoltaic yield. This study has identified that the optimal mass flow rate is dependent on the shape or aspect ratio of the array.

Keywords: Building integrated; Flow distribution; Photovoltaic; Hybrid collector; PV/T

1. Introduction

A photovoltaic/thermal hybrid collector (henceforth referred to as a PV/T collector) is a device capable of the simultaneous conversion of radiant solar energy into both electricity and thermal energy. These collectors consist of a photovoltaic (PV) panel responsible for the conversion of solar energy into electricity due to the Becquerel/photovoltaic effect, and thermal energy via an absorption process (Santbergen and van Zolingen, 2006). Depending on the type, a common PV module will convert 5–20% of incoming radiation into electricity (Santbergen et al., 2010). The remaining portion (a value >50% after deducting the reflected portion) is absorbed and converted to heat (Chow, 2010). Consequently the operating temperature of the cell will increase with temperatures 50 °C above ambient obtainable under certain conditions.

The performance decay of photovoltaic systems due to temperature is well documented and reviewed elsewhere (Skoplaki and Palyvos, 2009). In summary, it has a negative effect on the open circuit voltage and the fill factor of the cell while marginally increasing the short circuit current due to a reduction in bandgap energy. For detail regarding parameters of a solar cell sensitive to temperature, the reader is referred to the following literature (Bludau

* Corresponding author. Tel.: 164 220180398.
E-mail address: fag2@waikato.ac.nz (F. Ghani).

0038-092X/$ - see front matter © 2012 Elsevier Ltd. All rights reserved.
http://dx.doi.org/10.1016/j.solener.2012.02.013

et al., 1974; Emery et al., 1996; Radziemska and Klugmann, 1999, 2002; Wysocki and Rappaport, 1959). The overall effect however is an approximate drop of 0.5%/°C conversion efficiency for silicon based cells (Green, 1998).

To reduce the impact of temperature on the performance of a solar system, cooling of cells may be performed by either passive ventilation or active heat recovery. The latter method however has the prospect of increasing the total energy yield of the collector. For example, an experimental study showed that the combined efficiency of a photovoltaic–thermal collector can reach as high as 70% (Athienitis et al., 2005).

Additional advantages of PVT collectors include:

1. Improved energy payback. Calculations performed in another study showed that a PV/T type collector would have an energy payback period of 2 years under an Italian climate whereas individual solar thermal and photovoltaic collectors would be 4.3 and 3.4 years respectively (van Helden et al., 2004).
2. Building integrated PV/T collectors provide architectural uniformity and therefore an aesthetic advantage over conventional photovoltaic and solar thermal technology (Zondag et al., 2002).
3. Fast economic payback. By increasing energy yield per square metre of collector, and reducing material redundancy and installation costs, an economic payback period of less than 2 years has been reported (Erdil et al., 2008).

The potential of such a collector is clear considering that by end-use in Australia for example, the residential building sector comprised of 38% space heating, 30% electricity, 27% water heating, and 4% cooling (Bazilian and Prasad, 2002). Substantial reduction in carbon emissions may be possible for a country such as Australia which is primarily fossil fuel powered and considered one of the sunniest climates in the world.

Active heat recovery collectors to date have predominantly used either air or water as media for thermal transportation. An earlier study looked into the performance of several design variations of a PV/T collector (Zondag et al., 2003). This investigation examined the sheet-and-tube, channel PVT, free flow PVT, and two absorber designs. Their results showed that the channel flow design to offer the highest efficiency. Despite this result, the sheet and tube design commonly used in conventional solar thermal collectors was recommended as a good alternative based on its simpler manufacture and comparable performance. In Greece, a number of PV/T collector designs were investigated with collectors varying in working fluid (air and water), cell type (pc-Si, a-Si), insulation characteristics (glazed and unglazed), and the use of diffuse reflectors to improve radiation distribution (Tripanagnostopoulos et al., 2002). Their results showed that heat extraction by water circulation through a sheet and tube type absorber to be more efficient than air circulation. As such, a building integrated type PV/T collector is currently under development at the University of Waikato based on the sheet and tube design with water circulation. The collector under development is to be manufactured to meet the customers specific roofing requirements. The size and dimensions of the collector will therefore vary case by case. As traditional photovoltaic and solar thermal collectors are manufactured with fixed sizing, a collector manufactured to varying dimensions may behave differently.

The issue of flow distribution and its affect on photovoltaic performance of a BIPV/T collector has been identified as one potential issue and is the topic of this paper. Flow through the PV/T absorber will influence the operating temperature of each photovoltaic cell. Flow uniformity will therefore dictate the variation of temperature over the entire array. It is assumed when carrying out a Hottel–Whillier analysis that flow is evenly distributed and therefore the operating temperature of the cells is homogeneous. However uniform flow is rarely achieved in practice with the quality of flow distribution heavily dependent on a number of parameters. Research into the cause and effects of flow mal-distribution on the performance of traditional solar thermal collectors has been performed in earlier work.

In one study (Chiou, 1982), 16 mathematical models were used to examine the effects of artificially assumed flow distribution on a header/riser type solar thermal array. It was found that flow non-uniformity resulted in a 2–20% deterioration of collector efficiency. The authors recommended in a concluding remark that the effects of flow mal-distribution be considered in the analysis and design of solar (thermal) collectors.

A combined numerical and experimental analysis of a 16 collector array connected in series was investigated in a later study (Wang and Wu, 1990). Their study examined flow distribution and temperature variation over the absorber surface for both parallel and reverse flow in the manifold. For the case of parallel flow in the manifold, central risers registered negligible flow while the risers closest to the inlet and outlet ports of the manifold each received approximately half the total flow. Flow distribution for the case of reverse flow was described on the other hand as a bypass flow pattern were mass flow rate was highest for risers closest to the inlet port with riser flow rate quickly diminishing. Both flow distribution scenarios resulted in large temperature variation over the absorber. Thermal efficiency values reported from their study were 58.5% and 44.5% for the parallel and reverse flow arrays respectively while the theoretical (H W B model) efficiency value was determined to be 73.2%.

Another numerical study (Jones and Lior, 1994) identified three parameters which have a major influence on flow distribution; ratio of riser to manifold diameter (d_r/d_m), the number of risers, and the length of the risers. It was found that by changing the ratio d_r/d_m from 0.25 to 0.75, a change in peak riser flow excess above the average flow to increase by 100 fold. The second most influential factor identified in

this study was that the number of risers with mal-distribution was proportional to n^2 where n is the number of risers.

Studies regarding flow distribution so far have been limited solely to solar thermal applications. In more recent work (Naewngerndee et al., 2011), an investigation was performed to examine the influence of array geometry and mass flow rate on flow characteristics of various PV/T arrays. Their study which consisted of both finite element analysis and experimental work demonstrated that flow distribution was influenced by both factors with lower mass flow rates and fewer risers improving flow distribution. This investigation however did not examine the effect of flow distribution on the temperature and performance of the photovoltaic system which is the focus of this paper.

2. Methods

2.1. Overview of method

An overview of the investigation methodology carried out is given in Fig. 1. Each step shall be discussed individually in the proceeding sections.

2.2. Fluid flow analysis

Water will be actively circulated through an Aluminium extruded collector, cooling the cells and collecting thermal energy via a single fluid riser with a circular cross section. The effects of buoyancy was therefore considered negligible in our study. The internal diameter of the fluid riser (Φ_{riser}) was set at 10 mm for all simulations performed. The header/riser fluid network consists of an inlet header supplying water to each riser and an outlet header collecting water discharged at the riser outlet. Both inlet and outlet header manifolds are assumed circular in cross section.

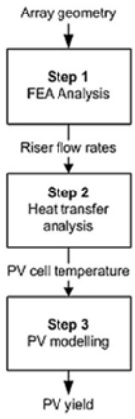

Fig. 1. Overview of method to calculate the photovoltaic yield of a PV/T collector.

To reduce computational burden and time, a 2D planar steady flow analysis as performed in other studies (Chiou, 1982; Wang and Wu, 1990) was assumed adequate for our study. All simulations were conducted using Autodesk Simulation Multi-physics 2012 software. Modelling only the fluid network, the mesh was generated automatically using four node quadrilateral elements operating under the Newtonian viscosity model. Two boundary conditions were specified for our simulation; a surface prescribed velocity at the inlet port of the fluid array dictating the mass flow rate, and a surface prescribed inlet/outlet port at the outlet port face. The former boundary condition dictated the mass flow rate of the fluid circulating through the collector, calculated by Eq. (1) below.

$$\dot{m} = \rho A V \tag{1}$$

where ρ is the density of fluid (kg m^{-3}), A is the cross sectional area of the port face (m^2) and V is the mean fluid velocity (m s^{-1}).

To determine the appropriate size of the elements and balance accuracy and computational effort, a simple convergence analysis was performed. Here we examined the riser mass flow rates of the sixteen riser array (array 4, Table 1) with the element size varying from 0.004 m to 0.00145 m. The inlet mass flow rate was set to 3.555 kg/min. Fig. 2 plots the total riser mass flow rate for each element size.

Based on the results provided by Fig. 2, we can see that values for total riser mass flow rate begin to converge at the desired value of 3.555 kg/min from an element size of 0.002 m. Based on its improved accuracy however, we used an element size of 0.0015 m for all simulations in our study.

In total, three sets of fluid analysis were conducted in order to investigate the influence of flow distribution on photovoltaic performance. Factors identified to influence flow distribution, discussed in the previous section were varied so that its impact on PV output may be understood. These factors are listed below:

1. Array geometry.
2. Area ratio of manifold to riser pipes (Analysis 1).

Table 1
List of array configurations investigated. All arrays are made up of 144 cells.

Array	N_s	N_p	Aspect ratio
1	4	36	0.11
2	6	24	0.25
3	8	18	0.44
4	9	16	0.56
5	12	12	1.00
6	16	9	1.78
7	18	8	2.25
8	24	6	4.00
9	36	4	9.00

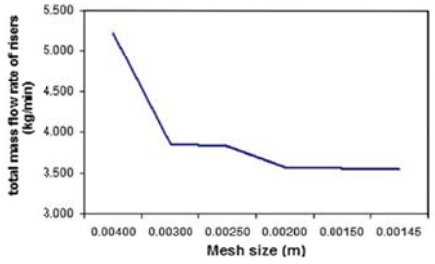

Fig. 2. Results of the mesh convergence analysis. Total riser mass flow rate is plotted against various mesh sizes.

3. Direction of flow in manifold (Analysis 2).
4. Circulation mass flow rate (Analysis 3).

Array geometry in our study specifically refers to the number and length of risers which make the PV/T array. Nine array designs were studied with variation in the number of cells connected in series (N_s) and in parallel (N_p). The total number of interconnected cells for each array was kept at 144 keeping the maximum power point equal for all arrays. Each of the configurations investigated are listed in Table 1 below.

The absorber area for each array was equal to 3.95 m^2 in our study. The shape of the array is indicated by the aspect ratio (AR) value given in the right hand column of Table 1. An array with an aspect ratio of 1 represents a square shaped array, values of $AR < 1$ describes an array which is wide (many risers) and short in the direction of flow, and a value greater than one represents a narrow and long array. The value for AR is determined by Eq. (2) below.

$$AR = \frac{N_s}{N_p} \tag{2}$$

The length of the PV/T absorber is a function of the total number of cells connected in series (N_s) as given by Eq. (3).

$$L_{abs} = (N_s \times 0.165) + 0.015 \tag{3}$$

The number of fluid risers is equal to the number of cells connected in parallel strings. That is,

$$N_{risers} = N_p \tag{4}$$

Therefore, referring to Table 1 we can see that Array 1 consists of an array of 36 parallel strings and risers whereas Array 9 is made up of only four strings and risers.

Additional to geometry, flow distribution is heavily influenced by the ratio of manifold and riser pipe area ($A_{manifold}$ and A_{riser} respectively) as discussed in Section 1. Our study therefore examined three manifold to riser ratios ($A_{manifold}/A_{riser}$): 1, 4, and 6. These values were used in our study to cover the worst case (ratio = 1) to a upper limit (ratio = 6). Only three manifold sizes were studied due to the computational burden of the CFD analysis, however the authors feel this range was adequate. This investigation was performed under Analysis 1 of our study with each of the nine arrays listed in Table 1 simulated with each manifold size, giving a total of 27 simulations. All simulations were conducted with parallel flow in the manifold and a total fluid flow rate of 0.015 kg s^{-1} m^{-2}.

For the second part of our study, the effect of flow direction within the manifold was investigated. Two directions, parallel and reverse flow were investigated (also referred to as reverse return and direct return respectively). Fig. 3 below shows the location of the inlet and outlet ports and direction of flow in manifolds for each configuration.

Each of the nine arrays (Table 1) with an $A_{manifold}/A_{riser} = 4$ were investigated with both flow directions giving a total of 18 simulations. The mass flow rate ($\dot{m}$) of water circulating through the collector was held constant at 0.015 kg/s m^2 for both Analyses 1 and 2. It was mentioned earlier in Section 1 that the mass flow rate will influence flow distribution. Its influence on flow distribution will therefore be investigated in Analysis 3.

Eight mass flow rates were investigated in total for Analysis 3; $\dot{m} = 0.005, 0.01, 0.015, 0.02, 0.025, 0.03, 0.035,$ and 0.04 kg s^{-1} m^{-2}. Here again each of the nine arrays with an $A_{manifold}/A_{riser}$ ratio of four and parallel flow in the manifold was examined. In total, 63 flow simulations were conducted.

2.3. Heat transfer analysis

Variation of fluid flow rate in each riser of a PV/T collector will lead to a temperature variation over the absorber surface. Here we discuss the method used to estimate the temperature of each cell of the array using a modified approach to the classical fin approach (Whillier, 1953, 1977). The overall method is summarised by the flow chart in Fig. 4.

The aim of our analysis is to determine the absorber temperature found by solving Eq. (5) (Duffie and Beckman, 2006).

$$T(x,y) = \frac{(T_b(y) - T_a - S/U_L)\cosh mx}{\cosh m(W-D)/2} + T_a + (S/U_L) \tag{5}$$

where T_b is the bond temperature. T_a is the ambient temperature, S is absorbed radiation (W/m^2), x represents an arbitrary distance perpendicular to fluid flow, W is the distance between tubes (m), D is the riser tube diameter (m), and U_L is the overall heat loss coefficient of the collector (W/m^2 K). The overall heat loss co-efficient for our unglazed collector was taken to be a constant value of 22 W/m^2 K (Anderson et al., 2009) in our study. Absorbed solar radiation (S) contributing to thermal yield was calculated using Eq. (6) which takes into account the photovoltaic electrical efficiency (Zondag et al., 2002).

$$\tau_{\alpha eff} = \tau_\alpha - \tau\eta_{el} \tag{6}$$

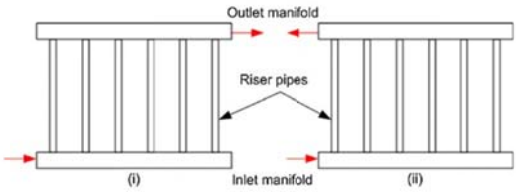

Fig. 3. Diagram depicting the difference in flow connections of a header riser flow network for a parallel flow array (left) and a reverse flow array (right).

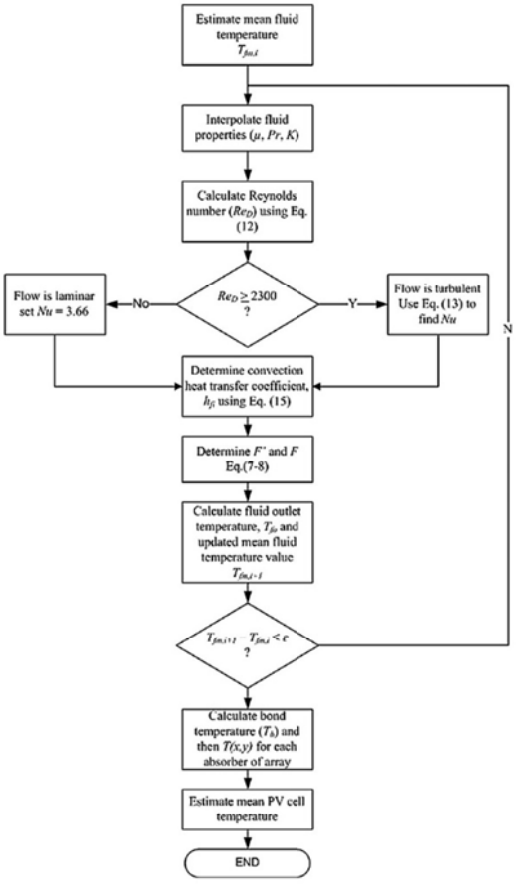

Fig. 4. Algorithm used to determine the values of photovoltaic cell temperature of a PV/T collector.

where $\tau_{\alpha,eff}$ is the effective transmission-absorption factor, τ is the transmissivity of glass, and η_{el} is the electrical efficiency of the photovoltaic cell.

In order to solve Eq. (5), we must first calculate the bond temperature, T_b using Eq. (7) (Duffie and Beckman, 2006).

$$T_b(y) = \frac{WF'[S - U_L(T_f(y) - T_a]}{h_{fi}\pi D_i} + T_f(y) \tag{7}$$

where $T_f(y)$ is the temperature of fluid circulating through the collector, F' is the collector efficiency factor, and h_{fi} is the convective heat transfer coefficient. The fluid temperature will vary in the direction of flow and is therefore a function of y (m). The collector efficiency factor is calculated by (Duffie and Beckman, 2006).

$$F' = \frac{1/U_L}{W\left[\frac{1}{U_L[D+(W-D)/F]} + \frac{1}{\pi D_i h_{fi}}\right]} \tag{8}$$

where F is the standard fin efficiency factor is determined by Eq. (9).

$$F = \frac{\tanh[m(W - D)/2]}{m(W-D)/2} \tag{9}$$

The coefficient m of Eq. (9) is a term which takes into account both the thermal conductivity of the absorber and the PV cell calculated by (Zondag et al., 2002),

$$m = \sqrt{\frac{U_L}{k_{abs}\delta_{abs} + k_{pv}\delta_{pv}}} \tag{10}$$

Temperature distribution in the direction of flow for each riser, $T_f(y)$ needed for Eq. (7) is calculated by Eq. (11) (Duffie and Beckman, 2006).

$$T_f(y) = (T_{fi} - T_a - S/U_L)e^{\left(-\frac{U_L W F' y}{\dot{m} c_p}\right)} + T_a + S/U_L \tag{11}$$

The process of calculating the absorber temperature, $T(x, y)$ begins by initially estimating a value for the mean fluid temperature (T_{fm}) so that fluid properties such as viscosity (μ_f), thermal conductivity (k) and Prandtl number (Pr) can be interpolated from tabulated data. The mean fluid temperature (T_{fm}) is calculated by Eq. (12).

$$T_{fm} = \frac{T_{fo} + T_{fi}}{2} \tag{12}$$

where T_{fo} and T_{fi} represent the values of outlet and inlet fluid temperature respectively. In our study, the inlet fluid temperature, T_{fi} was kept constant at 20 °C. The outlet fluid temperature is found using Eq. (11) with y set to the length of the absorber.

Using the riser mass flow rates determined in our fluid flow analysis, the Reynolds number (Re_D) was calculated using Eq. (13) below with the assumption that flow was steady and incompressible and within a pipe of uniform cross sectional area (Duffie and Beckman, 2006).

$$\mathrm{Re}_D = \frac{4\dot{m}}{\pi D\mu} \tag{13}$$

where D is the pipe diameter of riser pipe and μ is fluid viscosity. For values of $Re_D < 2300$, flow was considered laminar and fully developed. Conservative heat transfer coefficient values was calculated by making the constant wall temperature assumption (Duffie and Beckman, 2006). Here, the Nusselt number (Nu) was taken to be 3.66 (Kays and Crawford, 1993).For the case where flow was not laminar, but developed turbulent flow (i.e. $3000 < Re_D < 5 \times 10^6$, $0.5 < Pr < 2000$), the Nusselt number was calculated with Eq. (14) (Gnielinski, 1976) below.

$$Nu = \frac{(f/8)(\mathrm{Re}_D - 1000)\mathrm{Pr}}{1 + 12.7\sqrt{f/8}(\mathrm{Pr}^{2/3} - 1)} \tag{14}$$

where f is the Darcy friction factor (Incropera et al., 2006) for smooth pipes is given by Eq. (15).

$$f = (0.79\ln \mathrm{Re}_D - 1.64)^{-2} \tag{15}$$

the convective heat transfer coefficient (h_{fi}) of fluid circulating in the riser may then be calculated by re-arranging Eq. (16).

$$Nu = \frac{h_{fi}D}{K} \tag{16}$$

Referring to Fig. 4, once the convective heat transfer coefficient, h_{fi} has been found, the fin efficiency factor, F' and fluid temperature, $T_f(y)$ may be calculated. With the new value of outlet fluid temperature found, the new value for mean fluid temperature, $T_{fm,i+1}$ is calculated using Eq. (12) and compared to the previous value of $T_{fm,i}$. The process of calculating F' and T_{fo} is repeated until the error in subsequent iterations is within the tolerance (ε). As shown by Table 2, the value for error threshold, ε has small effect on the number of iteration performed due to the fast convergence. In our study, a threshold ε-value of 0.01 °C was used.

Final values of F' and T_f were then used to calculate the bond temperature (T_b) and absorber temperature (T) using Eqs. (7) and (5) respectively.

2.4. Photovoltaic system modelling

Similar to previous studies (Petrone et al., 2007; Picault et al., 2010) where modelling of photovoltaic systems was performed using equations based on the Lambert function, we approximated the yield of a PV array operating under heterogeneous temperature. Current as an explicit function

Table 2
Number of iterations required when varying the error threshold ε to calculate the mean fluid temperature.

	ε	No. of iterations
1	0.1	3
2	0.01	3
3	0.001	4
4	0.0001	4

of voltage modelled with the Lambert function is given by Eq. (17) (Jain and Kapoor, 2004).

$$i = -\frac{V}{R_s + R_{sh}} \; \frac{LambertW\left(\frac{R_s I_0 R_{sh} e^{\left(\frac{R_{sh}(R_s I_{ph} - R_s I_0 + V)}{nV_{th}(R_s + R_{sh})}\right)}}{nV_{th}(R_s + R_{sh})}\right) nV_{th}}{R_s} + \frac{R_{sh}(I_0 + I_{ph})}{R_s + R_{sh}} \quad (17)$$

where i and V are the terminal current and voltage in amperes and volts respectively, n is the diode ideality factor, I_{ph} is the photogenerated current (A), I_0 is the diode saturation current (A), R_s and R_{sh} are the series and shunt resistances of the cell respectively (Ω), and V_{th} is the thermal voltage given by Eq. (18).

$$V_{th} = \frac{k_B T}{q} \quad (18)$$

where k_B is the Boltzmann constant (1.38×10^{-23} J/K), T is temperature of the PV cell (K), and q is the charge of an electron (1.602×10^{-19} C).

The photogenerated current (I_{ph}) and diode saturation current (I_0) are calculated by Eqs. (19) and (20) respectively (Chenni et al., 2007).

$$I_{ph} = \left(\frac{G}{G_{ref}}\right)(I_{ph,ref} + \mu_{isc}(T_c - T_{c,ref})) \quad (19)$$

$$I_0 = I_{0,ref}\left(\frac{T_c}{T_{c,ref}}\right)^3 e^{\left[\left(\frac{\varepsilon_G}{kB}\right)\left(\frac{1}{T_{c,ref}} - \frac{1}{T_c}\right)\right]} \quad (20)$$

With G and G_{ref} the values of irradiance at actual and reference conditions (W/m^2), T and T_{ref} values of temperature at actual and reference states (K), μ_{isc} is the temperature decay co-efficient of short circuit current supplied by the manufacturer (A/K), and ε_G is the bandgap energy of the semiconductor (eV). For our analysis consisting of polycrystalline Si cells, the value for bandgap at 25 °C was taken to be 1.12 eV (De Soto et al., 2006). Like I_{ph} and I_0, the bandgap is also a function of temperature decreasing in an approximately linear fashion as shown by Eq. (21) (Radziemska and Klugmann, 2002).

$$\varepsilon_G = \varepsilon_G(300K) + \frac{d\varepsilon_G}{dT}(T - 300K) \quad (21)$$

where for the case of silicon, $d\varepsilon_G/dT = -2.3 \times 10^{-4}$ eV/K (Whillier, 1953).

A number of parameters must be evaluated in order to solve the equations mentioned so far. In the next section we will examine the evaluation procedure carried out.

2.4.1. Parameter evaluation

The unique parameters which dictate the behaviour of a solar cell were estimated based on data provided by the manufacturer as performed in earlier studies (Villalva et al., 2009). Typically, a cell manufacturer will publish experimentally obtained values of open circuit voltage ($V_{oc,ref}$), short circuit current ($I_{sc,ref}$), and values for current and voltage at maximum power point ($I_{mp,ref}$ and $V_{mp,ref}$ respectively) at standard test conditions (STC). To solve Eqs. (19) and (20), we need to find values for $I_{ph,ref}$ and $I_{0,ref}$. In our study, we assumed that the value for $I_{ph,ref}$ was approximately equal to $I_{sc,ref}$ (Chenni et al., 2007). That is,

$$I_{ph,ref} \approx I_{sc,ref} \quad (22)$$

The diode saturation current at reference conditions, $I_{0,ref}$ was approximated by Eq. (23) (Chenni et al., 2007).

$$I_{0,ref} = I_{sc,ref} e^{\left(\frac{-qV_{oc,ref}}{k_B n T_{c,ref}}\right)} \quad (23)$$

Both Eqs. (22) and (23) may be solved by entering values from manufacturer data sheets with the exception of the diode ideality factor, n. The value of n will affect the shape of the 'knee' in vicinity of the maximum power point on the current–voltage curve. Similar to an earlier study (Carrero et al., 2010), we assumed a value of unity for n.

Finally, two parameters remain unknown; series (R_s) and shunt (R_{sh}) resistances. Considering most photovoltaic systems are coupled with maximum power point tracking (MPPT) and will therefore generally operate at this point, resistance values have been specifically calculated at this point in other studies (Carrero et al., 2010; Villalva et al., 2009). A method proposed by the authors in earlier work (Ghani and Duke, 2011) seeks values of R_s and R_{sh} numerically at maximum power point using the Newton–Raphson method based on values supplied by the manufacturer. This method was used to determine the values of a 156 × 156 mm polycrystalline solar cell (Solar Fun model SF156P221-B1). Properties of the cell provided by the manufacturer and values calculated for R_s and R_{sh} are given in Table 3.

Once all the parameters of the cell under investigation were calculated, we determined the total yield of the array, accounting for each cell's performance variation due to temperature variation over the collector.

2.4.2. Calculation of total array output

The series–parallel connected topology shown in Fig. 5 represents the PV system whose output must be found. Kirchhoff's laws were applied to provide an algebraic system of non-linear equations relating all current and voltages in the network similar to earlier work (Quashning and Hanitsch, 1996).

It is assumed the terminal voltage of the array, V is known. Using numerical methods, our aim is to calculate

Table 3
Properties of the polycrystalline cell used in our study.

$I_{sc,ref}$ (A)	$V_{oc,ref}$ (V)	$I_{mp,ref}$ (A)	$V_{mp,ref}$ (V)	R_s (Ω)	R_{sh} (Ω)
8.41	0.613	7.92	0.495	0.0054	12.73

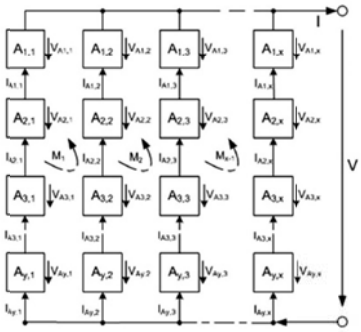

Fig. 5. The general connection scheme of a series–parallel connected PV array. The number of cells connected in series and parallel is denoted y and x respectively.

the unknown voltage values of each cell and the total current I of the PV/T array based on this value. As there are y number of cells connected in series, and x number of strings (see Fig. 5) we must find xy sub-voltages and the total current value making a total of $(x \cdot y + 1)$ unknowns. The vector of unknowns in transposed form, $\boldsymbol{u}^T$ is therefore,

$$\mathbf{u}^{\mathbf{T}} = (V_{A1,1}, \ldots, V_{Ay,x}, I) \tag{24}$$

Using Kirchhoff's current and voltage laws, we begin formulating vector $\boldsymbol{r}$ of non-linear equations in the proceeding steps.

Step 1: The sum of sub-voltages in any string of the array must be equal to the terminal voltage, V. i.e.,

$$r_1(\mathbf{u}) = \sum_{i=1}^{y} V_{Ai,1} - V = 0 \tag{25}$$

Step 2: Apply Kirchhoff's second law (Quashning and Hanitsch, 1996) for each mesh, M of the array which states that the sum of voltages in a mesh must equal zero.

$$r_{2\ldots m+1}(\mathbf{u}) = \sum_{i=1}^{y} V_{i,1} - \sum_{i=1}^{y} V_{i,j} = 0 \tag{26}$$

For j = 2…x.

Step 3: The total current I yields the equation:

$$r_{m+2}(\mathbf{u}) = \sum_{j=1}^{x} I_{A1,j} - I = 0 \tag{27}$$

Step 4: Apply Kirchhoff's first law (Quashning and Hanitsch, 1996). For the case of a series–parallel connected array, the current flowing through two consecutive modules in the same string is identical, that is

$$r_{m+3\ldots m+n+2}(\mathbf{u}) = f(V_{i,j}) - f(V_{i+1,j}) = 0 \tag{28}$$

For $i = 1 \ldots y-1$ and $j = 1 \ldots x$

For the $(x \cdot y + 1)$ unknowns represented by vector $\boldsymbol{u}$, we have an equal number of independent equations represented by vector $r(\boldsymbol{u})$. Our objective is to calculate the values of vector $\boldsymbol{u}$ which satisfy $r(\boldsymbol{u}) = 0$. To do this we used the numerical Newton–Raphson root finding method given by Eq. (29) (Quashning and Hanitsch, 1996).

$$\mathbf{u}_{i+1} = \mathbf{u}_i - (J(\mathbf{u}_i))^{-1} r(\mathbf{u}_i) \tag{29}$$

where $(J(\boldsymbol{u}_i))^{-1}$ is the inverse Jacobian matrix which must be calculated for each iteration. To create the Jacobian matrix, we need to differentiate Eq. (16) with respect to V. The Lambert function may be easily differentiated using Eq. (30) (Corless et al., 1996):

$$\frac{d}{d\theta} LambertW(\theta) = \frac{1}{(1 + LambertW(\theta)) e^{LambertW(\theta)}} \tag{30}$$

Applying Eq. (30) to derive the first order derivate of Eq. (16) with respect to voltage gives,

$$\frac{dI}{dV} = -\frac{1}{(R_{sh} + R_s)} - \frac{R_{sh}}{R_s(R_{sh} + R_s)} LambertW(\theta) \tag{31}$$

where

$$\theta = \frac{R_s I_0 R_{sh}}{n V_{th}(R_s + R_{sh})} e^{\left(\frac{R_{sh}\left(R_s I_{ph} + R_s I_0 + V\right)}{n V_{th}(R_s + R_{sh})}\right)} \tag{32}$$

The Newton Raphson process was initiated by designating each cell voltage to be equal to V/y. Starting with a vector $\boldsymbol{u}_0$, Eq. (28) was repeated until a criterion such as Eq. (32) was satisfied.

$$\|\mathbf{u}_{i+1} - \mathbf{u}_i\| < \varepsilon \tag{33}$$

The final vector $\boldsymbol{u}_{i+1}$ which satisfies Eq. (32) represents the solution vector.

The total characteristic curve of the array may be generated by incrementing the terminal voltage V and calculating the associated current value, I. Once the current voltage (I V) characteristic curve was determined, the power–voltage (P–V) curve was then created ($P = IV$) in order to obtain the value of the maximum power point.

3. Results and discussion

Approximately 100 simulations were completed using the method outlined in the previous section to determine the photovoltaic yield of arrays of various geometry (aspect ratio), design (manifold sizes), and operating conditions (mass flow rate). For each analysis, the flow rate of each riser was approximated in step 1 of our study to establish the flow distribution characteristics. Given the large number of simulations that were conducted, a statistical summary of the flow analysis is only provided to give an overview of the results. Specific flow distribution data will be provided in a follow up paper containing experimental

data. Section 3.2 will briefly provide the results of photovoltaic cell temperature scatter to demonstrate the variation in temperature found due to variation of flow. Finally, photovoltaic yield for each analysis will be presented in section 3.3.

3.1. Flow distribution

Figs. 6–8 each present the results of a statistical analysis for Analyses 1, 2, and 3 respectively with respect to flow distribution. The standard deviation of riser flow rates is calculated to indicate flow uniformity for each array. High values of standard deviation is representative of poor flow distribution. From these graphs we can make the general observation that flow homogeneity in riser flow rate is improved as we increase the aspect ratio of the array from Array 1 ($AR = 0.11$) to Array 9 ($AR = 9$) as this is the trend for each of the three analyses carried out.

Referring to Fig. 6, we can see that an array with a manifold to riser ratio of 1:1 will yield high values of riser flow rate standard deviation and poor flow distribution. A large reduction in riser flow rate variation is found by increasing manifold size to 40 mm followed by only a small improvement by further increasing the manifold size to 60 mm. Based on these results, a manifold diameter of 40 mm or a manifold to riser ratio of 4:1 is recommended as the additional cost of a 60 mm manifold results in negligible improvement in flow uniformity. Section 3.3 will later show this will lead to a negligible improvement in photovoltaic yield.

From Fig. 7, improved flow uniformity is achieved when parallel flow in the manifold is employed over reverse flow for all array geometries. However the values converge as the array geometry is varied from Array 1 to Array 9. From these results parallel flow within the fluid array is generally recommended as proposed elsewhere (Wang and Wu, 1990).

Reducing the circulation flow rate will reduce variation in riser flow rate values as shown by Fig. 8. These results are supported by the combined experiment and numerical analysis reported in an earlier study (Naewngerndee et al., 2011) who reported improved flow uniformity with lower mass flow rates. From this graph we can see that values for standard deviation in riser flow rate converge with an increase in array aspect ratio. A high flow rate therefore may be employed for an array of large aspect ratio (i.e. $AR > 9$) without suffering severe flow mal-distribution.

As a consequence of riser flow imbalance shown so far, each scenario investigated will result in a unique variation in PV cell temperature. The proceeding section will present temperature plots of selected arrays/scenarios.

3.2. Temperature distribution

As fluid flows from the inlet to discharge manifold, we can expect a linear rise in fluid (and therefore cell) temperature. This rise in temperature however will vary from string to string due to variation in riser flow rates. Using the method outlined in Section 2.2, the temperature of the PV/T absorber was approximated based on the results of the fluid analysis. Due to the large number of simulations carried out in this study, each temperature plot cannot be presented here. Extensive plots of temperature variation will be provided in a follow-up paper with experimental results.

Fig. 9 demonstrates the effect of poor flow uniformity on the operating temperature of the PV/T absorber surface. This plot is for a 16 riser array (Array 4) operating with each of the three manifold sizes (10, 40, and 60 mm) with parallel flow in the manifolds. We can see a sharp increase in absorber temperature located in the middle strings for an array with a 10 mm manifold as a direct result of poor flow cooling these strings. Cells being cooled by end risers however operate at lower temperatures due to the comparatively higher flow rate values. A similar temperature variation was reported by Wang and Wu in their experimental study consisting of 10 series connected modules

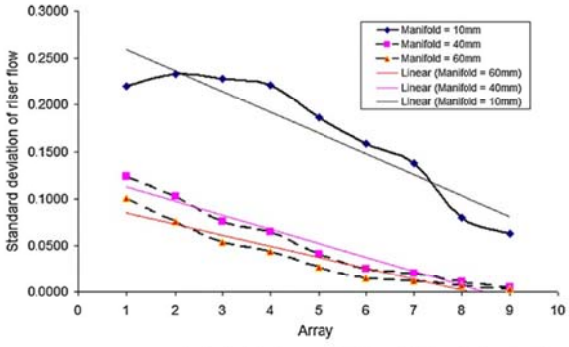

Fig. 6. Standard deviation of riser flow rates when simulated with three manifold sizes (10, 40, and 60 mm) with a riser diameter of 10 mm.

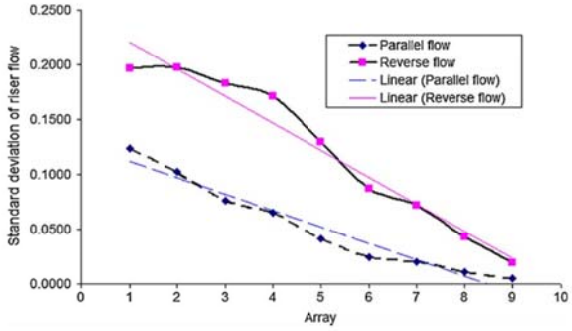

Fig. 7. Standard deviation of riser flow rate for each array when operating under both parallel and reverse flow in the manifolds.

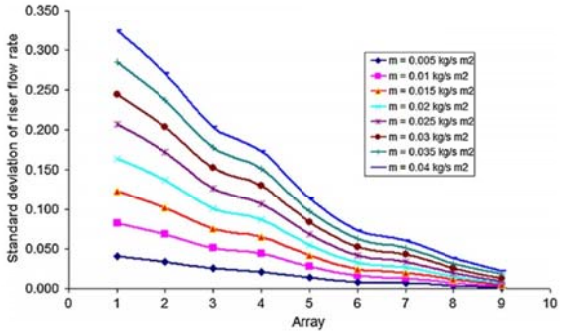

Fig. 8. Standard deviation of riser flow rate for each array simulated with various mass flow rates.

(160 risers). By increasing the manifold size to 40 mm, we see a substantial improvement in temperature distribution as a result of the flow distribution with the middle strings almost 10 °C cooler than the 10 mm manifold array. Due to the minor improvement in flow distribution with the 60 mm manifold, we similarly see a minor improvement in temperature distribution.

As discussed earlier, the performance of silicon type photovoltaic cell is a strong function of temperature. The overall array output will therefore be influenced by temperature variation. The next section will present the results of photovoltaic system modelling based on this temperature variation.

3.3. Photovoltaic yield

Photovoltaic yield of each array simulated under Analyses 1, 2, and 3 are presented in Figs. 10–12 respectively. Here, we make the assumption that the photovoltaic cells operate at the same temperature as the PV/T absorber surface discussed in the previous section. We make this assumption as we intend to directly vacuum laminate the cells onto the PV/T absorber and therefore introduce little thermal resistance between the absorber and cell. In a previous experimental study, researchers who bonded photovoltaic cells to a Aluminium absorber using a silicon based adhesive measured only a 1 °C disparity between absorber and cell temperatures (Lalovic, 1986) supporting our assumption.

The influence of manifold sizing on photovoltaic output is shown by Fig. 10. An array with a 10 mm manifold resulted in reduced yield particularly for arrays one through to five due to poor flow distribution within the array resulting in a large variation in cell operating temperatures. However as the aspect ratio of the array increases from array one to nine, the improved flow distribution leads to an improvement in PV yield. Values converge from array six (i.e. an aspect ratio, $AR > 1.78$) onwards for an array with a 10 mm manifold.

A 40 mm manifold was able to significantly improve photovoltaic output over a 10 mm manifold array although poor flow distribution for Arrays 1 and 2 did affect the total array yield. Photovoltaic yield was found to converge from array three (i.e. $AR > 0.44$) onwards.

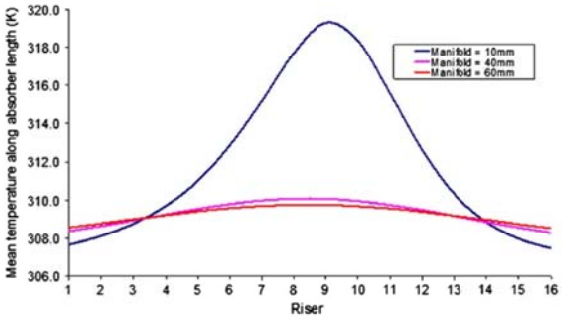

Fig. 9. Mean PV/T absorber temperature along fluid path for array 4 for manifold sizes = 10, 40, and 60 mm.

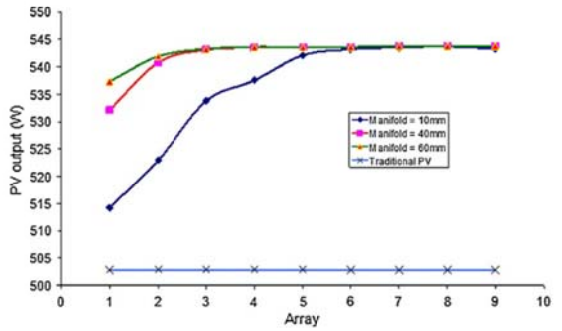

Fig. 10. Results of Analysis 1. Values of photovoltaic yield for each array when simulated with varying manifold sizes (10, 40, 60 mm) with riser diameter 10 mm.

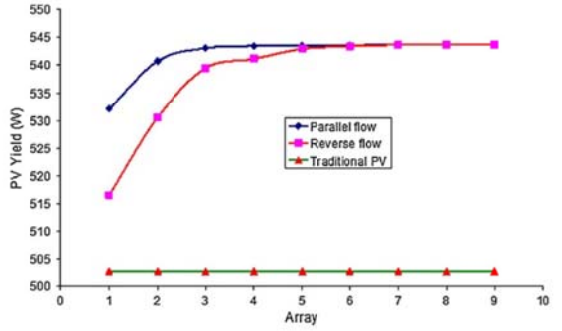

Fig. 11. Results of Analysis 2. Photovoltaic yield of arrays one to nine with a 40 mm manifold and operated with both parallel and reverse flow in the manifold.

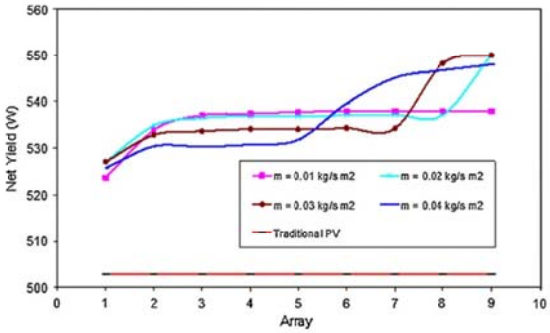

Fig. 12. Results of Analysis 3. Values of photovoltaic yield for each array simulated with varying mass flow rates.

As flow distribution was only marginally improved with a 60 mm manifold, it resulted in minor improvement in photovoltaic yield for Arrays 1 and 2 only. From Array 3 onwards (i.e. $AR > 0.44$), no improvement was obtained over the 40 mm manifold with values of both data sets converging to the same value.

Referring to Fig. 11, the photovoltaic output for Arrays 1–9 operating under both parallel and reverse flow is presented. Arrays 1–4 operating under parallel flow demonstrated improved performance over reverse manifold flow. Values for both arrays however begin to converge from Array 5 (i.e. $AR > 1$) onwards.

Results of Analysis 3 are presented in Fig. 12. Eight mass flow rates in total were simulated in order to determine the optimum value for each of the nine arrays. Unlike Figs. 10 and 11 which plots the photovoltaic yield as the dependent variable, Fig. 12 plots the net yield (P_{net}) of the array to include power consumed by the pump. Pump power (P_{pump}) was calculated using Eq. (33).

$$P_{pump} = \frac{q\rho g h}{3.6 \times 10^3} \tag{34}$$

where q is the flow capacity ($m^3\ h^{-1}$), ρ is the density ($kg\ m^{-3}$), g is gravity ($m\ s^{-2}$), and h is the head (m). For all calculations head height was assumed to be 10 m. The net yield was then calculated by Eq. (35).

$$P_{net} = P_{PV} - P_{pump} \tag{35}$$

Examining Fig. 12, the ideal mass flow rate was found to be dependent on the geometry of the array. For Arrays 1–5 (i.e. $0.11 < AR < 1$), the ideal mass flow rate was identified to be $0.015\ kg\ s^{-1}\ m^{-2}$. Although a lower value of mass flow rate will improve flow distribution, low riser flow rates for arrays with an $AR > 2.25$ will result in high temperature gradients in the direction of flow, reducing PV yield. However as the aspect ratio increases and flow distribution is improved, higher mass flow rates can be employed to improve heat transfer and therefore photovoltaic conversion efficiency. The sharp rise in net yield values for $m = 0.025$, 0.03, 0.035, and $0.04\ kg\ s^{-1}\ m^{-2}$ datasets is attributed to the change from laminar to turbulent flow. By switching to turbulent flow, the Nusselt number for each riser is increased consequently increasing the heat transfer coefficient. These higher flow rates, however, produce poor power yield values as a result of poor flow distribution and higher pump power consumption for arrays of $AR < 1$.

From the results of analysis three (Fig. 12), the net electric yield (P_{net}) from a PV/T array was calculated to be 550.4 W in the best case scenario (Array 9, $m = 0.03\ kg\ s^{-1}\ m^{-2}$, manifold to riser ratio – 4). Comparatively, the yield of a traditional photovoltaic collector operating under the same test conditions was 502.9 W due to its high operating temperature. This value was obtained using the outlined procedure with riser flow rates set to zero. By actively cooling the cells, the net electric yield of the PV/T system was increased by approximately 9.4%.

If the issue of flow distribution was disregarded in the design of a PV/T collector, negligible improvement in PV yield may be obtained. For example, if a 144 cell PV/T array was installed with 36 strings (i.e. Array 1 configuration), a manifold to riser ratio of 1:1 with a fluid flow rate of $0.015\ kg\ s^{-1}\ m^{-2}$, the net yield ($P_{net}$) of the array would be 508.4 W due to the poor flow uniformity within the array. This is only a 1.1% improvement over a traditional PV module.

4. Conclusions

Our investigation has revealed that flow distribution within the header/riser fluid network of a PV/T collector will influence the photovoltaic performance of a series/parallel connected array. Approximately 100 simulations were completed to estimate the effect of flow distribution on photovoltaic yield. Based on the results of this study we have shown that parameters including the manifold to riser pipe ratio, array geometry, manifold flow direction, and mass flow rate to have an influence on flow distribution and therefore photovoltaic conversion. A number of design recommendations are listed below.

1. A manifold to riser pipe ratio of 4:1 is recommended to improve flow distribution. A higher ratio of 6:1 was not found to improve PV yield with the exception of arrays with an aspect ratio less than 0.11. Refer to Fig. 10.
2. The aspect ratio of the array should be greater than 0.44 to improve flow distribution and optimise PV generation.
3. Parallel flow in manifold is generally recommended however reverse flow may be employed for arrays with an aspect ratio greater than one. Refer to Fig. 11.
4. Generally speaking a mass flow rate of 0.015 kg/s m^2 is recommended except for arrays with an aspect ratio greater than 1.78. For values greater than 1.78, higher mass flow rates will increase the net electric yield of the array. Refer to Fig. 12.
5. Work is currently underway to experimentally validate these numerical results at the University of Waikato.

References

Anderson, T.N., Duke, M., Morrison, G.L., Carson, J.K., 2009. Performance of a building integrated photovoltaic/thermal (BIPVT) solar collector. Solar Energy 83, 445–455.

Athienitis, A., Poissant, Y., Collins, M., Liao, L., 2005. Experimental and numerical results for a building-integrated photovoltaic test facility. In: 31st IEEE Photovoltaic Specialists Conference, Lake Buena Vista, Florida, pp. 1718–1721.

Bazilian, M., Prasad, D., 2002. Modelling of a photovoltaic heat recovery system and its role in a design decision support tool for building professionals. Renewable Energy 27, 57–68.

Bludau, W., Onton, A., Heinke, W., 1974. Temperature dependence of the band gap of silicon. Journal of Applied Physics 45 (5).

Carrero, C., Rodriguez, J., Ramirez, D., Platero, C., 2010. Simple estimation of PV modules loss resistances for low error modelling. Renewable Energy, 1103–1108.

Chenni, R., Makhlouf, M., Kerbache, T., Bouzid, A., 2007. A detailed modeling method for photovoltaic cells. Energy 32, 1724–1730.

Chiou, J.P., 1982. The effect of nonuniform fluid flow distribution on the thermal performance of solar collector. Solar Energy 29 (6), 487–502.

Chow, T.T., 2010. A review on photovoltaic/thermal hybrid solar technology. Applied Energy 87, 365–379.

Corless, R.M., Gonnet, G.H., Hare, D.E.G., Jeffery, D.J., Knuth, D.E., 1996. On the Lambert W function. Advances in Computational Mathematics 5, 329–359.

De Soto, W., Klein, S.A., Beckman, W.A., 2006. Improvement and validation of a model for photovoltaic array performance. Solar Energy 80 (1), 78–88.

Duffie, J.A., Beckman, W.A., 2006. Solar Engineering of Thermal Processes. John Wiley & Sons, New Jersey.

Emery, K. et al., 1996. Temperature dependence of photovoltaic cells, modules and systems. In: Proceedings of the 25th IEEE Photovoltaic Specialists Conference, Washington DC, USA, pp. 1275–1278.

Erdil, E., Ilkan, M., Egelioglu, F., 2008. An experiment study on energy generation with photovoltaic (PV)-solar thermal hybrid system. Energy 33, 1241–1245.

Ghani, F., Duke, M., 2011. Numerical determination of parasitic resistances of a solar cell using the Lambert W-function. Solar Energy 85 (9), 2386–2394.

Gnielinski, V., 1976. New equations for heat and mass transfer in turbulent pipe and channel flow. International Chemical Engineering 16, 359–368.

Green, M.A., 1998. Solar Cells Operating Principles. In: Technology and System Applications. University of New South Wales.

Incropera, F.P., DeWitt, D.P., Bergman, T.L., Lavine, A.S., 2006. Fundamentals of Heat and Mass Transfer. John Wiley & Sons, New York.

Jain, A., Kapoor, A., 2004. Exact analytical solutions of the parameters of real solar cells using Lambert W-function. Solar Energy & Materials 81, 269–277.

Jones, G.F., Lior, N.L., 1994. Flow distribution in manifold solar collectors with negligible buoyancy effects. Solar Energy 52 (3), 289–300.

Kays, W.M., Crawford, M.E., 1993. Convective Heat and Mass Transfer. McGraw-Hill, New York.

Lalovic, B., 1986. A hybrid amorphous silicon photovoltaic and thermal solar collector. Solar Cells 19, 131–138.

Naewngerndee, R. et al., 2011. Finite element method for computational fluid dynamics to design photovoltaic thermal (PV/T) system configuration. Solar Energy Materials & Solar Cells 95, 390–393.

Petrone, G., Spagnuolo, G., Vitelli, M., 2007. Analytical model of mismatched photovoltaic fields by means of Lambert W-function. Solar Energy Materials & Solar Cells 91, 1652–1657.

Picault, D., Raison, B., Bacha, S., de la Casa, J., Aguilera, J., 2010. Forecasting photovoltaic array power production subject to mismatch losses. Solar Energy 84, 1301–1309.

Quashning, V., Hanitsch, R., 1996. Numerical simulation of current–voltage characteristics of photovoltaic systems with shaded solar cells. Solar Energy 56 (6), 513–520.

Radziemska, E., Klugmann, E., 1999. Effect of temperature on conversion efficiency of solar module. In: Proceedings of the XXIII IMAPS Conference, Kolobrzeg, Poland.

Radziemska, E., Klugmann, E., 2002. Thermally affected parameters of the current–voltage characteristics of silicon photocell. Energy Conversion and Management 43, 1889–1900.

Santbergen, R., van Zolingen, A.A., 2006. Modeling the thermal absorption factor of photovoltaic/thermal combi-panels. Energy Conversion and Management 47, 3572–3581.

Santbergen, R., Rindt, C.C.M., Zondag, H.A., van Zolingen, A.A., 2010. Detailed analysis of the energy yield of systems with covered sheet-and-tube PVT collectors. Solar Energy 84, 867–878.

Skoplaki, E., Palyvos, J.A., 2009. On the temperature dependence of photovoltaic module electrical performance: a review of efficiency/power correlations. Solar Energy 83, 614–624.

Tripanagnostopoulos, Y., Nousia, T., Soulitios, M., Yianoulis, P., 2002. Hybrid photovoltaic/thermal solar systems. Solar Energy 72, 217–234.

van Helden, W.G.J., van Zolingen, A.A., Zondag, H.A., 2004. PV thermal systems: PV panels supplying renewable electricity and heat. Progress in Photovoltaics: Research and Applications 12, 415–426.

Villalva, M.G., Gazoli, J.R., Filho, E.R., 2009. Comprehensive approach to modeling and simulation of photovoltaic arrays. IEEE Transactions on Power Electronics 24 (5), 1198–1208.

Wang, S.A., Wu, L.G., 1990. Analysis and performance of flat-plate solar collector arrays. Solar Energy 45 (2), 71–78.

Whillier, A., 1953. Solar Energy Collection and its Utilisation for House Heating. Thesis. MIT, Cambridge, MA.

Whillier, A., 1977. Prediction of performance of solar collectors. In: Jordan, R.C., Liu, B.Y.H. (Eds.), Applications of Solar Energy for Heating and Cooling of Buildings. ASHRAE, New York.

Wysocki, J., Rappaport, P., 1959. Effect of temperature on photovoltaic solar energy conversion. Journal of Applied Physics 31 (3), 571–578.

Zondag, H.A., Vries, D.W., Van Steenhoven, A.A., Zolingen, R.J.C., 2002. The thermal and electrical yield of a PV-thermal collector. Solar Energy 72 (2), 113–128.

Zondag, H.A., Vries, D.W., Van Hendel, W.G.J., Van Zolingen, A.A., Van Steenhoven, A.A., 2003. The yield of different combined PV-thermal collector designs. Solar Energy 74, 253–269.

Chapter 8: Estimation of photovoltaic conversion efficiency of a building integrated photovoltaic/thermal (BIPVT) collector array using an artificial neural network

8.0 Introduction

The research goal of this thesis was to develop a model of a BIPVT collector which could be utilised to assess the effect of flow distribution on photovoltaic yield. This objective was met in the Chapter 7; however it could not be used by non-technical personnel. Research presented here has shown that a simpler method can be implemented to ensure the effect of flow distribution can be practically considered by the manufacturer of building integrated solar technology.

The feed forward multi-layer perceptron neural network was trained in this work using the back propagation learning algorithm in Matlab. Training data was obtained using the method presented in Chapter 7. It was found in this work that a neural network can be adequately trained to learn the relationship between the specified inputs and desired outputs. Once trained the neural network is fast and simple to use and has the ability to interpolate values within the original training set. This permits the effects of flow distribution to be factored into the calculation of photovoltaic output for a BIPVT installation with minimal complexity.

8.1 Journal paper: Estimation of photovoltaic conversion efficiency of a building integrated photovoltaic/thermal (BIPVT) collector array using an artificial neural network

Available online at www.sciencedirect.com
SciVerse ScienceDirect
Solar Energy 86 (2012) 3378–3387
SOLAR ENERGY
www.elsevier.com/locate/solener

Estimation of photovoltaic conversion efficiency of a building integrated photovoltaic/thermal (BIPV/T) collector array using an artificial neural network

F. Ghani *, M. Duke, J.K. Carson

Department of Engineering, Waikato University, Hamilton 3240, New Zealand

Received 26 March 2012; received in revised form 29 July 2012; accepted 3 September 2012

Communicated by: Associate Editor Brian Norton

Abstract

Earlier studies have shown that the thermal efficiency of a solar thermal collector is influenced by the quality of coolant flow distribution within the array. The quality of flow distribution within a header/riser type fluid network is influenced by a number of parameters including the coolant mass flow rate, the direction of flow in the manifolds, and most importantly the geometry of the array. As a building integrated photovoltaic thermal (BIPVT) collector will be a made to measure product, meaning its dimensions will be dictated by the specific roofing and energy requirements of the customer, the issue of flow distribution and its effect on both thermal and photovoltaic performance raises some concern. In order to quantify the detrimental effect flow distribution may have on the photovoltaic output of a BIPVT array, a numerical approach was presented by authors in earlier work where factors known to influence flow distribution were varied. The authors demonstrated that photovoltaic output may be severely hindered if the issue of flow distribution is not adequately addressed. In this new study we use this numerical method to additionally show that photovoltaic output is not always improved by reducing the fin width W (by increasing the number of risers for each module) despite the theoretical rise in fin efficiency F as a consequence of flow distribution. Under certain scenarios it was shown that a single riser will in fact improve PV output and also reduce system installation cost and complexity. The combination of these new finding and results previously obtained by the authors highlights the need in selecting the optimal design parameters to meet the specific requirements of each installation. The numerical approach carried out to calculate PV output however was time consuming and computationally intensive and therefore not feasible to perform for each and every customer. To address this issue, the authors have proposed in this paper to train an artificial neural network which can be used to approximate the photovoltaic yield of an array of specified shape operating under parallel\reverse flow in the manifolds and also with one or two fluid channels cooling each string of cells. By approximating the yield for each scenario, the optimal configuration can then be chosen. It was found that the neural network can be successfully trained for this specific application offering a fast alternative to the original numerical approach.

Keywords: Flow distribution; Photovoltaic; Thermal; Artificial neural network; Building integrated; Solar thermal

1. Introduction

As a result of growing concern for the environment regarding the effect of greenhouse gas emissions, human kind is actively seeking an alternative to fossil fuel based energy generation. Of all the renewable energy technologies which exist today, solar energy has greatest potential in meeting our growing energy needs since it is an abundant and essentially inexhaustible supply of energy. It has been stated elsewhere that in a single hour, the total irradiation received on earth from the sun is sufficient in meeting the

* Corresponding author. Tel.: 1 64 7 838 4522.
E-mail address: fag2@waikato.ac.nz (F. Ghani).

0038-092X/$ - see front matter © 2012 Elsevier Ltd. All rights reserved.
http://dx.doi.org/10.1016/j.solener.2012.09.001

global energy needs for an entire year (Lewis and Nocera, 2006).

At present, solar energy is harnessed by the conversion of incidental radiation into thermal and electrical energy via solar thermal and photovoltaic collector technologies respectively. The former technique is concerned with the conversion of solar energy into heat via an absorption process typically within an absorber made from a material of high thermal conductivity such as aluminium or copper. Fluid is circulated through channels bonded to the absorber in order to transport heat away from the absorber to a storage vessel were it is then typically used for domestic hot water and space heating purposes. The photovoltaic collector on the other hand is a solid state device which can convert solar radiation into electricity directly (Green, 1998). In one study it was stated that the residential building sector comprises of 38% space heating, 30% electricity, and 27% water heating by end use in Australia (Bazilian et al., 2002) making clear that both collector types would be useful in assisting our energy needs.

Despite the technological and environmental advantages attached to the use of solar collectors, their widespread adoption is hindered by economic factors. The high manufacturing and installation costs attached to these technologies make their purchase generally feasible only where government assistance is offered. In order to reduce the overall cost of these systems, the integration of photovoltaics directly onto buildings has been adopted where traditional building materials are replaced with solar energy conversion materials. By removing material, manufacturing, and installation redundancies, the cost of implementation can be reduced. However, the integration of photovoltaics into a building can lead to reduced ventilation of the photovoltaic cells and therefore elevated operating temperatures. For example cell temperatures 20 °C above the normal operating temperature were predicted in one study as a result of the integration of photovoltaics directly onto the building (Davis et al., 2001).

The detrimental effect of temperature on the performance of a photovoltaic cell, particularly those which are silicon based is well documented (Arora and Hauser, 1982; Emery et al., 1996; Green, 2003; Radziemska and Klugmann, 2002; Skoplaki and Palyvos, 2009). In summary, a reduction in bandgap with rising temperature (Bludau et al., 1974) yields a marginal increase in the short circuit current due to the additional photons which can penetrate the material and generate charge carriers. However the rise in reverse saturation current with temperature results in a linear drop in open circuit voltage. The net effect is a drop in photovoltaic conversion efficiency proportional to the temperature rise typically calculated using Eq. (1) (Evans, 1981).

$$\eta_c = \eta_{T_{ref}}[1 - \beta_{ref}(T_c - T_{ref})] \quad (1)$$

where η_{Tref} and β_{ref} are values typically provided by the manufacturer, T_c the actual cell temperature, and T_{ref} is the reference temperature of that cell. An extensive review of power and efficiency correlations is provided in other work (Skoplaki and Palyvos, 2009).

The operating temperature of the photovoltaic panel and its negative effects can be reduced by circulating fluid (for example air or water) in such a way that it provides a cooling effect. In addition to the electrical performance improvement of the PV panel, thermal energy transported from the cells can be captured and utilised for space heating and water heating by implementing an active heat recovery system. Such a system can dramatically improve the energy yield of the collector. An experimental study conducted by Athienitis et al. (2005) demonstrated that the combined efficiency (photovoltaic and thermal) can be as high as 70%. The combination of low modification cost and improved energy yield of the hybrid collector together has significant economic potential. For instance, the payback period for the hybrid modification was shown to be less than 2 years in one study (Erdil et al., 2008). In another study TRNSYS simulations were carried out which demonstrated the reduced payback period of the hybrid collector over traditional collector technology (Kalogirou and Tripanagnostopoulos, 2006).

But despite these advantages, a number of technical issues remain to be addressed to ensure the adoption and market penetration of this technology. In one study, three parameters were investigated; the packing factor, the water flow rate, and the pipe size of fluid channels on system performance (Ji et al., 2006). However the modified Hottel–Whillier analysis carried out for the heat transfer analysis in this study assumed that coolant flowed uniformly within the absorber. Several studies (to be discussed in the next section) have revealed that this assumption is not valid for most practical installations. The authors are currently investigating the influence of flow mal-distribution within the PV/T absorber and its influence on photovoltaic performance.

1.1. Flow distribution within a solar collector

The typical flat plate solar thermal collector utilises a fluid network system similar to the one shown in Fig. 1. Commonly referred to as a header/riser or manifold/riser array, this network consists of an inlet manifold which supplies the network with coolant fluid, a series of fluid risers which branch from the inlet manifold to collect heat from the absorber, and a discharge manifold which collects the heated fluid. The heat transfer analysis of a traditional solar thermal collector as stated by Duffie and Beckman (Duffie and Beckman, 2006) assumes that the fluid flow within such a network to be uniform such that,

$$m_1 = m_2 = m_2 \cdots = m_{N_{riser}} \quad (2)$$

where m is the riser mass flow rate (kg s^{-1}) and N_{riser} is the number of fluid risers of the header/riser network. However several studies have revealed that this assumption is not valid for most practical installations and that thermal efficiency decreases as flow uniformity within the array diminishes.

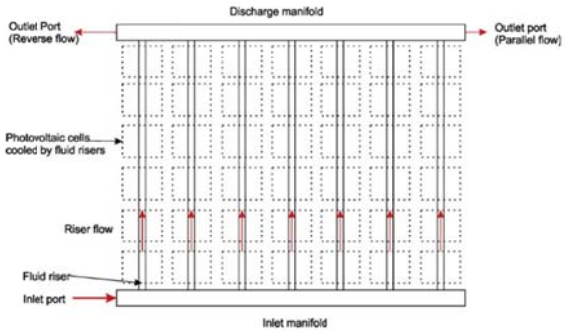

Fig. 1. The header/riser fluid network and photovoltaic connection scheme. Cells are connected in series along the fluid risers and connected in parallel with the next string of cells.

A two dimensional numerical analysis was conducted in one early study in order to investigate the issue of flow distribution within a flat plate solar collector (Chiou, 1982). Examining a total of 16 artificially assumed models, thermal efficiency of the collector was found to deteriorate between 2% and 20% due to the elevated absorber temperature in areas of poor flow.

Wang and Wu (1990) carried out a combined numerical and experimental study to investigate the effect of flow uniformity within a large 16 collector array. Their experiment looked into what effect the direction of flow in the manifolds will have on the flow distribution and thermal performance on the solar thermal array. Two levels were investigated; (i) parallel flow or *Z*-type array and (ii) reverse flow or *U*-type array (see Fig. 1). Their numerical results which were experimentally confirmed revealed a large change in the flow distribution pattern was obtained by changing the flow direction in the manifolds. For the case of parallel flow, flow was measured to be the greatest at the ends of the array with a sharp drop for central risers. Thermal efficiency for the first and last collectors of the array under these conditions was approximately 80% however the mean thermal efficiency for the total array was only 58.5%. The temperature of the riser or branch pipes varied between approximately 20 °C near the ends to over 50 °C at the array centre. For reverse manifold flow, the pattern of flow within the risers was found to vary significantly from the previous scenario with flow progressively dropping from the riser closest to the inlet port to the furthest location. In this case, thermal efficiency was found to drop from over 80% near the inlet port, to an average of only 44.5%. Based on these results, the authors suggest avoiding reverse flow in the manifolds.

Another numerical study investigated the effect of several parameters and their effect on flow distribution on the performance of a solar thermal collector (Jones and Lior, 1994). In this study 54 treatment combinations were looked at varying the following parameters: (i) the ratio of riser to manifold diameters, (ii) the number of risers, (iii) the distance between risers, (iv) the ratio of the riser length to riser diameter, and (v) the direction of flow in the manifold. The ratio of the riser to manifold pipe diameters was identified to be the most influential parameter on flow mal-distribution followed by the number of risers (N_{riser}) with flow uniformity deteriorating in proportion to N_{riser}^2. Additionally it was found that by reducing the length of the fluid risers flow uniformity was worsened. This study revealed that the shape of the fluid network (i.e. the number and length of risers) will have a strong influence on the thermal performance of a solar thermal collector.

Research into the effects of flow uniformity within a header/riser type array have until recently been primarily focused on traditional solar thermal technology only. These studies discussed so far have all revealed that a large variation in absorber temperature is possible due to the flow distribution phenomenon and that the performance of photovoltaic devices is strongly dependent on temperature. Only recently has this effect on a PVT collector been looked at.

An investigation was made which looked at what effect the distribution of flow it will have on a PVT collector (Naewngerndee et al., 2011). This study came to the conclusion that by decreasing mass flow rate, flow uniformity can be improved. Furthermore the shape of the array was found to also have an impact. However this work did not report on what effect this will have on the photovoltaic yield.

1.2. The effect of flow distribution on photovoltaic yield in a PVT collector

In previous work (Ghani et al., 2012) the authors investigated the influence of flow distribution on the photovoltaic yield of a PVT collector using a numerical approach. The authors found that the parameters which influence flow distribution and therefore the thermal performance

of a solar thermal collector will similarly affect the photovoltaic yield of a PVT collector. Interestingly, this study revealed that a correlation exists between the quality of flow distribution and the geometry of the array. We find this result interesting as the building integrated PVT collector will be built to suit the unique requirements of the customer and therefore its dimensions will be highly variable as opposed to the solar thermal collector which is traditionally manufactured to fixed dimensions, (i.e. its length and width remains constant). This will make it difficult to predict the flow distribution characteristics and photovoltaic output for a BIPVT collector.

An example of what a BIPVT array may look like is shown in Fig. 2. The length and number of modules placed alongside each other will depend on the requirements of the customer. For our investigation we make the assumption that the array shown in Fig. 2 is electrically connected in such a way that each cell of a BIPVT collector module is connected in series. Each adjacent module is then connected in parallel to form the array. The size of the fluid array is therefore proportional to the size of the PV array such that,

$$N_{riser} \propto N_p \tag{3}$$

$$L_{risers} \propto N_s \tag{4}$$

where N_p is the number of parallel strings, N_s the number of series connected cells and L_{risers} is the length of the BIPVT collector module.

In order to investigate the issue of array geometry, nine arrays were examined by Ghani et al. each of which consisted of a total of 144 cells. The characteristics of each of the nine arrays are given in Table 1. The arrays were created by altering the number of cells connected in series and in parallel thus adjusting the shape of the array as per our assumption while maintaining a total of 144 cells. Referring to Table 1, the aspect ratio or AR value for each array is used to quantify the array shape. It is calculated by dividing the number of cells connected in series (N_s) with the number of cells connected in parallel (N_p). Therefore an array with an AR value of less than 1 (such as Arrays 1 through to 4) is greater in width than in length (in the direction of fluid flow) and vice-versa.

Table 1
Array geometries investigated in previous work (Ghani et al., 2012). An AR value <1 represents an array which is short (in direction of fluid flow) and wide in width, while an AR value >1 represents and array which is long (in direction of fluid flow) and narrow in width.

Array	N_s	N_p	AR
1	4	36	0.11
2	6	24	0.25
3	8	18	0.44
4	9	16	0.56
5	12	12	1.00
6	16	9	1.78
7	18	8	2.25
8	24	6	4.00
9	36	4	9.00

In addition to the effects of array geometry other parameters were also investigated by Ghani et al. including the effect of mass flow rate and the direction of flow within the manifolds of the array (see Fig. 1). Naewngerndee et al. showed that flow uniformity would in fact improve by reducing the mass flow rate. However, by reducing the mass flow rate, we can expect a larger temperature rise in the working fluid and therefore a higher photovoltaic array operating temperature and reduced electric output. These effects must be balanced. Fig. 3 presents the effect of mass flow rate on the net yield ($P_{net} = P_{PV} - P_{pump}$) of the BIPVT collector for each of the arrays listed in Table 1. From a quick inspection we can see that the mass flow rate and the array geometries will have an effect on the net yield of an array. Taking a closer look at Fig. 3, the array operating with a mass flow rate of $m = 0.005\ \mathrm{kg\,s^{-1}\,m^2}$ offers a slight improvement in net yield over an array operating at $m = 0.035\ \mathrm{kg\,s^{-1}\,m^2}$ for Arrays 2–6 which we can attribute to the improvement in flow distribution. However as the aspect ratio increases going from Arrays 6 to 9, flow distribution is improved making the higher mass flow rate beneficial due to the improved heat transfer. The large jumps we see for $m = 0.025\ \mathrm{kg\,s^{-1}\,m^2}$ and $0.035\ \mathrm{kg\,s^{-1}\,m^2}$ is due to a switch from laminar heat transfer to turbulent heat transfer (see Ghani et al. for details). This figure demon-

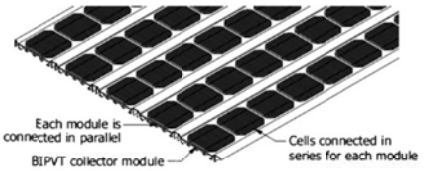

Fig. 2. Example installation of a BIPVT array. The length and number of modules may be varied to suit the requirements of the customer. The number of cells connected in series for each module dictated the length of the module. Each module was connected in parallel to form the array.

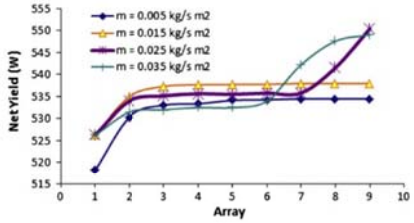

Fig. 3. Effect of mass flow rate on the net yield of BIPVT array (Ghani et al., 2012).

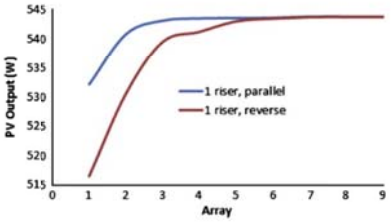

Fig. 4. Effect of flow direction in the manifolds on the photovoltaic yield of a BIPVT array (Ghani et al., 2012).

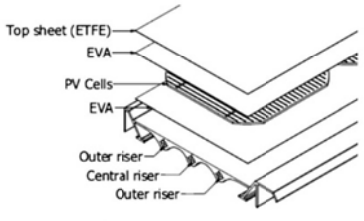

Fig. 5. Design of BIPV/T collector under investigation. Photovoltaic cells are vacuum laminated directly onto the aluminium extrusion using EVA and a top sheet. For the single riser setup, only the 'central riser' is used while for two risers the two 'outer riser' channels are only used.

strates that the ideal mass flow rate is dependent on the aspect ratio of the array.

As identified by Wang and Wu, the direction of flow through the manifolds will have an impact on the flow distribution and thermal performance of a traditional solar thermal collector. Fig. 4 plots the photovoltaic output for each of the nine arrays operating under both parallel and reverse flow in the manifolds. We observe that a reduced photovoltaic yield is obtained for Arrays 1–5 operating under reverse flow. However for Array 6 onwards, the improved flow characteristics associated with the high aspect ratio results in convergence of the two data sets. This result may be beneficial as during the installation of a BIPVT array, it may be more convenient for the installer to install the array operating with reverse manifolds flow. However under certain circumstance as indicated by Fig. 4 this should be avoided.

1.2.1. Effect of fin width W

The concept design of an unglazed BIPVT collector under investigation in this work is shown in Fig. 5. Photovoltaic cells are vacuum laminated directly onto the aluminium extruded absorber using multiple ethylene-vinyl-acetate (EVA) sheets and a single top cover sheet. An exploded assembly drawing is shown in Fig. 5 which provides the location of the constituent layers of the sandwich assembly. The irreversible lamination process occurs at 150 °C in a vacuum laminator whereby the copolymer EVA "cures" sealing the photovoltaic cells in order to prevent the ingress of moisture (Krauter, 2006). The process is performed in a vacuum chamber so that air is expelled from the assembly. This is not only important from an aesthetic perspective (i.e. to remove bubbles) but also for heat transfer. Thermal resistance between the PV cells and the aluminium absorber underneath it is minimised by the evacuation of air from the assembly.

The absorber shown in Fig. 5 is an aluminium extrusion which consists of three fluid risers to cool the absorber however during installation not all fluid risers need to be utilised raising the question of how many fluid risers should be used. Theoretically, by increasing the number of fluid channels of diameter D, we reduce the fin width (W) thereby improving the fin efficiency F (and heat transfer) as calculated using Eq. (5) (Duffie and Beckman, 2006).

$$F = \frac{\tan h[m(W-d)/2]}{m(W-D)/2} \tag{5}$$

However as discussed in the previous section, the issue of flow distribution should be considered for any practical installation. By increasing the number of fluid risers for certain array geometries, the flow distribution may be so poor that the photovoltaic yield may actually be reduced. Moreover the cost of the system, in terms of both material and labour, is increased by plumbing the extra risers. One of the objectives of this study is to identify the case were the two riser design will in fact reduce the PV output over the single riser design.

To answer this question the method outlined previously by the authors (Ghani et al., 2012) was implemented for the nine arrays listed in Table 1. This time however, both one and two risers were additionally investigated. Several mass flow rates (see Table 2) were investigated as we have shown this will have some impact on the flow distribution within the array. Parameters used for the analysis are given in Table 2 and characteristics of the solar cell used for the photovoltaic calculation is listed in Table 3. Series and shunt resistance values listed in Table 2 were calculated for the cell using the method of Ghani and Duke (2011).

Although any solar collector is expected to operate under a wide variety of irradiance levels, our investigation was carried out at only 1000 W/m^2 as this value corresponds to standard test conditions (STCs) typically used for photovoltaic rating. We therefore also made the assumption that the ambient temperature was 25 °C consistent with these test conditions.

Figs. 6 and 7 present the results of the photovoltaic analysis performed on a BIPVT collector. Fig. 6 plots the results for Arrays 1–9 operating with both one and two fluid channels, parallel and reverse flow in the manifolds at a coolant mass flow rate of 0.015 kg s^{-1} m^2. From these results we can see that for Arrays 1 and 2 (the low aspect ratio arrays) the use of two fluid channels is detrimental to the photovoltaic yield. From Array 3 onwards however, the improved fin efficiency and flow distribution results in

Table 2
Input parameters for analysis.

	Symbol	Value	Units
Manifold diameter	$\Phi_{manifold}$	40	mm
Fluid riser diameter	Φ_{risers}	10	mm
Number of covers	–	0	–
Fin width	W	160, 80	mm
Overall heat loss coefficient, (Anderson, 2009)	U_L	22	W/m^2 K
System flow rate	m	0.005, 0.015, 0.02, 0.025, 0.35, 0.04	kg s^{-1} m^{-2}
Absorber thickness	δ	2	mm
Absorber thermal conductivity	k_{abs}	190	W/m k
PV cell thermal conductivity, (Krauter, 2006)	k_{PV}	130	W/m k
Absorption coefficient, (De Vries, 1998)	α_{PV}	0.74	–
Ambient temperature	T_{amb}	25	°C
Fluid inlet temperature	$T_{fluid,inlet}$	20	°C
Irradiance	G	1000	W/m^2
Number of cells in series	N_s	Refer to Table 1	–
Number of cells in parallel	N_p	Refer to Table 1	–

Table 3
Characteristics of solar cells used for the PV analysis.

Short circuit current	I_{sc}	8.41	A
Open circuit voltage	V_{oc}	0.613	V
Current at MPP	I_{mp}	7.92	A
Voltage at MPP	V_{mp}	0.495	V
Diode constant (Carrero et al., 2010)	n	1	–
Series resistance (Ghani and Duke, 2011)	R_s	0.0054	Ω
Shunt resistance (Ghani and Duke, 2011)	R_{sh}	12.73	Ω

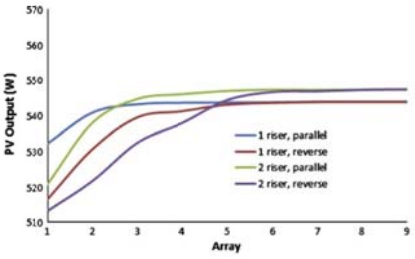

Fig. 6. Photovoltaic yield for Arrays 1–9 operating under $m = 0.015$ kg s^{-1} m^2 of flow.

an improvement in PV output from the array. With respect to parallel and reverse flow in the manifolds, we can see that the PV output eventually converges for both directions from Array 6 onwards regardless of how many fluid channels are used. For Arrays 1–5 however, parallel flow in the manifold is preferred based on the improvement in PV yield.

Fig. 7 presents the results of our analysis at $m = 0.04$ kg s^{-1} m^2. The pattern in comparison to Fig. 6

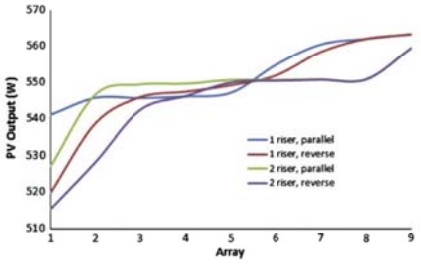

Fig. 7. Photovoltaic yield for Arrays 1–9 operating under $m = 0.04$ kg s^{-1} m^2 of flow.

is quite different due to the variation in flow distribution quality and the switch made from laminar to turbulent heat transfer for the array geometries of high aspect ratio. Here we can see that two fluid channels optimises PV yield for Arrays 2–5. For Array 1, a single fluid channel operating under parallel flow is preferred. Interestingly, from Array 6 onwards, the single fluid riser optimises PV output due to the switch from laminar to fully developed turbulent heat transfer. This occurs as the flow rate (and therefore velocity) for each fluid channel is higher with less fluid channels increasing the Reynolds number $Re_D > 3000$ into the fully developed Turbulent flow region. These results demonstrate that the photovoltaic output will be a function of array geometry, manifold flow direction, mass flow rate and finally the number of fluid channels used to cool the PVT module.

Based on the results so far, we begin to understand the unique requirements of the building integrated PVT collector and how flow distribution will affect its photovoltaic output. The custom nature of this technology whereby the collector is sized to meet the specific requirements of the customers roofing and energy needs means that a method to determine the optimal combination of mass flow rate, number of fluid channels, and the flow direction in the manifolds would be beneficial. The method used for the work so far however was time consuming and computationally intensive and therefore cannot be practically implemented for commercial purposes. In an attempt to address this issue, the authors have investigated the use of an artificial neural network to develop a tool which may be easily and quickly used to assist the installer in selecting the optimal design.

2. The artificial neural network

In this section we discuss the development of an artificial neural network trained using the numerical data acquired in the previous section. The aim is to develop a simple and fast tool which will assist the installer of a BIPVT system in selecting the optimal mass flow rate, the number of fluid channels to utilise, and the direction of flow in the

manifolds in order to maximise the photovoltaic output. The next section will give a brief introduction into the theory of the artificial neural network.

2.1. Background in the artificial neural network

Artificial neural networks (ANNs) are computational models which replicate the function of a biological network, composed of neurons and are used to solve complex functions in various applications such as control, data compression, forecasting, optimisation, pattern recognition, classification, speech, and vision (Sözen et al., 2008). More recently, however, is the application of ANNs to energy systems (Kalogirou, 1999, 2000; Kalogirou and Panteliou, 2000).

The commonly used feed-forward, multi-layer perceptron (MLP) ANN architecture has been successfully applied to a number of solar thermal (Farkas and Geczy-Vig, 2003; Kalogirou and Panteliou, 2000; Kalogirou et al., 1999) and photovoltaic applications (Ashhab, 2008; Izgi et al., 2012; Karatepe et al., 2006; Mellit and Kalogirou, 2008). This architecture typically consists of three layers; an input layer, the hidden layer, and the output layer. Inputs are presented to the neural network via the input layer were they are then processed in the hidden layer. The neural network output is calculated in the final output layer. Neurons located in both the hidden and output layers possess an activation function. The sigmoid non-linear activation function is commonly used and produces an output between 0 and 1.

A critical step in applying an artificial neural network to an application is the training stage. Here training data which consists of input vectors and the corresponding output vectors are presented to the network. The initial weights and bias values originally selected at random are then adjusted according to a training algorithm so the output of the ANN matches the output of the training data. Once a satisfactory level of performance is achieved by the network, training is stopped and the final weights and bias values are used permanently by the network.

The back-propagation algorithm is commonly employed for the training of the multi-layer perceptron neural network. The objective of this algorithm is to minimise the global error such as the mean% error, mean square error (MSE), and R^2 (Sözen et al., 2008). The mean square error calculated using Eq. (6) was used in our study.

$$MSE = \frac{1}{N}\sum_{N}^{1=1}(t_i - a_i)^2 \tag{6}$$

where t_i is the target output and a_i is the actual output from the network.

The error is calculated by comparing the output from the network with the output value from the training data. Weights are then adjusted by propagating the error from the output layer back to the input layer. This iterative process is repeated until the network has learnt the pattern of the training data.

2.2. Design of an ANN for BIPV/T application

An artificial neural network was developed to approximate the photovoltaic output of a BIPV/T array using the Matlab™ Neural Network toolbox. The purpose of the network was to approximate PV yield of a BIPV/T array operating under various modes of operation for a specified array shape (aspect ratio) and mass flow rate. The feed forward MLP architecture chosen for this problem is shown by Fig. 8.

Two input neurons, nine hidden layer neurons and four output layer neurons were used in total for our artificial neural network. The inputs in the network are the arrays aspect ratio and mass flow rate. The outputs of the network are the approximate PV yield (in Watts) with the BIPV/T array operating under four fluid flow configurations; (a) single riser, parallel flow, (b) single riser, reverse flow (c) double riser, parallel flow, and (d) double riser, reverse flow.

Although the reverse flow in manifolds generally yields reduced PV output due to the poor flow characteristics (Ghani et al., 2012), there may be instances where the installation of the array may be simplified and/or cost effective by this type of installation. Output from this scheme is therefore included. Data for training the network was obtained by conducting 288 numerical simulations using the method outlined by Ghani et al. Examining the architecture of the neural network, we can see that for each aspect ratio and mass flow rate input pair, we obtain four outputs.

The network shown in Fig. 8 was trained using the using the Levenberg-Marquardt back-propagation algorithm (Beale et al., 2012). Network training data is usually split three ways for the training process. For our study the data collected from the 288 simulations was split 70/15/15 into three subsets; training, validation, and testing respectively. The majority of data is allocated to training the network in order to adjust synaptic weights and biases. The validation data set is used to overcome overtraining of the network, when the network loses its ability to generalise due to over fitting. During the training process validation error is calculated with training error after each training epoch. Overtraining is identified when training error is reduced but validation error rises. If the validation error continues to rise for a specified number of epochs, the training is stopped (Caner et al., 2011). The final portion of training data is then used to test the trained network. Input vectors which have not been previously encountered during the training phase are presented to the network. The network output is compared with the desired output. If the error is acceptable, the training is stopped, otherwise the training process is repeated and the weights readjusted.

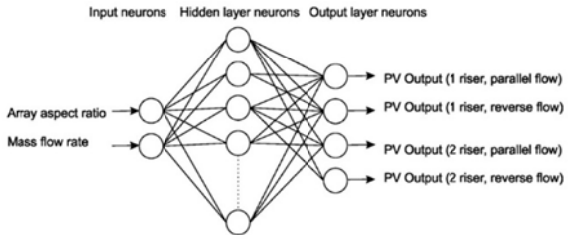

Fig. 8. Feed forward, multi-layer perceptron neural network architecture used in our investigation.

3. Training results and discussion

Results of training the ANN are shown in Fig. 9. In this figure, regression values are plotted for the training, validation, and testing stages and additionally the total training response. The regression plots show the relationship between the outputs of the network and the target values. The dashed line represents the ideal result where the network output equals the target or desired value. The solid coloured line represents the best fit linear regression line between the output and the target. Ideally the coloured line will superimpose the dashed line.

As the minimum R value obtained from training the network was 0.979 and 0.984 for total training, a close relationship between the network and target outputs was achieved. The best fit regression lines for all three stages (training, validation, and testing) shown by the coloured lines closely match the dotted lines indicating a strong correlation between network outputs and targets had been achieved.

The results obtained indicate that an artificial neural network can be successfully trained for approximating the photovoltaic output from a BIPV/T array of various shape and mass flow rate operating under several fluid flow

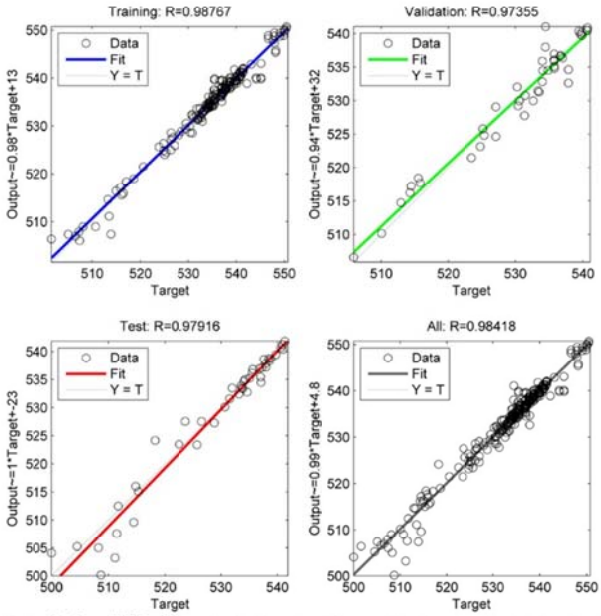

Fig. 9. Results from ANN training using the Levenberg Marquardt back-propagation training algorithm.

configurations. Once trained, the artificial neural network can be used to answer the following questions for an array of specified aspect ratio:

(1) How many fluid risers should be used?
(2) What is the optimal mass flow rate?
(3) Should parallel or reverse flow in the manifolds be used?

Once trained, the output of the neural network is quickly calculated which is the primary advantage over performing the three step numerical process proposed by the authors in earlier work (Ghani et al., 2012). The process of calculating array yield for the four connection schemes is reduced from several hours to less than a second. Although training of the neural network is a time consuming process, the neural network has the additional advantage that it can be used to interpolate values within the original training set. For example, during training the following mass flow rate values were used; 0.005, 0.01, 0.015, 0.02, 0.025, 0.03, 0.035, 0.04 $kgs^{-1} m^2$. Once trained the network could be used to determine the array output for $m = 0.018$ for $kgs^{-1} m^2$ example. This could similarly be applied for the aspect ratio value. Therefore a neural network that has been trained from a discrete number of training sets can be applied to solve for inputs over a continuous domain provided it is within the boundaries of the training data.

4. Conclusions

In this work, the effect of flow distribution on the photovoltaic yield of an unglazed BIPV/T collector has been discussed. Results of a numerical investigation have been presented which displays the variation in photovoltaic output due to the changes in the manifold to riser ratio, the mass flow rate, the direction of flow in the manifolds, and by the shape of the array as a consequence of coolant flow distribution. As the size of a BIPV/T array (and therefore fluid network) will inevitably vary from customer to customer, the behaviour of the fluid cooling the photovoltaic system will similarly vary making photovoltaic yield difficult to predict. Additionally in this study we have demonstrated that by reducing the fin width we do not always improve the photovoltaic output. Cases have been identified were the single riser will in fact improve PV yield due to the more favourable flow distribution conditions. A three step numerical process proposed by the authors in earlier work was used to approximate this value for different geometries but it was computationally intensive and time consuming to carry out. In this study, an artificial neural network was successfully trained so that it can be used to approximate the PV yield for a BIPV/T array of specific aspect ratio and mass flow rate operating under several flow connection schemes. Similar to the standard test conditions typically used for the rating of photovoltaic systems, our investigation was carried out under fixed conditions. Therefore the effects of wind, varying irradiance, and temperature were not considered. Results of the training process indicate that a neural network is able to learn the underlying relationship between the inputs and the outputs for this specific application. The trained network can be used as a useful tool for the installer of BIPVT arrays in selecting the optimal array parameters.

The primary disadvantage of this method however is the initial collection of data used for network training which was obtained by running numerous numerical simulations which was time consuming and computationally intensive. Once trained however, the network is fast and can be used to interpolate values over a continuous domain within the limits of the training data set. The application discussed in this work is however only concerned with the photovoltaic yield of the BIPV/T collector.

References

Anderson, T.N., 2009. Investigation of thermal aspects of building integrated photovoltaic/thermal solar collectors. In: Science & Engineering, Hamilton: Waikato University.

Arora, N.D., Hauser, J.R., 1982. Temperature dependence of silicon solar cell characteristics. Solar Energy Materials 6, 151–158.

Ashhab, M.S.S., 2008. Optimization and modeling of a photovoltaic solar integrated system by neural networks. Energy Conversion and Management 49, 3349–3355.

Athienitis, A., Poissant, Y., Collins, M., Liao, L., 2005. Experimental and numerical results for a building-integrated photovoltaic test facility. In: Presented at the 31st IEEE Photovoltaic Specialists Conference, 3–7 January, Lake Buena Vista, Florida.

Bazilian, M., Kamalanathan, H., Prasad, D.K., 2002. Thermographic analysis of a building integrated photovoltaic system. Renewable Energy 26, 449–461.

Beale, M.H., Hagan, M.T., Demuth, H.B., 2012. Neural Network Toolbox User's Guide, The Mathworks, Inc.

Bludau, W., Onton, A., Heinke, W., 1974. Temperature dependence of the band gap of silicon. Journal of Applied Physics, 45.

Carrero, C., Rodriguez, J., Ramirez, D., Platero, C., 2010. Simple estimation of PV modules loss resistances for low error modelling. Renewable Energy, 1103–1108.

Caner, M., Gedik, E., Kecebas, A., 2011. Investigation on thermal performance calculation of two type solar air collectors using artificial neural network. Expert Systems with Applications 38, 1668–1674.

Chiou, J.P., 1982. The effect of nonuniform fluid flow distribution on the thermal performance of solar collector. Solar Energy 29, 487–502.

Davis, M.W., GFanney, A.H., Dougherty, B.P., 2001. Prediction of building integrated photovoltaic cell temperatures. Journal of Solar Energy Engineering 123, 200–210.

De Vries, D.W., 1998. Design of a photovoltaic/thermal combi-panel, PhD report: EUT.

Duffie, J.A., Beckman, W.A., 2006. Solar engineering of thermal processes, third ed. John Wiley & Sons, New Jersey.

Emery, K. et al., 1996. Temperature dependence of photovoltaic cells, modules and systems. In: Presented at the Proceedings of the 25th IEEE Photovoltaic Specialists Conference, Washington DC, USA.

Erdil, E., Ilkan, M., Egelioglu, F., 2008. An experiment study on energy generation with photovoltaic (PV)-solar thermal hybrid system. Energy 33, 1241–1245.

Evans, D.L., 1981. Simplified method for predicting photovoltaic array output. Solar Energy 27, 555–560.

Farkas, I., Geczy-Vig, P., 2003. Neural network modelling of flat-plate collectors. Computers and Electronics in Agriculture 40, 87–102.

Ghani, F., Duke, M., 2011. Numerical determination of parasitic resistances of a solar cell using the Lambert W-function. Solar Energy 85, 2386–2394.

Ghani, F., Duke, M., Carson, J.K., 2012. Effect of flow distribution on the photovoltaic performance of a building integrated photovoltaic/thermal (BIPV/T) collector. Solar Energy 86, 1518–1530.

Green MA, 1998. Solar Cells Operating Principles, Technology and System Applications. University of New South Wales.

Green, M.A., 2003. General temperature dependence of solar cell performance and implications for device modelling. Progress in Photovoltaics: Research and Applications 11, 333–340.

Izgi, E., Oztopal, A., Yerli, B., Kaymak, M.K., Sahin, A.D., 2012. Short–mid-term solar power prediction by using artificial neural networks. Solar Energy 86, 725–733.

Ji, J. et al., 2006. Effect of fluid flow and packing factor on energy performance of a wal- mounted hybrid photovoltaic/water-heating collector system. Energy and Buildings 38, 1380–1387.

Jones, G.F., Lior, N.L., 1994. Flow distribution in manifold solar collectors with negligible buoyancy effects. Solar Energy 52, 289–300.

Kalogirou, S.A., 1999. Applications of artificial neural networks in energy systems: a review. Energy Conversion and Management 40, 1073–1087.

Kalogirou, S.A., 2000. Applications of artificial neural-networks for energy systems. Applied Energy 67, 17–35.

Kalogirou, S.A., Panteliou, S., 2000. Thermosiphon solar domestic water heating systems: long-term performance prediction using artificial neural networks. Solar Energy 69, 163–174.

Kalogirou, S.A., Tripanagnostopoulos, Y., 2006. Hybrid PV/T solar systems for domestic hot water and electricity production. Energy Conversion and Management 47, 3368–3382.

Kalogirou, S.A., Panteliou, S., Dentsoras, A., 1999. Modeling of solar domestic water heating systems using artificial neural networks. Solar Energy 65, 335–342.

Karatepe, E., Boztepe, M., Colak, M., 2006. Neural network based solar cell model. Energy Conversion and Management 47, 1159–1178.

Krauter, S., 2006. Solar Electric Power Generation: Photovoltaic Energy Systems. Springer-Verlag, Heidelberg.

Lewis, N.S., Nocera, D.G., 2006. Powering the planet: chemical changes in solar energy utilization. Proceedings of the National Academy of Sciences of the United States of America 103, 15729–15735.

Mellit, A., Kalogirou, S.A., 2008. Artificial intelligence techniques for photovoltaics: a review. Progress in Energy and Combustion Science 34, 574–632.

Naewngerndee, R., Hattha, E., Chumpolrat, K., Sangkapes, T., Phongsitong, J., Jaikla, S., 2011. Finite element method for computational fluid dynamics to design photovoltaic thermal (PV/T) system configuration. Solar Energy Materials and Solar Cells 95, 390–393.

Radziemska, E., Klugmann, E., 2002. Thermally affected parameters of the current-voltage characteristics of silicon photocell. Energy Conversion and Management 43, 1889–1900.

Skoplaki, E., Palyvos, J.A., 2009. On the temperature dependence of photovoltaic module electrical performance. A review of efficiency/power correlations. Solar Energy 83, 614–624.

Sözen, A., Menlik, T., Ünvar, S., 2008. Determination of efficiency of flat-plate solar collectors using neural network approach. Expert Systems with Applications 35, 1533–1539.

Wang, S.A., Wu, L.G., 1990. Analysis and performance of flat-plate solar collector arrays. Solar Energy 45, 71–78.

Chapter 9: Summary and Conclusions

9.1 Introduction

It is generally assumed during the analysis of a traditional solar thermal collector that the heat exchange fluid is uniformly distributed. This simplification to the model consequently assumes a homogeneous temperature distribution over the absorber surface. Several studies discussed in Chapter 2, however, have demonstrated that this assumption is not entirely accurate and that the quality of flow distribution is dependent on several factors. The consequence of non-uniform flow through a solar thermal collector is that the warmer regions of the absorber (i.e. areas under reduced flow) are subject to greater heat losses to the ambient and therefore operate under reduced thermal efficiency. For a flat plate solar thermal collector used in domestic hot water application, the net impact of non-uniform flow is not severe. Therefore for the analysis of these collectors this assumption and the significant simplification it brings to the modelling process is commonly applied.

The hybrid PVT collector on the other hand, which incorporates photovoltaic cells has been shown to be temperature sensitive. Given the manner in which photovoltaic cells must be electrically connected so that their electrical output can be combined, the effect of non-uniform temperature has been demonstrated to have a much greater impact on the output of the collector. As the development of the PVT collector is still in its infancy relative to traditional solar thermal technology, this issue has not been sufficiently examined.

In order to investigate this issue further, a numerical model was developed to calculate the electrical output of the photovoltaic array which considered the variation in fluid flow

through a header/riser type fluid network and the resultant temperature of absorber. Using this model, a number of factors were investigated which considered the unique aspects of the building integrated PVT collector, such as the shape of the array and the direction of flow in the manifolds. This analysis provided several key findings. By examining the effect of a number of parameters such as the array geometry, mass flow rate, the ratio of the manifold to fluid channel diameters, and the direction of flow relative to the manifolds on the output of a PVT collector, it was possible to rank their statistical significance and identify two secondary interactions.

First, array geometry and two secondary interactions were shown to have statistically significant effects on the flow distribution and thermal performance of a building integrated collector. By using the finite difference method it was also shown that the fin efficiency was reduced by 5 per cent due to additional losses through the structural ribs of the collector in comparison to the value obtained using the classical fin approach. The second key finding was the development of a new method to determine the modelling parameters of a solar cell based on data provided by the manufacturer. Finally by integrating the fluid, heat transfer, and photovoltaic system analyses, a model was developed to quantify the photovoltaic yield of a BIPVT array of various designs which considered the detrimental impact of flow distribution. Each finding will be discussed in the proceeding sections.

9.2 Analysis of factors affecting flow distribution

Results from Chapter 3 indicated that the geometry of a solar collector will have the greatest impact on flow distribution based on a statistical analysis which examined a total of four factors (array shape, manifold to fluid channel pipe ratio, flow direction in manifolds and mass flow rate). Furthermore as a result of a two level full factorial

analysis, two secondary interactions were additionally identified which influence flow distribution and thermal output of a building integrated thermal collector. The interactions between array geometry and the direction of flow in the manifolds, and the array geometry and the ratio of manifold to fluid channel ratio were shown to impact thermal output. Although the numerical approach used by Jones and Lior [82] identified that the number and length of the risers will have an influence on flow distribution, the issue of geometry was not emphasised due to the minor variation in conventional solar thermal collector geometry. Furthermore previous studies did not identify any secondary interactions among factors investigated.

As the building integrated solar collector will be a made-to-measure product its geometry will be highly variable so that the individual customer's needs are met. Research conducted in this study has shown that geometry and its interaction with two other parameters will influence the quality of flow throughout the fluid network consequently the issue of flow distribution is of greater concern in comparison to conventional solar thermal technology.

9.3 Calculation of solar cell modelling parameters

Presently, several methods are available to determine the modelling parameters of a solar cell required for photovoltaic system modelling. A unique method has been developed in this research based on the multi-dimensional Newton-Raphson method which was experimentally shown to reduce modelling error over existing methods.

Originally a method was developed to determine the values of series (R_s) and shunt resistance (R_{sh}) based on data provided by the manufacturer at maximum power point. Initially this method was compared against values published by Charles et al. and compared against two alternative methods. It was shown that the method proposed in Chapter 4 matched the previously published values with the greatest accuracy. In order to

further validate this method, a precise source measuring unit was used to experimentally acquire the current-voltage data of a single multi-crystalline cell exposed to varying levels of natural sunlight in Chapter 5. Simulated current-voltage data was then generated using resistance values calculated using three methods and the method proposed in Chapter 4. This analysis demonstrated that at maximum power point (MPP), greatest accuracy was obtained using the proposed method. Using a root mean square error analysis, it was shown that the method offers greatest accuracy over the entire voltage vector (i.e.$0 < V < V_{oc}$).

Closely examining the combined experimental and simulated current-voltage data, a growing disparity was identified moving away from MPP. Investigating this issue further, it was found that by adjusting the diode constant value this disparity could be reduced thereby improving modelling accuracy. A modification to the original algorithm used to calculate R_s and R_{sh} was made in Chapter 6 so that it could also calculate the diode constant value, n. This method was experimentally shown to further reduce modelling error over existing techniques. At 1000 W/m^2 of illumination for example, root mean square error was reduced from 0.0101 to 0.0038.

The method to determine modelling parameters in this thesis has the advantages that it offers improved modelling accuracy when compared against two other recently published methods. By employing numerical methods which limit the number of assumptions and simplifications in the analysis, improved accuracy is obtained over the analytical approach. Furthermore, it also only requires data provided by the manufacturer at standard test conditions.

9.4 The effect of flow distribution on the photovoltaic output

By combining the fluid and heat transfer analysis conducted in Chapter 3 with the photovoltaic system modelling method outlined in Chapters 4 to 6, a complete model was developed to calculate photovoltaic output for a BIPVT collector operating under heterogeneous temperature as a result of flow mal-distribution. Using this model, a number of scenarios were investigated examining the effect of flow distribution on the photovoltaic output of a BIPVT array. Changes were made to the manifold to fluid channel pipe ratio, array geometry, flow direction in manifolds, and the mass flow rate. For the case where flow uniformity was poorest, it was found that only a 2 % improvement in PV output is made over a traditional photovoltaic panel with no cooling. However a 10 % improvement was obtained where flow uniformity was optimal. Therefore by appropriately addressing the issue of flow distribution, the photovoltaic yield can be improved.

Current methods typically adopt the approach used by conventional solar thermal technology which makes the assumption that flow throughout the collector is uniform. Such an assumption could lead to misleading results and an over estimation of the photovoltaic output of a system. Current literature in this field of BIPVT collector technology has not adequately addressed this issue. The model presented in this thesis may be used to approximate the photovoltaic yield of a BIPVT array with greater accuracy by considering the effects of flow mal-distribution. Results presented in Chapter 7 revealed that if the issue of flow distribution is not appropriately addressed, photovoltaic yield may be reduced by up to 10%. If flow distribution is assumed uniform as typically carried out at present, this disparity between model and actual outputs would lead to reduced power generation and inaccurate economic forecasts. Implementing the steps carried out in this study can reduce this error.

9.5 Conclusions

Harnessing energy from the sun is an active area of research and development driven primarily by the science of climate change science and the desire for energy independence. The successful implementation of solar technologies, such as the building integrated PVT collector however must address a number of technical and economic issues. This particular collector offers a number of advantages over conventional solar technologies such as;

1. Improved electrical output as a result of cooling.
2. Greater energy yield per unit area of roofing.
3. Improved architectural uniformity.

Despite these advantages, the market penetration of this collector type is minimal to date. Economic justification is mandatory for any capital expenditure, therefore a detailed model is necessary to forecast the approximate energy yield from an array of specified size. The PVT collector is unique in comparison to traditional solar thermal and photovoltaic collectors in the sense that the thermal and photovoltaic outputs are linked. This link however has not been explored in sufficient detail which runs the risk of possible overestimation in energy yield.

In this study a model has been developed which couples fluid flow, heat transfer, and photovoltaic conversion in order to quantify the photovoltaic output of a BIPVT collector which considers the effects of flow distribution. During the development of this model, it was shown that:

• Four factors have a statistical impact on flow distribution; Array shape, the manifold to fluid channel pipe ratio, the direction of flow in the manifold and the mass flow rate. Array geometry was to have the greatest statistical effect on flow distribution and thermal output of a building integrated solar collector.

• Two secondary interactions were identified to influence the quality of flow distribution; (i) array geometry and the ratio of the manifold to fluid channel, and (ii) array geometry and the flow direction in the manifolds.

• By conducting a numerical analysis of the building integrated collector using the finite difference method, fin efficiency was shown to be 5% less than a traditional rectangular fin and tube absorber design.

• Photovoltaic cell modelling parameters R_s, R_{sh}, and n can be modelled using the multi-dimensional version of the Newton-Raphson method and current-voltage equations expressed using Lambert W-function in comparison to other current methods. It was demonstrated both theoretically and experimentally that the proposed method offers an improvement to modelling accuracy and can be implemented using data provided by the manufacturer.

The model was then used to demonstrate the reduction in photovoltaic yield as a result of the flow distribution phenomenon. As the geometry of the building integrated collector will vary considerably, the assumption of uniform flow throughout the fluid network as currently employed may lead to a significant overestimation of the photovoltaic output. The model presented here can be used to address this issue to assist in the successful implementation of this promising technology.

9.6 Scope of research and future work

The analysis conducted here was limited to the header riser fluid type network only. Other fluid networks were beyond the scope of this work. Additionally this study was concerned only with the working fluid water and the operational characteristics of crystalline silicon solar cells which the authors believe to be the most commonly applied, however other working fluids and PV technologies may also be implemented.

For future work, it is recommended that other fluid networks also be investigated as a large number of absorber types many of which were presented in Chapter 2, have been proposed. Furthermore, the use of air as the heat exchanger working fluid was not investigated in this work. As air is a commonly used medium for this collector type, it is recommended that a fluid analysis be similarly conducted.

References

1. Lewis, N.S. and D.G. Nocera, *Powering the planet: Chemical changes in solar energy utlization.* Proceedings of the National Academy of Sciences of the United States of America, 2006. **103**(43): p. 15729-15735.
2. Ibrahim, A., et al., *Recent advances in flat plate photovoltaic/thermal (PV/T) solar collectors.* Renewable and Sustainable Energy Reviews, 2011. **15**: p. 352-365.
3. Jones, A.D. and C.P. Underwood, *A thermal model for photovoltaic systems.* Solar Energy, 2001. **70**(4): p. 349-359.
4. Zondag, H.A., *Flat-plate PV-Thermal collectors and systems: A review.* Renewable and Sustainable Energy Reviews, 2008. **12**: p. 891-959.
5. Athienitis, A., et al., *Experimental and numerical results for a building-integrated photovoltaic test facility*, in *31st IEEE Photovoltaic Specialists Conference*2005: Lake Buena Vista, Florida. p. 1718-1721.
6. Yusof Othman, M., et al., *Performance studies on a double finned double-pass photovoltaic-thermal (PV/T) solar collector.* Desalination 2007. **109**: p. 43-49.
7. Duffie, J.A. and W.A. Beckman, *Solar engineering of thermal processes*. 3rd ed. 2006, New Jersey: John Wiley & Sons.
8. Goetzberger, A. and C. Hebling, *Photovoltaic materials, past, present, future.* Solar Energy Materials & Solar Cells, 2000. **62**: p. 1-19.
9. Anderson, T.N., *Investigation of thermal aspects of building integrated photovoltaic/thermal solar collectors*, in *Science & Engineering*2009, Waikato University: Hamilton.
10. Anderson, T.N., M. Duke, and J.K. Carson, *The effect of colour on the thermal performance of building integrated solar collectors.* Solar Energy Materials & Solar Cells, 2010. **94**: p. 350-354.
11. Lange, R.F.M., et al., *The lamination of (multi)crystalline and thin film based photovoltaic modules.* Progress in Photovoltaics: Research and Applications, 2010.
12. McGuiness, B., *Design of building integrated photovoltaic product for long run metal roofing*, in *Engineering*2012, University of Waikato: Hamilton.
13. Wolf, M., *Performance analysis of combined heating and photovoltaic power system for residences.* Energy Convers, 1976. **16**: p. 79-90.
14. Kalogirou, S.A. and Y. Tripanagnostopoulos, *Hybrid PV/T solar systems for domestic hot water and electricity production.* Energy Conversion and Management, 2006. **47**: p. 3368-3382.
15. Chow, T.T., *A review on photovoltaic/thermal hybrid solar technology.* Applied Energy, 2010. **87**: p. 365-79.
16. Santbergen, R. and A.A. van Zolingen, *Modeling the thermal absorption factor of photovoltaic/thermal combi-panels.* Energy Conversion and Management, 2006. **47**: p. 3572-3581.
17. Green, M.A., *Solar Cells Operating Principles, Technology and System Applications*. 1998: University of New South Wales.
18. Lee, Y. and A.O. Tay, *Finite element thermal analysis of a solar photovoltaic module.* Energy Procedia, 2012. **15**: p. 413-420.
19. *PVT Roadmap – a European guide for the development and market introduction of PV-thermal technology*, in *PVT forum*2006.
20. Bergene, T. and O.M. Lovvik, *Model calculations on a flat plate solar heat collector with integrated solar cells.* Solar Energy, 1995. **55**(6): p. 453-462.
21. Zondag, H.A., et al., *The thermal and electrical yield of a PV-thermal collector.* Solar Energy, 2002. **72**(2): p. 113-128.
22. Zondag, H.A., et al., *The yield of different combined PV-thermal collector designs.* Sol Energy, 2003. **74**(3): p. 253-269.

23. Kumar, R. and M.A. Rosen, *A critical review of photovoltaic-thermal solar collectors for air heating.* Applied Energy, 2011. **88**: p. 3603-3614.
24. da Silva, R.M. and J.L.M. Fernandes, *Hybrid photovoltaic/thermal (PV/T) solar systems simulation with Simulink/Matlab.* Solar Energy, 2010. **84**: p. 1985-1996.
25. Charalambous, P.G., et al., *Photovoltaic thermal (PV/T) collectors: A review.* Applied Thermal Engineering 2006. **27**: p. 275-86.
26. Ji, J., et al., *Experimental study of photovoltaic solar assisted heat pump system.* Solar Energy, 2008. **82**: p. 43-52.
27. Ji, J., et al., *Distributed dynamic modeling and experimental study of PV evaporator in a PV/T solar-assisted heat pump.* International Journal of Heat and Mass Transfer, 2009. **52**: p. 1365-1373.
28. Kuang, Y.H., R.Z. Wang, and L.Q. Yu, *Experimental study on solar assited heat pump system for heat supply.* Energy Conversion and Management, 2003. **44**(1089-1098).
29. Ito, S., N. Miura, and Y. Takano, *Studies of heat pumps using direct expansion type solar collectors.* Journal of Solar Energy Engineering, 2005. **127**: p. 60-64.
30. Liu, K., et al., *Performance study of a photovoltaic solar assisted heat pump with variable-frequency compressor—a case study in Tibet.* Renewable Energy, 2009. **34**(2680-2687).
31. Bakker, M., et al., *Performance and costs of a roof-sized PV/thermal array combined with a ground coupled heat pump.* Solar Energy, 2005. **78**: p. 331-339.
32. Tyagi, V.V., S.C. Kaushik, and S.K. Tyagi, *Advancement in solar photovoltaic/thermal (PV/T) hybrid collector technology.* Renewable and Sustainable Energy Reviews, 2012. **16**: p. 1383-1398.
33. Bhargava, A.K., H.P. Garg, and V.K. Sharma, *Theory of multiple-pass solar air heaters.* Energy, 1985. **10**(5): p. 589-599.
34. Hegazy, A., *Comparative study of the performance of four photovoltaic/ thermal solar air collectors.* Energy Convers manage, 2000. **41**: p. 861-81.
35. Garg, H.P., G. Datta, and B. Bandyopadhyay, *A study on the effect of enhanced heat transfer area in solar air heaters.* Energy Conversion and Management, 1983. **23**(1): p. 43-49.
36. Cole Appel, B.E. and R.D. Haberstroh. *Performance of air-cooled flat-plate collectors*. in *On sharing the sun, solar technologies in the seventies*. 1976. Winnipeg.
37. Choudhury, C., S.L. Andersen, and J. Rekstad, *A solar air heater for low temperature applications* Solar Energy, 1988. **40**(4): p. 335-343.
38. Sopian, K., et al., *Performance analysis of photovoltaic thermal air heaters.* Energy Conversion and Management, 1996. **37**(11): p. 1657-1670.
39. Joshi, A.S., et al., *Performance evaluation of a hybrid photovoltaic thermal (PV/T) (glass-to-glass) system.* International Journal of Thermal Sciences, 2009. **48**: p. 154-164.
40. Tripanagnostopoulos, Y., et al., *Hybrid photovoltaic/thermal solar systems* Solar Energy, 2002. **72**: p. 217-34.
41. Hollick, J.C., *Solar cogeneration panels.* Renewable Energy, 1998. **15**: p. 195-200.
42. Nagano, K., et al., *Development of thermal-photovoltaic hybrid exterior wallboards incorporating PV cells in and their winter performances.* SEMS 2003. **77**: p. 265-82.
43. Kalogirou, S.A. and Y. Tripanagnostopoulos, *Industrial application of PV/T solar energy systems.* Applied Thermal Engineering, 2007. **27**: p. 1259-1270.
44. Daghigh, R., M.H. Ruslan, and K. Sopian, *Advances in liquid based photovoltaic/thermal (PV/T) collectors.* Renwable and Sustainable Energy Reviews, 2011. **15**: p. 4156-4170.

45. Roblescampo, B., et al., *Photovoltaic/thermal solar hybrid systems with bifacial PV module and transparent plane collector.* Solar Energy, 2007. **91**: p. 1966-71.
46. Rockendorf, G., et al., *PV-hybrid and thermoelectric collectors.* Solar Energy, 1999. **67**: p. 227-237.
47. Fraisse, G., C. Menezo, and K. Johannes, *Energy performance of water hybrid PV/T collectors applied to combisystems of direct solar floor type.* Solar Energy, 2007. **81**: p. 1426-1439.
48. Dupeyrat, P., et al., *Efficient single glazed flat plate photovoltaic-thermal hybrid collector for domestice hot water system.* Solar Energy, 2011. **85**: p. 1457-1468.
49. Chow, T.T., W. He, and J. Ji., *Hybrid photovoltaic-thermosyphon water heating system for residential application.* Solar Energy, 2006. **80**: p. 298-306.
50. Erdil, E., M. Ilkan, and F. Egelioglu, *An experiment study on energy generation with photovoltaic (PV)-solar thermal hybrid system.* Energy, 2008. **33**: p. 1241-1245.
51. Hendrie, S., *Photovoltaic/thermal Collector Development Program - Final Report*, in *Report MIT*1982, Lincoln laboratory.
52. Bakker, M., H.A. Zondag, and D. Prasad. *Demonstartion on a dual flow photovoltaic/thermal combi panel*. in *Proceedings of PV in Europe-From PV technology to Energy Solutions Conference and Exhibition*. 2002. Rome, Italy.
53. Santbergen, R., et al., *Detailed analysis of the energy yield of systems with covered sheet-and-tube PVT collectors.* Solar Energy, 2010. **84**: p. 867-878.
54. Jelle, B.P. and C. Breivik, *State-of-the-art building integrated photovoltaics.* Energy Procedia, 2012. **20**: p. 68-77.
55. Frankl, P., M. Gamberale, and R. Battisti. *Life cycle assessment of a PV cogenerative system: comparison with a solar thermal collector and a PV system*. in *16th European photovoltaic solar energy conference*. 2000. Glasgow.
56. Tselepis, S. and Y. Tripanagnostopoulos. *Economic analysis of hybrid photovoltaic/thermal solar systems and comparison with standard PV modules*. in *PV in Europe - from PV technology to energy solutions conference and exhibition*. 2002. Rome.
57. Corbin, C. and J.Z. Zhiqiang, *Experimental and numerical investigation on thermal and electrical performance of a building integrated photovoltaic-thermal collector system.* Energy and Buildings 2010. **42**: p. 76-82.
58. Clarke, J.A., et al., *Photovoltaic-integrated building facades.* Renewable Energy, 1996. **8**(1-4): p. 475-479.
59. Zondag, H.A., et al., *Thermal and electrical yield of combi-panel.* Proceedings of ISES Bi-annual Conference on CD-ROM, Jerusalem 1999.
60. Chel, A., G.N. Tiwari, and A. Chandra, *Simplified method of sizing and life cycle cost assessment of building integrated photovoltaic system.* Energy and Buildings, 2009. **41**: p. 1172-1180.
61. Benemann, J., E.S. Chehab, and E.S. Gabriel, *Building integrated PV modules.* Solar Energy Materials & Solar Cells, 2001. **67**: p. 345-354.
62. Davis, M.W., A.H. Fanney, and B.P. Dougherty, *Prediction of building integrated photovoltaic cell temperatures.* Journal of Solar Energy Engineering 2001. **123**(3): p. 200-210.
63. Green, M.A., *General Temperature Dependence of Solar Cell Performance and Implications for Device Modelling.* Progress in Photovoltaics: Research and Applications, 2003. **11**: p. 333-340.
64. Chow, T.T., J.W. Hand, and P.A. Strachan, *Building-integrated photovoltaic and thermal applications in a subtropical hotel building.* Applied Thermal Engineering, 2003. **23**: p. 2035-2049.
65. Chow, T.T., W. He, and J. Ji, *An experimental study of facade-integrated photovoltaic/water-heating system.* Applied Thermal Engineering, 2007. **27**: p. 37-45.

66. Chow, T.T., et al., *Computer modeling and experimental validation of a building integrated photovoltaic and water heating system.* Applied Thermal Engineering, 2008. **28**: p. 1356-1364.
67. Dubey, S. and G.N. Tiwari, *Thermal modeling of a combined system of photovoltaic thermal (PV/T) solar water heater.* Solar Energy, 2008. **82**: p. 602-612.
68. Touafek, K., M. Haddadi, and A. Malek, *Modeling and Experimental Validation of a New Hybrid Photovoltaic Thermal Collector.* IEEE Transactions on Energy Conversion, 2010. **PP**(99): p. 1-8.
69. Florschuetz, L., *Extension of the Hotell Whiller model to the analysis of combined photovoltaic/thermal flat plate collectors.* Sol Energy, 1979. **22**: p. 361-6.
70. Hottel, H.C. and B.B. Woertz, *The performance of flat-plate solar heat collectors.* Trans. ASME, 1942. **64**: p. 91-104.
71. Whillier, A., *Solar Energy Collection and its Utilisation for House Heating*, 1953, MIT: Cambridge, MA.
72. Hottel, H.A. and A. Whillier, *Evaluation of flat-plate solar collector performance*, in *Trans. of the conference on the Use of Solar Energy, The Scientific Basis*1958, University of Arizona Press: Tucson, Arizona. p. 74-104.
73. Evans, D.L., *Simplified method for predicting photovoltaic array output* Solar Energy 1981. **27**: p. 555-560.
74. Anderson, T.N., et al., *Performance of a building integrated photovoltaic/thermal (BIPVT) solar collector.* Solar Energy, 2009. **83**: p. 445-455.
75. Kreith, F. and J.F. Kreider, *Principles of Solar Engineering*. 1978, New York: McGraw-Hill.
76. Beckman, W.A., A. Klein, and J.A. Duffie, *Solar Heating Design by the F-chart Method*. 1977, New York: Wiley.
77. Datta, A.B. and A.K. Majumdar, *Flow distribution in parallel and reverse flow manifolds.* International Journal of Heat and Fluid Flow 1980. **2**(4).
78. Acrivos, A., B.D. Babcock, and R.L. Pigford, *Flow distributions in manifolds.* Chemical Engineering Science 1958. **10**: p. 112-124.
79. Dunkle, R.V. and E.T. Davey. *Flow distribution in solar absorber banks*. in *Proc. ISES Conference*. 1970. Melbourne, Australia.
80. Chiou, J.P., *The effect of nonuniform fluid flow distribution on the thermal performance of solar collector.* Solar Energy, 1982. **29**(6): p. 487-502.
81. Wang, S.A. and L.G. Wu, *Analysis and performance of flat-plate solar collector arrays.* Solar Energy, 1990. **45**(2): p. 71-78.
82. Jones, G.F. and N.L. Lior, *Flow distribution in manifold solar collectors with negligible buoyancy effects.* Solar Energy, 1994. **52**(3): p. 289-300.
83. Molero Villar, N., et al., *Numerical 3-D heat flux simulations on flat plate solar collectors.* Solar Energy, 2009. **83**: p. 1086-1092.
84. Naewngerndee, R., et al., *Finite element method for computational fluid dynamics to design photovoltaic thermal (PV/T) system configuration.* Solar Energy Materials & Solar Cells, 2011. **95**: p. 390-393.
85. Chegaar, M., Z. Ouennoughi, and F. Guechi, *Extracting dc parameters of solar cells under illumination.* Vacuum 2004. **75**: p. 367-372.
86. Chan, D.S. and J.C.H. Phang, *Analytical methods for the extraction of solar-cell single- and double-diode model parameters from I-V characteristics* IEEE Transactions on Electron devices, 1987. **34**(2): p. 286-293.
87. Carrero, C., J. Amadow, and S. Arnaltes, *A single procedure for helping PV designers to select silicon PV modules and evaluate the loss resistances.* Renewable Energy, 2007. **32**: p. 2579-2589.
88. Lo Brano, V., et al., *An improved five-parameter model for photovoltaic devices.* Solar Energy Materials & Solar Cells, 2010. **94**: p. 1358-1370.

89. Walker, G., *Evaluating MPPT converter technologies using a matlab PV model.* J. Elect. Electron. Eng., Australia 2001. **21**(1): p. 45-55.
90. Celik, A.N. and N. Acikgoz, *Modelling and experimental verification of the operating current of mono-crystalline photovoltaic modules using four-and five-parameter models.* Applied Energy, 2007. **84**: p. 1-15.
91. Villalva, M.G., J.R. Gazoli, and E.R. Filho, *Comprehensive Approach to Modeling and Simulation of Photovoltaic Arrays*. IEEE Transactions on Power Electronics 2009. **24**(5): p. 1198-1208.
92. Chenni, R., et al., *A detailed modeling method for photovoltaic cells.* Energy, 2007. **32**: p. 1724-1730.
93. De Soto, W., S.A. Klein, and W.A. Beckman, *Improvement and validation of a model for photovoltaic array performance.* Solar Energy, 2006. **80**(1): p. 78-88.
94. de Blas, M.A., J.L. Torres, and A. Garcia, *Selecting a suitable model for characterizing photovoltac devices.* Renewable Energy, 2002. **25**: p. 371-380.
95. Bouzidi, A., M. Chegaar, and A. Bouhemadou, *Solar cells parameters evaluation considering the series and shunt resistance.* Solar Energy & Materials, 2007. **91**: p. 1647-1651.
96. Carrero, C., et al., *Simple estimation of PV modules loss resistances for low error modelling.* Renewable Energy, 2010: p. 1103-1108.
97. Charles, J.P., et al., *A practical method of analysis of the current-voltage characteristics of solar cells.* Solar Cells, 1981. **4**: p. 169-178.
98. Jain, A. and A. Kapoor, *Exact analytical solutions of the parameters of real solar cells using Lambert W-function.* Solar Energy & Materials 2004. **81**: p. 269-277.
99. Banwell, T.C. and A. Jayakumar *Exact Analytical Solution for Current flow through Diode with Series resistance*. Electronics letters 2000. **36**, 291-292.
100. Lambert, J.H., *Observationes variae in mathesin puram.* Acta Helvetica, physico-mathematico-anatomico-botanico-medica, 1758. **3**: p. 128-168.
101. Corless, R.M., et al., *On the Lambert W function.* Adv. Computational Maths. , 1996. **5**: p. 329-359.
102. Petrone, G., G. Spagnuolo, and M. Vitelli, *Analytical model of mismatched photovoltaic fields by means of Lambert W-function.* Solar Energy Materials and Solar Cells, 2007. **91**: p. 1652-1657.
103. Picault, D., et al., *Forecasting photovoltaic array power production subject to mismatch losses.* Solar Energy, 2010. **84**: p. 1301-1309.
104. Phang, J.C.H., D.S. Chan, and J.R. Phillips, *Accurate analytical method for the extraction of solar cell model parameters.* Electron letters, 1984. **20**(10): p. 406-408.
105. Wenham, S.R., et al., *Applied photovoltaics*. 2nd ed. 2008, London: Taylor & Francis Ltd.
106. van Dyk, E.E. and E.L. Meyer, *Analysis of the effect of parasitic resistances on the performance of photovoltaic modules.* Renewable Energy, 2004. **29**: p. 333-344.
107. Green, M.A., *Accuracy of analytical expressions for solar cell fill factors.* Solar Cells, 1982. **7**(3): p. 337-340.
108. Bashahu, M. and A. Habyarimana, *Review and test of methods for determination of the solar cell series resistance.* Renewable Energy, 1995. **6**(2): p. 129-138.
109. Emery, K., et al., *Temperature dependence of photovoltaic cells, modules and systems*, in *Proceedings of the 25th IEEE Photovoltaic Specialists Conference*1996: Washington DC, USA. p. 1275-1278.
110. Arora, N.D. and J.R. Hauser, *Temperature dependence of silicon solar cell characteristics.* Solar Energy Materials 1982. **6**: p. 151-158.
111. Meneses-Rodriguez, D., et al., *Photovoltaic solar cells performance at elevated temperatures.* Solar Energy, 2005. **78**: p. 243-250.

112. Nordmann, T. and L. Clavadetscher. *Understanding temperature effects on PV system performance*. in *Proceedings of the 3rd world conference on photovoltaic energy conversion*. 2003. Osaka, Japan.
113. Singh, P., et al., *Temperature dependence of I-V characteristics and performance parameters of silicon solar cell.* Solar Energy Materials and Solar Cells, 2008. **92**: p. 1611-1616.
114. Wysocki, J. and P. Rappaport, *Effect of Temperature on Photovoltaic Solar Energy Conversion.* Journal of Applied Physics, 1959. **31**(3): p. 571-578.
115. Radziemska, E. and E. Klugmann. *Effect of temperature on conversion efficiency of solar module* in *Proceedings of the XXIII IMAPS Conference*. 1999. Kolobrzeg, Poland.
116. Radziemska, E. and E. Klugmann, *Thermally affected parameters of the current-voltage characteristics of silicon photocell.* Energy Conversion and Management 2002. **43**: p. 1889-1900.
117. Wolf, H.F., *Semiconductors*. 1971, New York: Wiley.
118. Skoplaki, E. and J.A. Palyvos, *On the temperature dependence of photovoltaic module electrical performance: A review of efficiency/power correlations.* Solar Energy, 2009. **83**: p. 614-624.
119. Skoplaki, E. and J.A. Palyvos, *Operating temperature of photovoltaic modules: A survey of pertinent correlations.* Renewable Energy, 2009. **34**: p. 23-29.
120. Zakharchenko, R., et al., *Photovoltaic solar panel for a hybrid PV/thermal system.* Solar Energy Materials and Solar Cells, 2004. **82**: p. 253-261.
121. Chow, T.T., *Performance analysis of photovoltaic-thermal collector by explicit dynamic model.* Sol Energy, 2003. **75**(2): p. 143-152.
122. Bucciarelli, L.L., *Power loss in photovoltaic arrays due to mismatch in cell characteristics.* Solar Energy, 1979. **23**: p. 277-288.
123. Shechter, M., J. Appelbaum, and G. Yekutieli, *Quality factors of solar cell arrays.* Solar Cells, 1983. **9**: p. 295-309.
124. Saha, H. and G. Bhattacharya, *Mismatch losses in series combinations of silicon solar cell modules.* Solar Cells, 1988. **25**: p. 143-153.
125. Lambarski, T.J., *Design Analysis of Advanced PV Technologies, SERI Technical Report*, 1982, BDM Corporation.
126. Bishop, J.W., *Computer simulation of the effects of electrical mismatches in photovoltaic cell interconnection circuits.* Solar Cells, 1988. **25**: p. 73-89.
127. Crozier, J.L., E.E. van Dyk, and F.J. Vorster, *Characterization of cell mismatch in a multi-crystalline silicon photovoltaic module.* Physica B, 2012. **407**: p. 1578-1581.
128. Kaushika, N.D. and A.K. Rai, *An investigation of mismatch losses in solar photovoltaic cell networks.* Energy 2007. **32**: p. 755-759.
129. Abete, A., et al., *A study of shading effects in photovoltaic generators*, in *9th EC Photovoltaic Solar Energy Conference*1989. p. 240-244.
130. Alonson-Garcia, M.C., J.M. Ruiz, and W. Herrmann, *Computer simulation of shading effects in photovoltaic arrays.* Renewable Energy, 2006. **31**: p. 1986-1993.
131. Caluianu, I., et al., *Photovoltaic Energy Generation under Partially Shading Conditions*, in *ELECTROMOTION 2009 - EPE Chapter 'Electric Drives' Joint Sympsium*2009: Lille, France.
132. Gupta, A. and A.G. Milnes. *Effects of shading and defects in solar cell arrays*. in *15th IEEE Photovolatic Specialists Conference*. 1981.
133. Rauschenbach, H.S., *Electrical output of shaded solar arrays*, in *IEEE Trans. Electron Devices*1971. p. 483-490.
134. Nguyen, D.D. and B. Lehman, *An adaptive solar photovoltaic array using model-based reconfiguration algorithm.* IEEE Transactions on Industrial Electronics, 2008. **55**: p. 2644-2654.

135. Green, M.A., E. Gauja, and W. Withayachamnankul, *Silicon solar cells with integral bypass diodes.* Solar Cells 1981. **3**: p. 233-244.
136. Abete, A., et al. *Analysis of photovoltaic modules with protection diodes in presence of mismatching*. in *21st IEEE Photovolatic Specialists Conference*. 1990.
137. Swaleh, M.S. and M.A. Green, *Effect of shunt resistance and bypass diodes on the shadow tolerance of solar cell modules.* Solar Cells, 1982. **5**: p. 199-204.
138. Roche, D., H. Outhred, and J.R. Kaye. *Optimised design of photovoltaic arrays* in *AU PEC: Australasian Universities Power Engineering Conference*. 1993.
139. Green, M.A., *Silicon cells with integral bypass diodes*, in *NERDC Report*1982, National Energy Research and Development Council: Canberra, Australia.
140. Wenham, S.R., et al. *Screen printed processing of solar cells incoporating integral bypass diodes*. in *16th IEEE Photovoltaic Specialists Conference*. 1982.
141. Hasyim, E.S., S.R. Wenham, and M.A. Green, *Shadow tolerance of modules incoporating integral bypass diode solar cells.* Solar Cells, 1986. **19**: p. 109-122.
142. Roche, D., H. Outhred, and J.R. Kaye, *Analysis and Control of Mismatch Loss in Photovoltaic Arrays* Progress in Photovoltaics: Research and Applications 1995. **3**: p. 113-127.
143. Gonzalez, C.C. and R. Weaver. *Circuit design considerations for photovoltaic modules and systems*. in *14th IEEE Photovoltaic Specialists Conference*. 1980. San Diego.
144. Wenger, H.J., et al. *Decline of the Carrisa plains photovoltaic power plant: the impact of concentrating sunlight on flat plates* in *Proc. 22nd IEEE Photovoltaic Specialists Conference*. 1991.
145. Goss, R.G. *Technology developments toward 30 year life of photovoltaic modules and systems*. in *17th IEEE Photovoltaic Specialists Conference*. 1984. Orlando.
146. Bhattacharya, G. and C. Neogy, *Removal of the hot-spot problem in photovoltaic modules and arrays* Solar Cells, 1991. **31**: p. 1-12.
147. Fahrenbruch, A.L. and R.H. Bube, *Fundamentals of Solar Cells*. 1983, New York: Academic Press. 272.
148. Wang, Y.J. and P.C. Hsu, *An investigation on partial shading of PV modules with different connection configurations of PV cells.* Energy, 2011. **36**: p. 3069-3078.
149. Asif, M. and T. Muneer, *Energy supply, its demand and security issues for developed and emerging economies.* Renewable and Sustainable Energy Reviews, 2007. **11**: p. 1388-1413.
150. Weiss, W. and F. Mauthner, *Solar heat worldwide markets and contributions to the energy supply 2010*, in *Solar Heating & Cooling Programme*2012, International Energy Agency.
151. Zhai, X.Q., et al., *Solar integrated energy system for a green building.* Energy and Buildings, 2007. **39**: p. 985-993.
152. Medved, S., C. Arkar, and B. Cerne, *A large-panel unglazed roof-integrated liquid solar collector-energy and economic evaluation.* Solar Energy, 2003. **75**: p. 455-467.
153. Ghani, F., M. Duke, and J.K. Carson, *Effect of flow distribution on the photovoltaic performance of a building integrated photovolatic/thermal (BIPV/T) collector.* Solar Energy, 2012. **86**(11): p. 1518-1530.
154. Mathews, P., *Design of experiments with Minitab*. 2005, US: ASQ Quality Press.
155. Antony, J., *Design of experiments for engineers and scientists*. 2008, Oxford: Butterworth-Heinemann.
156. Incropera, F.P., et al., *Fundamentals of Heat and Mass Transfer*. 2006, New York: John Wiley & Sons.
157. Nellis, G. and S.A. Klein, *Heat Transfer*. 2009, New York: Cambridge University Press.

158. Myers, G.E., *Analytical methods in conduction heat transfer*. 1987, US: Genium Publishing Corp.
159. Kays, W.M. and M.E. Crawford, *Convective Heat and Mass Transfer*. 3rd ed. ed. 1993, New York: McGraw-Hill.